

EXPOSURE-AWARE SIGNAL DESIGN FOR
MILLIMETER WAVE MIMO COMMUNICATION SYSTEMS

A Dissertation

Submitted to the Faculty

of

Purdue University

by

Miguel Rodrigo Castellanos Llorca

In Partial Fulfillment of the

Requirements for the Degree

of

Doctor of Philosophy

May 2020

Purdue University

West Lafayette, Indiana

THE PURDUE UNIVERSITY GRADUATE SCHOOL
STATEMENT OF DISSERTATION APPROVAL

Dr. David J. Love, Co-Chair

School of Electrical and Computer Engineering

Dr. Borja Peleato, Co-Chair

School of Electrical and Computer Engineering

Dr. Mark R. Bell

School of Electrical and Computer Engineering

Dr. James V. Krogmeier

School of Electrical and Computer Engineering

Approved by:

Dr. Dimitrios Peroulis

Head of the School of Electrical and Computer Engineering

To my abuela

ACKNOWLEDGMENTS

I am extremely fortunate to have received support and guidance from numerous people during my time at Purdue. While it was difficult to compress their contributions down to a few paragraphs, it was a pleasure to reminisce on their part in this journey.

I am deeply indebted to my advisors, Professor David J. Love and Professor Borja Peleato. I would like to thank David for his invaluable insights and for his gentle nudges when I was stuck in my research. I first met David as an undergraduate student; his academic passion was a key factor in my decision to pursue a Ph.D. David taught me many things, and his unrelenting drive for excellence has served as a constant source of inspiration.

I would also like to thank Borja for his unparalleled attentiveness and encouragement. Our frequent meetings were instrumental in my doctoral development. He often acted as a sounding board for my ideas, and his discerning judgement helped me sort out the good ones from the not so good ones. Both David and Borja were incredible mentors and friends, and I am proud to have been able to work with them.

I wish to thank Professor James V. Krogmeier and Professor Mark R. Bell for serving on my advisory committee. Their thoughtful questions and suggestions on my work were greatly appreciated. I also developed a strong foundation in the field of wireless communication under their exceptional instruction.

I had the great pleasure of collaborating with faculty at other institutions on the SAR project. In particular, I would like to thank Professor Bertrand Hochwald at the University of Notre Dame and Professor Jian-Ming Jin at the University of Illinois at Urbana-Champaign. Their constructive feedback and vast expertise were integral in finding and fixing the gaps in my research.

I am grateful to have completed two internships during my graduate studies, both of which aided me in attaining technical skills and practical knowledge. I appreciate the help provided by Tiangyang Bai, Jung Ryu, and Sundar Subramanian at the Qualcomm Corporate R&D Office in Bridgewater, NJ; and Eugene Visotsky, Fred Vook, and Amitava Ghosh at Nokia Bell Labs in Naperville, IL. I would like to give special thanks to Vasanthan Raghavan, whose advice extended far beyond my time at Qualcomm. His acute, no-nonsense perspectives greatly influenced how I gauge the quality of research, including my own.

I would like to recognize my colleagues, past and present, in the TASC lab. Whenever I had any minor issues, it was a great comfort to know that the solution was typically a short walk away. My interactions with them were overwhelmingly positive, and I hope that I was able to repay the kindness they shared with me. I would specifically like to thank Dennis Ogbe, who saved me a considerable amount of time in writing papers and code by introducing me to Emacs, and Dawei Ying, who was a great mentor during my early studies.

This research would not have been possible without the generous financial support of the National Science Foundation, which partially funded my work under grants CCF-1403458 and CNS-1642982.

While their contributions are less obvious, my friends and family have played the largest role in shaping who I am. I would like to thank my friends, Giuseppe Giuliani, Conor Sullivan, and Paul Krogmeier, all of whom I have known since I was young. Our strange escapades led to many nights of tear-inducing laughter and gave me respite during times of hardship. I am very grateful for my brothers, whose tireless energy always managed to cheer me up. My mother, grandmother, aunt, and sister have had a profound impact on my life. They have always motivated me to do my best, and I largely dedicate my achievements to their unconditional support. Finally, I would especially like to thank my girlfriend, Jenny, for her seemingly infinite love and patience.

TABLE OF CONTENTS

	Page
LIST OF TABLES	ix
LIST OF FIGURES	x
ABBREVIATIONS	xiii
ABSTRACT	xv
1 Introduction	1
1.1 Signal-Level Models of Electromagnetic Exposure for Millimeter Wave Communication Systems	4
1.2 Efficient Signal Design Under Exposure Constraints	5
1.3 Beamforming Perturbation Approach for Mitigating User Exposure	7
1.4 Organization	8
1.5 Notation	9
2 Signal-Level Models of Electromagnetic Exposure for Millimeter Wave Com- munication Systems	10
2.1 Procedures for Computing Signal-Level Exposure Models	10
2.1.1 Review of Prior Art	10
2.1.2 Proposed Methods for Computing Exposure Matrices	13
2.2 Millimeter Wave Exposure Modeling	16
2.2.1 Incident Power Density	16
2.2.2 Specific Absorption Rate	20
2.3 Model Verification Results	24
2.3.1 Dipole Array Parameters and Head Model	24
2.3.2 Incident PD Model Validation	28
2.3.3 Surface SAR Model Validation	28
2.4 Exposure Model Analysis and Applications	29

	Page
2.4.1 Sampling Methods	30
2.4.2 Spatially Averaged Exposure Model	34
2.4.3 Numerical Examples of Sampling Methods	37
2.4.4 Average Exposure Model Validation	38
2.5 Conclusion	39
3 Efficient Signal Design Under Exposure Constraints	46
3.1 System Model	46
3.2 Discretization Method for Optimal Signaling	48
3.2.1 Problem Formulation	48
3.2.2 Discretization	49
3.2.3 Numerical Results	52
3.3 Position-Based Adaptive Power Back-Off	56
3.3.1 Problem Formulation	56
3.3.2 Dynamic Exposure Model	56
3.3.3 Power Back-Off Schemes	59
3.3.4 DFT Codebook Implementation	60
3.3.5 Numerical Results	61
3.4 Conclusion	64
4 Beamforming Perturbation Approach for Mitigating User Exposure	66
4.1 System Model	66
4.2 Perturbation-Based Beamforming	70
4.2.1 Minimum Distance	70
4.2.2 Maximum Correlation	73
4.2.3 Performance Analysis	75
4.3 Numerical Results	77
4.4 Conclusion	83
5 Summary	85
REFERENCES	87

	Page
A Appendix	92
A.1 Proof of Lemma 2.4.1	92
VITA	96

LIST OF TABLES

Table	Page
2.1 List of model parameters.	14
2.2 Dipole antenna parameter specifications.	25
2.3 Number of sample points for different choices of N and d	37

LIST OF FIGURES

Figure	Page
2.1 A diagram of the considered exposure scenario. A body model lies close to an N element transmitter array. The position of the n -th element is \mathbf{s}_n , and exposure is measured at a point \mathbf{p} on the body surface.	12
2.2 Diagram of the considered electromagnetic radiation transmission scenario with array elements located near a planar tissue model. The radiated field from the n -th source impinges on the tissue surface at an angle of incidence ζ_n^i and contributes to the total transmitted field.	22
2.3 HFSS setup for SAR simulations. The dipole array is placed 5 mm away from a hemispherical tissue model with radius 20 mm, complex dielectric constant $\epsilon^* = 19 - j19.26$, and tissue density 1 g/cm ³ . SAR values are obtained at a depth of 0.2 mm from the surface point \mathbf{p}	26
2.4 Plane wave equivalent PD values from HFSS simulations and the quadratic model $\mathbf{x}^H \mathbf{R}_{\text{PD}}(\mathbf{p}) \mathbf{x}$, with PD matrices calculated as in (2.7), vs. the beam sweep angle ψ of the transmit signal \mathbf{x} in (2.29). The point \mathbf{p} is located 5 mm from the array center and at 30° from boresight. Results with half-wave dipole ULAs are shown in the ideal case with (a) $N = 2$ and (b) $N = 4$, and in the non-ideal case with $N = 2$ and $N = 4$ in (c) and (d), respectively. The dipole antenna parameters are given in Table 2.2, and the array coupling matrices are given in (2.28).	27
2.5 SAR values from HFSS simulations, the SPW SAR model in (2.22), and the quadratic model $\mathbf{x}^H \mathbf{R}_{\text{SAR}}(\mathbf{p}) \mathbf{x}$, with SAR matrices calculated as in (2.10), vs. the beam sweep angle ψ of the transmit signal \mathbf{x} in (2.29). The body model and measurement point are shown in Fig. 2.3. Non-simulated values were scaled by a factor of 0.7024 to account for absorption losses. Results with half-wave dipole ULAs are shown in the ideal case with (a) $N = 2$ and (b) $N = 4$, and in the non-ideal case with $N = 2$ and $N = 4$ in (c) and (d), respectively. The dipole antenna parameters are given in Table 2.2, and the array coupling matrices are given in (2.28). In the non-ideal cases, the proposed model was scaled by a factor of $K = 1.203$ and $K = 1.423$ in (c) and (d), respectively.	41

Figure	Page
2.6	Plots of the sampling points obtained from the (a) uniform and (b) non-uniform sampling approaches over the surface of a spherical head model with radius 90 mm at a distance of 10 mm from a two-element ideal dipole ULA. Sampling was performed with an error parameter of $\epsilon = 25 \text{ mW/cm}^2$. 42
2.7	Two regions considered in the validation of the average exposure model. Each region is an arc of measure 5° on the surface of a spherical head model with radius 90 mm at a distance of 5 mm from the center of the array.43
2.8	Average PD values obtained from HFSS simulations using (2.48), and the proposed average exposure model in (2.55), vs. the beam sweep angle ψ of the transmit signal \mathbf{x} in (2.29) on the regions \mathcal{P}_1 and \mathcal{P}_2 . Values were obtained for a non-ideal two-element dipole array. For both regions, the proposed model was calculated using a uniform sampling with $\epsilon = 10 \text{ mW/cm}^2$ 44
2.9	Mean-square-error (MSE) between the average PD matrices $\mathbf{R}_{\text{PD, avg}}(\mathcal{P})$ from (2.60) and $\mathbf{R}(\mathcal{P})$ vs. the number of samples M . Computations were performed for an ideal two-element dipole array. 45
3.1	Capacity vs. the transmit power constraint P_T for the proposed discretization approach and worst-case power back-off. The exposure constraint and noise variance are fixed to $Q = 5 \text{ mW/cm}^2$ and $\sigma^2 = 1$, respectively. . . . 54
3.2	Capacity vs. the exposure constraint Q with transmit power $P_T = 10 \text{ mW}$. The transmit SNR is fixed to 0 dB. 55
3.3	Diagram of the considered exposure scenario. A ULA in the xy -plane is located near a spherical head model. The distance between the array and the head is d , and the array is tilted at an angle ϕ . Average PD levels are monitored over the region \mathcal{P} in the xy -plane. For a point p in the region, \mathbf{s} denotes the position vector from the center of the array to p , and \mathbf{s}_n denotes the position vector from the n -th array element to p 57
3.4	Maximum possible PD vs. the distance d at points in the center and edge of the region \mathcal{P} for a transmitter with transmit power $P_T = 10 \text{ mW}$ and $\phi = 90^\circ$ 62
3.5	Average receive SNR vs. the transmit power P_T for the different power back-off schemes applied to a DFT codebook. The exposure constraint is $Q = 4 \text{ mW/cm}^2$ and the noise variance $\sigma^2 = 1$. The distance d is uniformly distributed in $[4, 6]$ mm and the tilt angle is as $\phi = 90^\circ$ 63

Figure	Page
3.6 Average receive SNR vs. the transmit power P_T for the different power back-off schemes applied to a DFT codebook. The exposure constraint is $Q = 4 \text{ mW/cm}^2$ and the noise variance $\sigma^2 = 1$. The distance d and the angle ϕ are uniformly distributed in the ranges $[4, 6] \text{ mm}$ and $[60^\circ, 120^\circ]$, respectively.	65
4.1 Average receive SNR vs. transmit power P for a SAR-constrained 2x8 MIMO system. The proposed perturbation methods and the power back-off methods are applied to the optimal exposure-unaware beamformer. . . .	78
4.2 Main beam back-off factor vs. transmit power P for a SAR-constrained 2x8 MIMO system.	79
4.3 Average receive SNR vs. transmit power P for a 2x8 MIMO system with two SAR constraints. The proposed perturbation methods and the power back-off methods are applied to the optimal exposure-unaware beamformer. . . .	81
4.4 Average receive SNR vs. transmit power P for a 4x16 MIMO millimeter wave system with an incident PD constraint. The proposed perturbation methods and the power back-off methods are applied to a DFT codebook.	82
4.5 Normalized array gain achieved by the exposure-aware beamforming methods.	83

ABBREVIATIONS

5G	Fifth-Generation
5GNR	Fifth-Generation New Radio
AWGN	Additive White Gaussian Noise
AOA	Angle of Arrival
AOD	Angle of Departure
AOI	Angle of Incidence
CSI	Channel State Information
DFT	Discrete Fourier Transform
FCC	Federal Communications Commission
FDD	Frequency Division Duplexing
FFT	Fast Fourier Transform
HFSS	High-Frequency Structure Simulator
ICNIRP	International Commission on Non-Ionizing Radiation Protection
IDFT	Inverse Discrete Fourier Transform
i.i.d.	Independent and Identically Distributed
KKT	Karush-Kuhn-Tucker
LIDAR	LIght Detection and RAnging
LTE	Long-Term Evolution
MaxC	Maximum Correlation
MIMO	Multiple-Input Multiple-Output
MinD	Minimum Distance
MRC	Maximum Ratio Combining
MSE	Mean-Square-Error
NFGCF	Near-Field Gain Correction Factor

PD	Power Density
QCQP	Quadratically Constrained Quadratic Program
RF	Radio Frequency
SAR	Specific Absorption Rate
SNR	Signal-to-Noise-Ratio
SPW	Single Plane Wave
ULA	Uniform Linear Array

ABSTRACT

Castellanos Llorca, Miguel Rodrigo. PhD, Purdue University, May 2020. Exposure-Aware Signal Design for Millimeter Wave MIMO Communication Systems. Major Professors: Dr. David J. Love and Dr. Borja Peleato.

All wireless devices expose users to some level of electromagnetic radiation during operation. In many countries, exposure levels are strictly regulated to ensure the safety of consumers. Previous research demonstrates that incorporating exposure constraints into transmit signal design leads to substantial capacity gains over traditional power back-off techniques. This is especially vital for millimeter wave systems, which require large array gains to combat high path losses and are more susceptible to a decrease in transmit power. In this work, we present exposure modeling procedures and exposure-aware transmission schemes for millimeter wave systems. We first develop methods to approximate the characteristic matrix of a quadratic model for two exposure measures in the millimeter wave band: incident power density and surface specific absorption rate (SAR). The proposed models can be calculated with a small number of parameters and can be altered to account for changes in the exposure scenario. Software simulations with half-wave dipole antennas corroborate the accuracy of the exposure models in the millimeter wave band. We then exploit the ability of the model to calculate exposure at any point surrounding the device to develop efficient exposure-aware signaling strategies. Finally, we propose a low-complexity perturbation approach to obtain exposure-compliant beamforming vectors. Analytical and numerical results demonstrate that the proposed exposure-aware signaling techniques outperform power reduction approaches.

1. INTRODUCTION

In recent years, the unprecedented growth in mobile data traffic has led to an increasingly congested sub-6 GHz spectrum. The expected large throughput demands for future cellular systems have motivated efforts to exploit the wide bandwidths available in the millimeter wave band (roughly 20-100 GHz) to achieve multi gigabit-per-second data rates [1–3]. Millimeter wave systems experience higher path loss compared to lower frequency systems and additional losses from atmospheric gas and rain absorption [4]. Fortunately, the small wavelengths of millimeter wave signals allow devices to provide large beamforming gains through large-sized arrays comprising relatively small antenna elements.

Millimeter wave technologies will play a pivotal role in fifth-generation (5G) wireless communication systems. Millimeter wave frequencies are ideal candidates for wireless backhaul and access in small cell deployments due to the short-range and highly directional nature of millimeter wave propagation [5, 6]. Additionally, millimeter wave vehicular communication systems can take advantage of high data rate transmissions to exchange raw, high-resolution sensor data obtained from radars, cameras, and LIDARs (LIght Detection and RAnging) [7, 8]. One key consideration for millimeter wave communication is the design of beamforming schemes that are tailored to the sparse structure of millimeter wave channels and the hardware limitations at these carrier frequencies. In this context, a variety of studies have addressed practical and efficient precoding methods for millimeter wave systems [1, 5, 9–16].

An additional, less explored challenge in the implementation of millimeter wave systems is the measurement and regulation of electromagnetic exposure to users. Electromagnetic waves emanated from wireless devices are absorbed by users at all frequencies. In the radio and microwave frequency bands, this radiation is non-ionizing; the main effect is heating of body tissues. Even so, biological experts generally agree

that adverse health effects can arise from high levels of radio frequency (RF) energy absorption [17]. Radiation exposure is typically limited by governing bodies to prevent hazardous operating conditions for users. Agencies such as the Federal Communications Commission (FCC) and the International Commission on Non-Ionizing Radiation Protection (ICNIRP) set guidelines for maximum allowable exposure and determine appropriate testing methodologies. All wireless devices must comply with these exposure limits before becoming available to the public.

For lower frequency systems, both the FCC and the ICNIRP have adopted specific absorption rate (SAR) as the standard metric for regulatory compliance [18, 19]. SAR measures user electromagnetic exposure as absorbed power per unit mass, with units W/kg. In this manner, SAR quantifies incident electromagnetic radiation and subsequent absorption. The SAR constraint placed on a device is dependent on the type of device and on its usage. At frequencies between 100 KHz and 6 GHz, the FCC SAR limit for RF exposure from portable devices used by the public is a 1.6 W/kg average over any one gram of tissue [20].

Millimeter wave absorption behaves differently, and its regulation requires the use of alternative exposure metrics. Interactions between millimeter waves and the human body and the biological effects arising from such interactions have been the subject of many studies over the past decades [21–27]. The limited penetration of millimeter waves into the body leads to a large concentration of energy deposition in thin layers of exposed tissue such as the skin and the eye, but negligible absorption a few millimeters below the surface. As a result, tissue heating from millimeter wave exposure is largely restricted to a thin tissue layer and can be effectively measured with superficial quantities such as incident power density (PD) and SAR at the tissue surface, commonly referred to as surface SAR. For example, the FCC and ICNIRP have adopted incident PD as the standard exposure metric in the millimeter wave band [18, 19].

Electromagnetic emission management is critical to the safety and success of millimeter wave systems. Incident PD exposures above several hundred mW/cm² can

cause pain in the skin and even ocular lesions [28], and millimeter wave devices limit transmit power to be below 10 dBm to comply with regulatory standards [26]. Recent works related to 5G exposure have addressed the effects of exposure constraints on millimeter wave devices and the advantages of exposure-aware system design [29–32]. Regardless, exposure constraints are typically ignored during system design and later act as secondary power constraints if absorption measurements exceed existing thresholds. Such power limits on user-end devices can cause significant degradation to the system performance, especially since millimeter wave systems need high transmit gains to combat path loss. Fortunately, multiple-input multiple output (MIMO) communication systems can benefit from large exposure variations as a function of signal design and are able to jointly maximize the achievable rate under exposure constraints.

A number of studies have addressed the development and validation of signal-level exposure models. SAR measurement variations with respect to the phase difference between two transmit antennas were first addressed in [33, 34]. Work in [35–38] later demonstrated that SAR can be approximated as a mixed quadratic function of the transmit signal and introduced the notion of an *exposure matrix*, which is the characteristic matrix in the quadratic model. A Fourier analysis based model for fast SAR and power loss density estimation was also proposed and validated in [39]. In [40, 41], a method for determining device compliance with SAR limits in linear time was derived by exploiting the structure of the quadratic model.

Exposure models are important not only for characterizing the exposure induced by wireless devices, but also for imposing exposure constraints on system signal design. In this context, previous research has focused on the design and analysis of exposure-aware transmissions [35–37, 42–46]. In [36], a SAR-aware coding solution is introduced and shown to provide a 2.5 dB improvement in probability of error over the Alamouti code in a SAR-limited system. The problem of finding optimal beamformers and precoders in systems with one or more SAR constraints is presented in [42, 44, 45] and an extension for multi-user systems is presented in [43].

In this dissertation, we focus on the problem of exposure-aware signal design for millimeter wave systems. We first address suitable models for exposure measures employed in the millimeter wave band. We then present two applications of the developed exposure model for exposure-constrained systems. Finally, we develop a new method for exposure-constrained beamforming for systems with limited feedback.

1.1 Signal-Level Models of Electromagnetic Exposure for Millimeter Wave Communication Systems

The aforementioned quadratic model can predict electromagnetic exposure with high accuracy, but computing the model parameters requires a significant amount of overhead. Model parameters are calculated by obtaining exposure measurements — from software simulations or phantom head setups — with a device held in a typical operating condition and then performing a fitting procedure. These parameters are specific to the measurement configuration, including the transmitter array design, the operating frequency, the shape and dielectric properties of the exposed tissue, and how the device is held relative to the exposed tissue. Since emission compliance must be verified over a device’s typical operating conditions, various measurement sets are needed to completely characterize exposure via these models.

This work addresses the issue of constructing low-complexity models for incident PD and surface SAR in the millimeter wave band by deriving formulas to approximate the exposure matrices in the quadratic model proposed in [35–38]. We leverage the relative simplicity of electromagnetic absorption measures at millimeter wave frequencies to develop parametric expressions that only require a few external measurements and that can easily adapt to the testing configuration. We develop a method to calculate incident PD matrices by approximating the near-field gain of the transmitter in terms of basic array parameters and incorporating existing models for mutual coupling and near-field effects. We also derive an expression for SAR matrices by modeling the total electric field transmitted through the air-tissue boundary as the

superposition of incident spherical waves refracted as plane waves through a planar dielectric. The proposed formulas for the characteristic exposure matrices demonstrate how the quadratic model can be represented as a rank-one model in terms of an effective steering vector, which is defined later. To validate the model, we simulate a 28 GHz millimeter wave exposure scenario with a uniform linear array (ULA) composed of half-wave dipoles and a spherical tissue model. Our results demonstrate a high degree of agreement between the quadratic model with the calculated exposure matrices and the simulation measurements.

The proposed models estimate pointwise exposure and are, therefore, not directly compatible with regulatory thresholds, which are defined as averages over predetermined areas or volumes. Thus, a key modeling consideration is how to sample a spatial region to obtain a robust characterization of averaged exposure. We first derive upper bounds on the exposure differential between two testing points based on the proposed models. This result is used to develop uniform and non-uniform spatial sampling guidelines which guarantee variations in exposure measurements at adjacent sample points do not exceed a predetermined threshold. We also discuss how to construct exposure models for average exposure from the sampled pointwise models. Finally, we present numerical examples to demonstrate the application of the developed sampling methods.

1.2 Efficient Signal Design Under Exposure Constraints

One of the key advantages of the exposure model in Chapter 2 is that it provides the system with the ability to calculate exposure at any point surrounding the device. While the problem of optimal exposure-constrained signaling has been addressed in previous studies [42, 43], we consider two scenarios in which the proposed exposure model allows the system to perform efficient exposure-aware transmission schemes.

In the first scenario, we consider a system which is constrained by a large number of exposure constraints corresponding to exposure limits on a large region of the body.

In this case, it may not be practical to perform the optimal precoding strategy as discussed in [42]. We propose a precoding method which combines the optimal solution to a signal design problem with a finite number of exposure constraints found in [42] with a constraint sampling approach. The proposed discretization algorithm iteratively adds maximal exposure testing points as new constraints based on the current optimal precoder and converges to a near-optimal solution after a small number of iterations.

The optimal exposure-constrained signaling schemes are highly effective but require complex optimizations and high-resolution digital beamforming architectures. A more basic alternative is to reduce the transmit power to comply with exposure limits. While suboptimal, this approach is highly practical and limits the system computational load. In its simplest form, power back-off is implemented on a worst-case basis, i.e., the transmit power is reduced so that exposure lies below the regulatory threshold regardless of the transmit signal and gesture. However, EM exposure is not static; levels can vary significantly with changes in the transmit signal and the relative device location. Worst-case power back-off unnecessarily deteriorates the uplink performance in many cases.

Power back-off can also be applied adaptively depending on the current exposure in order to minimize the performance loss associated with power reduction. Previous studies have addressed adaptive power back-off with respect to the transmit signal [35, 42]. However, modern wireless devices are equipped with a variety of proximity sensors and can determine not only when the device is near the user's head but also how close the user is to the device [47]. Systems may be able to use this information to adjust power levels as a function of the relative device position.

In second scenario, we consider a codebook-based deployment in which the exposure induced by the device varies due to changes in its position relative to the user. We propose a method for adaptively regulating the transmit power of a millimeter wave system to mitigate user exposure. We employ the low-complexity model proposed in Chapter 2 to recalculate the codebook exposure whenever the device location

relative to the user changes. Note that while the proposed scheme is applicable at any frequency, we rely on the expressions developed in Chapter 2 to calculate exposure. The exposure measures considered in the model, namely SAR at the tissue surface and PD, are typically only used for above-6 GHz systems. To reduce the computational load on the system, we also propose the use of a discrete Fourier Transform (DFT) codebook for data transmission. The codebook structure is leveraged to derive a fast Fourier Transform (FFT) method for calculating the exposure induced by each beam in the codebook. Simulation results demonstrate that adjusting the beam power depending on the distance from the user yields notable gains in performance.

1.3 Beamforming Perturbation Approach for Mitigating User Exposure

Previous studies have mainly focused on optimal signaling schemes over exposure-constrained channels, but these schemes may not be realizable in the uplink for certain deployments. Optimal beamforming with exposure limits requires both perfect instantaneous CSI and complete knowledge of the exposure constraint. Channel information is often not available at the transmitter due to feedback constraints and lack of reciprocity in frequency division duplexing (FDD) systems. In such cases, the base station is often tasked with determining a suitable beamformer for the user, and a limited feedback channel can be employed to convey this information to the user. Optimal exposure-aware beamforming would require the base station to know the exposure characteristics of the user, which are typically specified as multiple quadratic forms with corresponding exposure matrices [42]. Feedback of the exposure matrices is not practical since the size of these matrices grows quadratically with the number of antennas in the user device and the exposure constraint may be characterized by multiple exposure matrices. Therefore, the necessary components for exposure-aware beamforming are typically not available at the same location.

We leverage existing signal-level exposure models to develop a low-complexity exposure reduction scheme. Rather than decreasing the transmit power of a given

beamforming vector to comply with exposure limits, we apply a small perturbation to obtain an exposure-compliant beamformer while minimizing the beamforming gain loss. We show that the perturbed beamformer can be viewed as the sum of the original beam with reduced power and an orthogonal component which mainly acts to decrease exposure. Our analytical and simulation results demonstrate that the proposed exposure reduction approach outperforms traditional power back-off methods. In contrast to optimal exposure-constrained beamforming, the proposed perturbation technique does not require channel knowledge and can be applied to systems employing beamforming codebooks. Therefore, the proposed scheme offers a practical solution to the problem of exposure management and can be easily implemented in real systems, including standards-compliant LTE-Advanced and 5G NR devices.

1.4 Organization

This dissertation is organized as follows. In Chapter 2, we develop low-complexity approaches to calculate exposure models suitable for millimeter wave exposure scenarios. We review prior work on signal-level exposure modeling and present our proposed approaches for computing exposure matrices in the millimeter wave band. We present software simulation results of a simple millimeter wave exposure scenario to validate the proposed models. Spatial sampling techniques and the characterization of spatially averaged exposure are also discussed.

In Chapter 3, we present two applications of the proposed signal-level exposure model. We first propose a discretization-based iterative approach to obtain the optimal precoder for an exposure-constrained channel. We then present a distance-adaptive power back-off techniques that leverages the capabilities of the models developed in Chapter 2. We present simulation results for our proposed transmission method and compare the performance with traditional power back-off techniques.

In Chapter 4, we propose two exposure-aware perturbation schemes for MIMO systems. Analytical results demonstrate that the proposed approaches allow the

system to transmit with higher power in the original beamforming direction compared to power back-off techniques. Simulations demonstrate that the perturbation methods achieve substantial gains over power reduction methods and perform nearly optimally in certain cases.

1.5 Notation

A bold lowercase letter \mathbf{a} denotes a column vector, a bold uppercase letter \mathbf{A} denotes a matrix, \mathbf{A}^T denotes the transpose of \mathbf{A} , \mathbf{A}^H denotes the conjugate transpose of \mathbf{A} , $\|\mathbf{a}\|$ denotes the vector 2-norm of \mathbf{a} , $\|\mathbf{A}\|_2$ denotes the induced vector 2-norm of \mathbf{A} . $\mathbf{A} = \text{diag}(a_0, a_1, \dots, a_{N-1})$ denotes the diagonal matrix \mathbf{A} with diagonal entries given by a_0, a_1, \dots, a_{N-1} . For a complex number z , $\text{Re}\{z\}$ and $\text{Imag}\{z\}$ denote the real and imaginary parts of z , respectively.

2. SIGNAL-LEVEL MODELS OF ELECTROMAGNETIC EXPOSURE FOR MILLIMETER WAVE COMMUNICATION SYSTEMS

2.1 Procedures for Computing Signal-Level Exposure Models

We briefly review the results of prior exposure modeling studies in [35–39] and define the notion of an exposure matrix. We then present our proposed procedures for calculating exposure matrices for pointwise incident PD and surface SAR. The measurements required to compute exposure matrices with both the prior and the proposed methods are discussed and compared.

2.1.1 Review of Prior Art

Wireless devices sold worldwide are thoroughly tested for compliance with regulatory standards for maximum user exposure. These limits are often set conservatively to ensure that electromagnetic radiation absorbed by users does not cause biologically significant thermal heating. For systems operating below 6 GHz, exposure measurements are typically expressed in terms of SAR. SAR is a measure of power absorbed in human tissue per unit mass at a point \mathbf{p} and is expressed as

$$\text{SAR}(\mathbf{p}) = \frac{\sigma |\mathcal{E}_m(\mathbf{p})|^2}{2\rho}, \quad (2.1)$$

where σ is the tissue conductivity, $\mathcal{E}_m(\mathbf{p})$ is the electric field strength, and ρ is the density of the tissue [48].

©[2019] IEEE. Reprinted, with permission, from M. R. Castellanos, Y. Liu, D. J. Love, B. Peleato, J. M. Jin, and B. M. Hochwald, “*Signal-Level Models of Pointwise Electromagnetic Exposure for Millimeter Wave Communication*,” accepted in IEEE Transactions on Antennas and Propagation, June 2019.

In a multi-antenna system, SAR values can vary significantly with respect to the transmit signal. Let N be the number of transmitter antennas, and let \mathbf{x} be the length N transmit signal vector. Experimental results in [35–39] show that average SAR measurements over a volume V are well approximated as a quadratic function of the transmit signal \mathbf{x} as

$$\text{SAR}_V(\mathbf{x}) = \mathbf{x}^H \mathbf{R}_V \mathbf{x}, \quad (2.2)$$

where \mathbf{R}_V is the $N \times N$ matrix that characterizes the variation of SAR with respect to \mathbf{x} within the volume. Various studies have shown that incorporating SAR constraints into signal design problems by employing the quadratic model yields significantly higher rates compared to conventional power back-off schemes which lower the transmit power to satisfy exposure constraints [35–37, 42–45].

In (2.2), the SAR matrix \mathbf{R}_V is obtained by a fitting method, such as a least-squares algorithm, on measured SAR data. Since regulatory agencies place limits on the worst-case exposure, the volume is chosen such that it corresponds to the maximum region of absorption. Changing the transmission frequency or the location of the wireless device relative to the body can change the location of the hotspot [37]. Therefore, different operating conditions must be modeled by different SAR matrices, all of which require additional exposure data.

Constructing sub-6 GHz SAR models requiring less measurements/simulations is challenging given the complex nature of electromagnetic absorption at these frequencies. Electromagnetic radiation at lower frequencies can reach past the dermal and subcutaneous skin layers, and maximum SAR measurements are typically found inside the body. For example, emissions from a portable device operating near the head often induce SAR hotspots inside of the skull. Cooling mechanisms such as blood flow can also significantly reduce intrabody tissue heating and affect the location of maximum exposure.

In contrast, the submillimeter penetration depths of millimeter waves lead to extremely large local SAR values at the tissue surface, but only about 40-60% of incident power is able to reach past 0.1 mm [26]. The superficial nature of millimeter

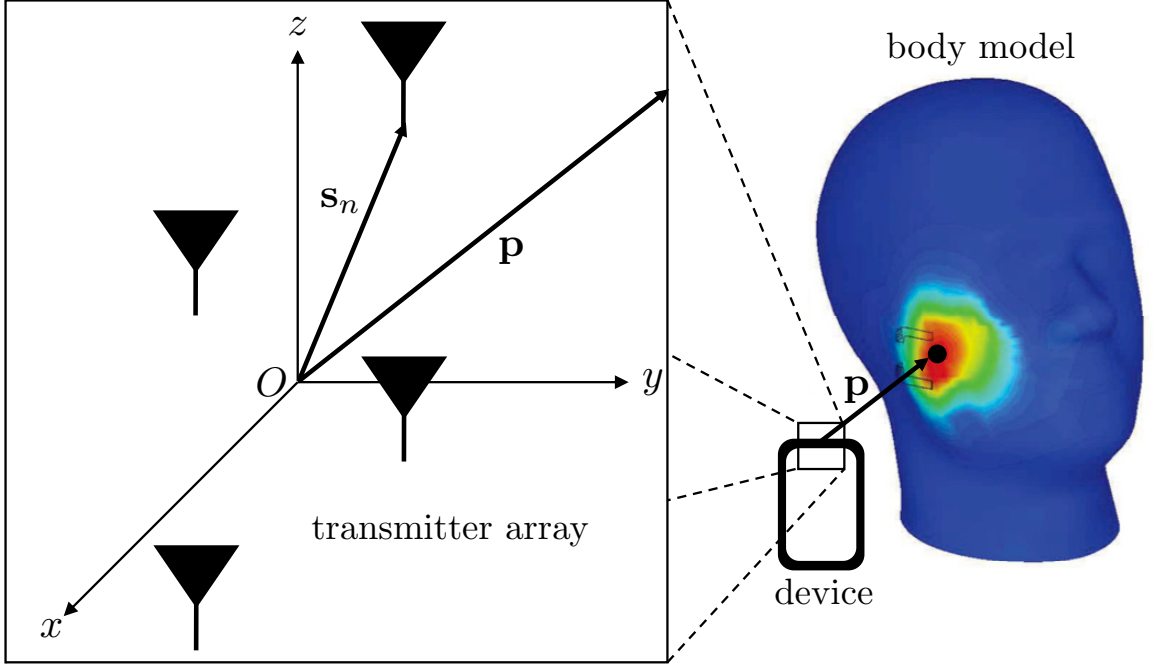


Fig. 2.1. A diagram of the considered exposure scenario. A body model lies close to an N element transmitter array. The position of the n -th element is \mathbf{s}_n , and exposure is measured at a point \mathbf{p} on the body surface.

wave absorption suggests tissue heating is heavily dependent on incident PD and surface SAR values, which are markedly easier to understand and model than SAR readings at points deep in the body.

In the remainder of this study, we construct and analyze low-complexity signal-level models for incident PD and surface SAR by exploiting the simple nature of these exposure measures. Although these models are valid at all frequencies, the main motivation for this work is to develop signal-level models that can be easily incorporated into the design of exposure-aware transmission schemes such as those proposed in [35–37, 42–45]. As incident PD and surface SAR are not robust measures of exposure for lower frequencies, the proposed models may not be useful for this application for sub-6 GHz devices. Therefore, we mainly focus on the models in the context of millimeter wave systems.

2.1.2 Proposed Methods for Computing Exposure Matrices

Both incident PD and surface SAR are proportional to the squared electric field magnitude, therefore either dosimetric quantity can be characterized as a quadratic function of a transmit signal \mathbf{x} as

$$\text{EXP}(\mathbf{p}, \mathbf{x}) = \mathbf{x}^H \mathbf{R}(\mathbf{p}) \mathbf{x}, \quad (2.3)$$

where EXP is the exposure measure, \mathbf{p} is the measurement point, and $\mathbf{R}(\mathbf{p})$ is the $N \times N$ characteristic exposure matrix for the point \mathbf{p} . We precede the development and justification of the proposed models by outlining how to compute the exposure matrix $\mathbf{R}(\mathbf{p})$ at a point \mathbf{p} . In the considered exposure scenario, an N element antenna array is in the vicinity of an arbitrary tissue model and exposure is measured at a point \mathbf{p} on the body surface, as shown in Fig. 2.1. The position of the n -th array element and the vector from the n -th element to \mathbf{p} are denoted as \mathbf{s}_n and $\mathbf{p}_n = \mathbf{p} - \mathbf{s}_n$, respectively. The phase center of the array, given as $\sum_{n=0}^{N-1} \mathbf{s}_n$ [49], is assumed to lie at the origin for convenience.

Table 2.1 lists the necessary model parameters, drawing a distinction between those which are known or measured, and those which are calculated. Parameters related to the antenna gain, such as the gain patterns and the array coupling matrix, are assumed to be normalized with respect to the transmit power. Additionally, the transmit signal \mathbf{x} is assumed to be unit-norm. The following procedures provide a step-by-step guides for calculating the matrix $\mathbf{R}_{\text{EXP}}(\mathbf{p})$.

Procedure for Computing PD Matrices: To compute the plane wave equivalent PD matrix $\mathbf{R}_{\text{PD}}(\mathbf{p})$, follow the steps below:

1. Calculate the near-field steering vector $\mathbf{a}(\mathbf{p})$, which is defined as [49]

$$\mathbf{a}(\mathbf{p}) \triangleq \left[\gamma_0 e^{-j\varphi_0} \quad \gamma_1 e^{-j\varphi_1} \quad \dots \quad \gamma_{N-1} e^{-j\varphi_{N-1}} \right]^T, \quad (2.4)$$

where φ_n and γ_n are given by

$$\varphi_n = \frac{2\pi (\|\mathbf{p}_n\| - \|\mathbf{p}\|)}{\lambda}, \quad (2.5)$$

Table 2.1.

List of model parameters.

Measured/Known Parameters	Description
λ	Transmission wavelength (m)
$g_n(\mathbf{p})$	Gain pattern of the n -th antenna element
P	Transmit power (W)
$\alpha(\ \mathbf{p}\)$	Near-field gain correction factor
\mathbf{M}	Array coupling matrix
ϵ^*	Relative complex tissue dielectric constant
ρ	Tissue density (kg/m ³)
Calculated Parameters	
$\mathbf{a}(\mathbf{p})$	Near-field steering vector
ζ_n^i	Angle of incidence from n -th source to \mathbf{p}
τ_n	Transmission coefficient for n -th source at \mathbf{p}

$$\gamma_n = g_n^{1/2}(\mathbf{p}_n) \frac{\|\mathbf{p}\|}{\|\mathbf{p}_n\|}. \quad (2.6)$$

If the gain patterns $g_n(\mathbf{p}_n)$ are near-field gain patterns, then set $\gamma_n = g_n^{1/2}(\mathbf{p}_n)$.

2. If coupling between array elements is to be modeled, determine a suitable coupling matrix \mathbf{M} . Otherwise set $\mathbf{M} = \mathbf{I}$.
3. If the gain pattern $g(\mathbf{p})$ was measured in the far-field, determine an appropriate scaling coefficient $\alpha(\|\mathbf{p}\|)$ to correct for differences between the near-field and far-field array gain. Otherwise set $\alpha(\|\mathbf{p}\|) = 1$.

4. Calculate the PD matrix $\mathbf{R}_{\text{PD}}(\mathbf{p})$ as

$$\mathbf{R}_{\text{PD}}(\mathbf{p}) = \frac{P\alpha(\|\mathbf{p}\|)}{4\pi\|\mathbf{p}\|^2} \mathbf{M}^H \mathbf{a}(\mathbf{p}) \mathbf{a}^H(\mathbf{p}) \mathbf{M}. \quad (2.7)$$

Procedure for Computing Surface SAR Matrices: To compute the surface SAR matrix $\mathbf{R}_{\text{SAR}_0}(\mathbf{p})$, follow the steps below:

1. Calculate the PD matrix $\mathbf{R}_{\text{PD}}(\mathbf{p})$.
2. Determine angles of incidence (AoIs) ζ_n^i from the sources to the point \mathbf{p} based on the tissue model.
3. Calculate the corresponding transmission coefficients τ_n assuming the incident wavefronts are plane waves, and define the diagonal $N \times N$ matrix \mathbf{T} as

$$\mathbf{T} = \text{diag}(\tau_0, \tau_1, \dots, \tau_{N-1}). \quad (2.8)$$

For TE and TM polarized radiation, τ_n is given as

$$\begin{aligned} \tau_{n,\text{TE}} &= \frac{2 \cos \zeta_n^i}{\cos \zeta_n^i + \sqrt{\epsilon^* - \sin^2 \zeta_n^i}}, \\ \tau_{n,\text{TM}} &= \frac{2\sqrt{\epsilon^*} \cos \zeta_n^i}{\epsilon^* \cos \zeta_n^i + \sqrt{\epsilon^* - \sin^2 \zeta_n^i}}. \end{aligned} \quad (2.9)$$

4. Calculate the surface SAR matrix as

$$\mathbf{R}_{\text{SAR}_0}(\mathbf{p}) = \frac{\eta_0 \sigma}{\rho} \mathbf{T}^H \mathbf{R}_{\text{PD}}(\mathbf{p}) \mathbf{T}, \quad (2.10)$$

where η_0 is the intrinsic impedance of free space given by 377Ω . Note that the tissue conductivity σ can be calculated from $\epsilon^* = \epsilon' - j\epsilon''$ as

$$\sigma = \omega \epsilon_0 \epsilon'', \quad (2.11)$$

where ω is the transmission angular frequency and ϵ_0 is the permittivity of free space given by 8.85×10^{-12} F/m.

Apart from ϵ^* , all of the non-calculated parameters involved in these procedures are related to the transmitter and can be easily obtained from standard array measurements/simulations. Tissue permittivity measurements in the millimeter band are sparse due to technical limitations, but various studies have addressed models for human skin complex permittivity at millimeter wave frequencies [21, 22, 25, 27]. Note that the measured parameters do not depend on the location of the user relative to the transmitter. Therefore, exposure matrices for various operating conditions can be computed with the same set of parameters.

2.2 Millimeter Wave Exposure Modeling

In this section, we derive the formulas for calculating exposure matrices provided in Section 2.1.2. The problem of modeling pointwise incident PD and surface SAR is equivalent to estimating the incident and transmitted electric field across the body surface. Therefore, our objective is to approximate the near-field array pattern and the transmission of energy through the air-tissue boundary.

2.2.1 Incident Power Density

Most regulatory agencies have adopted incident PD as the main exposure metric in the millimeter band [18, 19]. PD measurements are typically estimated by converting field strength measurements to plane wave equivalent PDs, and can be calculated as

$$S(\mathbf{p}) = \frac{|\mathcal{E}_m(\mathbf{p})|^2}{2\eta_0} = \frac{|\mathcal{H}_m(\mathbf{p})|^2}{2}\eta_0, \quad (2.12)$$

where $\mathcal{E}_m(\mathbf{p})$ is the electric field strength and $\mathcal{H}_m(\mathbf{p})$ is the magnetic field strength. Throughout this chapter, it is assumed that PD refers to plane wave equivalent PD. Incident PD limits are often referred to as maximum permissible exposures (MPEs) in regulatory standards [18]. We derive an expression to compute the incident PD matrix $\mathbf{R}_{\text{PD}}(\mathbf{p})$ for the quadratic model

$$S(\mathbf{p}, \mathbf{x}) = \mathbf{x}^H \mathbf{R}_{\text{PD}}(\mathbf{p}) \mathbf{x} \quad (2.13)$$

at a point \mathbf{p} located near the transmitter array.

Since incident PD is proportional to $|\mathcal{E}_m(\mathbf{p})|^2$, calculating PD matrices requires minimal work if the variations in the transmitter array's radiated electric field as a function of \mathbf{p} and \mathbf{x} are known. However, this information is not always readily available and can be difficult to measure. Therefore, we focus on a more practical scenario in which only the gain patterns of the individual antenna elements are known. The initial assumptions for the model development are as follows:

(A1) \mathbf{p} is in the far-field of the antenna elements.

(A2) the antenna elements in the array are uncoupled.

Far-field conditions are dependent on the transmission wavelength λ and the array size. The general conditions for (A1) to hold are $\|\mathbf{p}\| > 2W_{\max}^2/\lambda$, $\|\mathbf{p}\| \gg W_{\max}$, and $\|\mathbf{p}\| \gg \lambda$, where W_{\max} is the maximum linear dimension of the antenna elements. Some cases where (A2) holds include arrays with inter-element spacing that is large relative to λ and arrays fed by decoupling networks.

Incident PD at a point \mathbf{p} can be expressed in terms of array parameters as

$$S(\mathbf{p}, \mathbf{x}) = \frac{PG(\mathbf{p}, \mathbf{x})}{4\pi\|\mathbf{p}\|^2}, \quad (2.14)$$

where P is the transmit power and $G(\mathbf{p}, \mathbf{x})$ is the array gain. In cases where (A1) and (A2) hold, the array gain can be obtained by the principle of pattern multiplication as

$$G(\mathbf{p}, \mathbf{x}) = \left| \mathbf{a}^H(\mathbf{p})\mathbf{x} \right|^2, \quad (2.15)$$

where $\mathbf{a}(\mathbf{p})$ is the length N transmitter steering vector and \mathbf{x} is the unit-norm length N transmit signal [50]. In (2.15), the term $\mathbf{a}^H(\mathbf{p})\mathbf{x}$ is often referred to as the array factor, which accounts for differences in the phase and amplitude of the radiated fields. Note that the individual gain patterns are absorbed in the steering vector.

Steering vectors typically represent the set of phase delay differences corresponding to the radiated fields from each source and ignore path loss differences between wavefronts. This is only applicable far from the array, as the path lengths from each

transmitter element to \mathbf{p} may differ significantly when the point of interest is close to the array. These path length variations result in non-negligible attenuation differences between the waves which must be accounted for to calculate the array gain at \mathbf{p} . The steering vector is therefore constructed to represent the gains and phase delays differences between spherical wavefronts as they impinge on \mathbf{p} and is defined as in (2.4). Note that $\mathbf{a}(\mathbf{p})$ is given in a general form that adapts to both the array geometry and the elements' gain patterns.

A characteristic matrix $\mathbf{R}_{\text{PD}}(\mathbf{p})$ for the quadratic model of ideal incident PD can be defined using the expressions above as

$$\mathbf{R}_{\text{PD,ideal}}(\mathbf{p}) \triangleq \frac{P}{4\pi\|\mathbf{p}\|^2} \mathbf{a}(\mathbf{p})\mathbf{a}^H(\mathbf{p}). \quad (2.16)$$

The matrix $\mathbf{R}_{\text{PD,ideal}}(\mathbf{p})$ is a Hermitian, positive semi-definite matrix by construction. Note that the dominant eigenvector of the ideal PD matrix is a scalar multiple of the near-field array steering vector $\mathbf{a}(\mathbf{p})$, and maximum exposure occurs when \mathbf{x} is aligned with $\mathbf{a}(\mathbf{p})$. This agrees with the intuition that plane wave equivalent PD is directly proportional to the array gain.

The characteristic matrix given in (2.16) is accurate under (A1) and (A2), but many exposure scenarios do not fall under these assumptions. Both near-field field components and mutual coupling can significantly affect array patterns and radiation emissions. We add correction factors to (2.16) to address both of these issues.

The near-field region of an array is characterized by complex field components that decrease with distance faster than $1/\|\mathbf{p}\|$. This results in gain patterns whose shape can vary significantly with distance from the source. In antenna measurement procedures where far-field conditions cannot be met, a gain pattern $G_{\text{nf}}(\mathbf{p})$ is measured in the near-field and the far-field gain pattern is approximated from the model

$$G_{\text{ff}}(\theta, \phi) \approx \alpha^{-1}(\|\mathbf{p}\|)G_{\text{nf}}(\mathbf{p}), \quad (2.17)$$

where θ and ϕ are the elevation and azimuth angles of \mathbf{p} , respectively, and $\alpha(\|\mathbf{p}\|) \in \mathbb{R}_{>0}$ is the near-field gain correction factor (NFGCF) [51]. This only gives an estimate for the far-field gain since the NFGCF only varies with distance, but the

error between the near-field and far-field gain patterns may have a directional dependence. The near-field gain converges to the far-field gain at large distances, therefore $\lim_{\|\mathbf{p}\| \rightarrow \infty} \alpha(\|\mathbf{p}\|) = 1$. The NFGCF can be estimated empirically by comparing measured data with theoretical gain curves that decay as $1/\|\mathbf{p}\|^2$ [51].

Array elements are often mutually coupled and act as parasitic elements that absorb and reradiate outgoing waves. A popular and simple method for modeling the field pattern of a coupled array is through an $N \times N$ coupling matrix \mathbf{M} [52–54]. Let $\{\mathcal{E}_{n,\text{uc}}(\mathbf{p})\}_{n=0}^{N-1}$ denote the uncoupled three-dimensional electric field pattern of the array elements obtained from a unit excitation. The coupled array field pattern can be found as

$$\mathcal{E}_c(\mathbf{p}) = \mathcal{E}_{\text{uc}}(\mathbf{p})\mathbf{M}\mathbf{x}, \quad (2.18)$$

where $\mathcal{E}_{\text{uc}} = [\mathcal{E}_{0,\text{uc}}, \dots, \mathcal{E}_{N-1,\text{uc}}]$. In general, the coupling matrix cannot be determined exactly and must be estimated as in [52, 53]. Additionally, the coupling matrix \mathbf{M} may vary depending on \mathbf{p} . However, we assume that \mathbf{M} remains relatively constant over the exposed region of interest.

Incident PD Model: With the above models for ideal PD, near-field gain, and mutual coupling, the corrected characteristic exposure matrix to compute incident PD as $\mathbf{x}^H \mathbf{R}(\mathbf{p}) \mathbf{x}$ is defined as

$$\begin{aligned} \mathbf{R}_{\text{PD}}(\mathbf{p}) &\triangleq \alpha(\|\mathbf{p}\|) \mathbf{M}^H \mathbf{R}_{\text{PD,ideal}}(\mathbf{p}) \mathbf{M} \\ &= \frac{P\alpha(\|\mathbf{p}\|)}{4\pi\|\mathbf{p}\|^2} \mathbf{M}^H \mathbf{a}(\mathbf{p}) \mathbf{a}^H(\mathbf{p}) \mathbf{M}. \end{aligned} \quad (2.7 \text{ revisited})$$

The corrected matrix better approximates incident power density in non-ideal scenarios as shown in Section 2.3.2. It can also be seen that the corrected and uncorrected models agree under (A1) and (A2) since $\mathbf{R}_{\text{PD}}(\mathbf{p}) = \mathbf{R}_{\text{PD,ideal}}(\mathbf{p})$ when $\alpha(\|\mathbf{p}\|) = 1$ and $\mathbf{M} = \mathbf{I}$. The model in (2.7) is able to predict pointwise exposure with only prior knowledge of array parameters which are typically measured during the transmitter design. Note that the model not only predicts PD as a function of the transmit signal, but also as a function of space.

It can be seen that the PD matrix is rank-one by construction, and therefore it can be expressed as the outer product of its dominant eigenvector as $\mathbf{R}_{\text{PD}}(\mathbf{p}) = \mathbf{r}(\mathbf{p})\mathbf{r}^H(\mathbf{p})$. In the ideal PD model, this eigenvector is colinear with the array steering vector $\mathbf{a}(\mathbf{p})$, whereas the coupling matrix and NFGCF rotate and scale the $\mathbf{a}(\mathbf{p})$ in the non-ideal scenario. In both cases, maximum exposure occurs when the transmit signal is aligned with the dominant eigenvector of the PD matrix, which can be expressed as a linear transformation of $\mathbf{a}(\mathbf{p})$. This motivates the notion of an *effective array steering vector* for a given exposure measure, which is defined as the vector $\hat{\mathbf{a}}_{\text{EXP}}(\mathbf{p})$ such that

$$\text{EXP}(\mathbf{p}, \mathbf{x}) = \frac{|\hat{\mathbf{a}}_{\text{EXP}}^H(\mathbf{p})\mathbf{x}|^2}{\|\mathbf{p}\|^2}. \quad (2.19)$$

Note that for the proposed PD matrix, the effective array steering vector is given as

$$\hat{\mathbf{a}}_{\text{PD}}(\mathbf{p}) = \sqrt{\frac{P\alpha(\|\mathbf{p}\|)}{4\pi}}\mathbf{M}^H\mathbf{a}(\mathbf{p}), \quad (2.20)$$

and so incident PD can be defined as the rank-one model

$$S(\mathbf{p}, \mathbf{x}) = \frac{|\hat{\mathbf{a}}_{\text{PD}}^H(\mathbf{p})\mathbf{x}|^2}{\|\mathbf{p}\|^2}. \quad (2.21)$$

PD calculations are relatively easy to perform for compliance, but they do not contain information about energy absorption in tissues. Incident electromagnetic waves are partially reflected when incident on dielectric media, which leads to significant differences in absorption for oblique incidence versus tangent incidence. Because of this, we consider SAR at the tissue surface as an alternative measurement for radiation absorption.

2.2.2 Specific Absorption Rate

SAR is a more robust measure of exposure than incident PD since it captures the rate of energy absorption in tissues. Unlike incident PD, SAR must be measured, not calculated, with the device operating in its intended manner at full transmit power. Current methodologies require measuring SAR values in a phantom head

while the wireless device is held in a variety of operating conditions. Although current averaging volumes for SAR may not yield measurements that are useful for determining compliance in millimeter wave systems, SAR values at the tissue surface may serve as a suitable measure of energy deposition.

For a plane wave with power density $S(\mathbf{p}, \mathbf{x})$ incident on a point \mathbf{p} on the surface of planar tissue, the pointwise surface SAR, denoted as SAR_0 is given as

$$\text{SAR}_0(\mathbf{p}, \mathbf{x}) = \frac{2TS(\mathbf{p}, \mathbf{x}) \cos \zeta^i}{\rho\delta}, \quad (2.22)$$

where T is the power transmission coefficient of the skin, ζ^i is the angle of incidence (AoI), and δ is the skin depth [21]. The skin depth is defined as the distance that electromagnetic radiation travels into a material before its power decreases to $\exp(-2)$ of its surface value and is given by

$$\delta = \frac{\lambda}{-2\pi \text{Im}\{\sqrt{\epsilon^*}\}}, \quad (2.23)$$

where ϵ^* is the complex dielectric constant of the tissue [55]. Small penetration depths also lead to radiation absorption in tissue decreasing exponentially from the skin as

$$\text{SAR}(\mathbf{p}, \mathbf{x}, \xi) = \text{SAR}_0(\mathbf{p}, \mathbf{x})e^{-2\xi/\delta}, \quad (2.24)$$

where ξ is the depth from the tissue surface [21]. Maximum exposure occurs at the surface of the tissue and quickly decays within the skin.

The expression in (2.22) is heavily dependent on the AoI ζ^i . Far from the array, this can be approximated as the AoI from the center of the array to \mathbf{p} because all path lengths $\|\mathbf{p}_k\|$ are approximately the same. We denote the surface SAR model in (2.22) with ζ^i calculated in this manner as the single plane wave (SPW) SAR model, since the incident radiation at \mathbf{p} is assumed to be a plane wave with power density $S(\mathbf{p}, \mathbf{x})$.

The approximations of the SPW model may lead to poor SAR estimates when \mathbf{p} is close to the array. For example, if \mathbf{p} is much closer to one of the array elements than to any other antenna, then ζ^i cannot be estimated as above. Moreover, the assumption that the incident wavefront behaves like a plane wave may not hold in

general. Rather than computing surface SAR by finding the incident field at \mathbf{p} , we propose finding the total transmitted field as a superposition of the transmitted fields from each source.

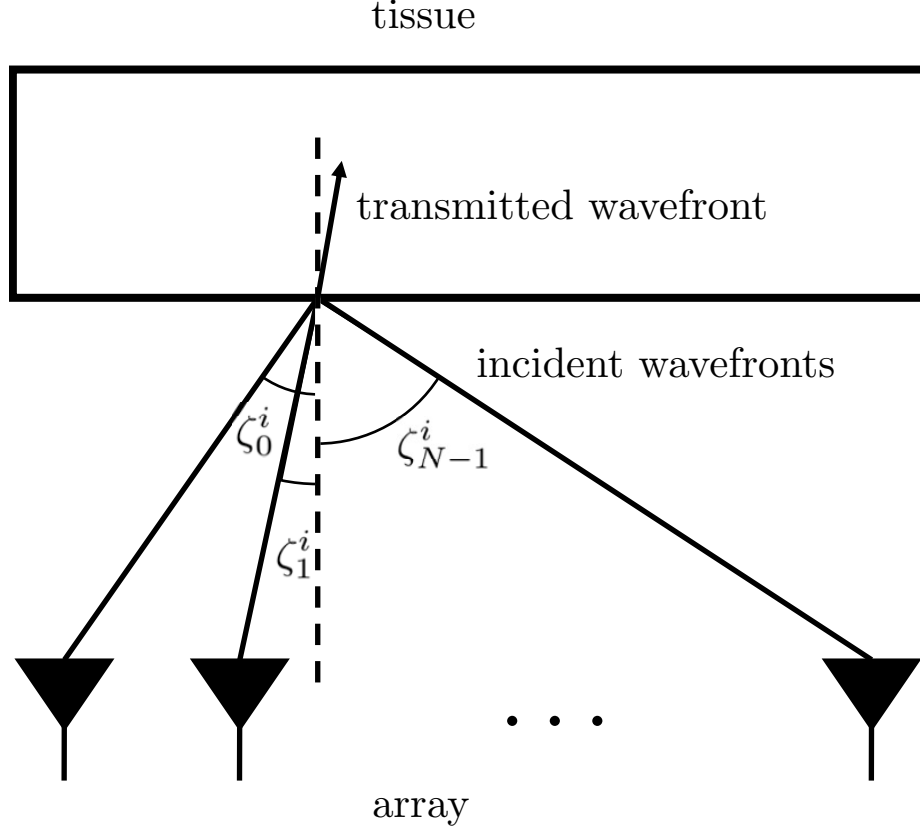


Fig. 2.2. Diagram of the considered electromagnetic radiation transmission scenario with array elements located near a planar tissue model. The radiated field from the n -th source impinges on the tissue surface at an angle of incidence ζ_n^i and contributes to the total transmitted field.

Consider the scenario in Fig. 2.2, where the transmitter array is a short distance away from a planar tissue surface. We assume all electromagnetic fields involved are time-harmonic and can therefore be represented in phasor form. For the n -th source, let ζ_n^i be the AoI of the incident wavefront and $\mathcal{E}_n^i(\mathbf{p})$ be the complex magnitude of the incident electric field at point \mathbf{p} . The transmitted electric field

amplitudes can be expressed in terms of the incident field amplitudes and transmission coefficients τ_n as

$$\mathcal{E}_n^t(\mathbf{p}) = \tau_n \mathcal{E}_n^i(\mathbf{p}), \quad (2.25)$$

where the superscript t denotes the transmitted portion of the electric field. The total transmitted field can then be found as the sum of the individual fields as $\mathcal{E}^t(\mathbf{p}) = \sum_{n=0}^{N-1} \tau_n \mathcal{E}_n^i(\mathbf{p})$. Transmission coefficients are dependent on the field polarization, the shape of the incident waves, and the geometry of plane of incidence. Here, we assume that the incident waves and surface of incidence are planar. In this case, the transmission coefficients for TE and TM polarization are given as in (2.9).

Surface SAR Model: Since SAR is proportional to $|\mathcal{E}^t|^2$ and incident PD is proportional to $|\mathcal{E}^i|^2$, the surface SAR matrix is defined in terms of the PD model as

$$\mathbf{R}_{\text{SAR}_0}(\mathbf{p}) \triangleq \frac{\eta_0 \sigma}{\rho} \mathbf{T}^H \mathbf{R}_{\text{PD}}(\mathbf{p}) \mathbf{T}, \quad (2.10 \text{ revisited})$$

where \mathbf{T} is a diagonal matrix with the transmission coefficients $\tau_0, \tau_1, \dots, \tau_{N-1}$ in its diagonal. This SAR matrix can then be used to predict surface SAR at a point \mathbf{p} as $\mathbf{x}^H \mathbf{R}_{\text{SAR}_0}(\mathbf{p}) \mathbf{x}$. Furthermore, the exponential decay model in (2.24) indicates that reducing average SAR measurements in millimeter wave systems can be simplified to reducing surface SAR measurements. Note that \mathbf{R}_{PD} is calculated with the proposed PD model as in (2.7), so the proposed surface SAR model is valid even when (A1) and (A2) do not apply. It can be seen that the SAR matrix is also characterized by an effective array steering vector, given as

$$\hat{\mathbf{a}}_{\text{SAR}_0}(\mathbf{p}) = \sqrt{\frac{\eta_0 \sigma}{\rho}} \mathbf{T}^H \hat{\mathbf{a}}_{\text{PD}}(\mathbf{p}), \quad (2.26)$$

and surface SAR can be modeled as

$$\text{SAR}_0(\mathbf{p}, \mathbf{x}) = \frac{|\hat{\mathbf{a}}_{\text{SAR}_0}^H(\mathbf{p}) \mathbf{x}|^2}{\|\mathbf{p}\|^2}. \quad (2.27)$$

In this case, the rotation of the steering vector is dependent on \mathbf{p} through \mathbf{T} .

2.3 Model Verification Results

In this section, we validate the proposed formulas for exposure matrices in (2.7) and (2.10) by simulating a simple millimeter wave exposure scenario in ANSYS High Frequency Structure Simulator (HFSS) software. The following examples demonstrate that the quadratic signal-level models can predict exposure values from software simulations with high accuracy, even in non-ideal settings.

2.3.1 Dipole Array Parameters and Head Model

We consider N element uniform linear arrays (ULAs) of half-wavelength dipoles placed on the x -axis transmitting at 28 GHz. In all simulations, the inter-element spacing of the array is $\lambda/2$ and the system transmit power P is 10 mW. Simulations were performed with both ideal and non-ideal dipoles. The use of ideal dipoles indicates that the antennas were implemented as cylindrical sources with the theoretical radiation pattern of a linear antenna in both the near-field and the far-field. Note that simulations with ideal dipoles fall under (A1) and (A2). Non-ideal dipoles were also modeled in HFSS in order to validate the proposed models in the presence of mutual coupling and near-field effects.

The parameters for the ideal and non-ideal dipoles are shown in Table 2.2. At the operating frequency of 28 GHz, the ideal and non-ideal dipoles achieved a maximum gain of 1.64 and 1.76, respectively, in the xy -plane. For simplicity, all exposure testing points in the validation results are assumed to lie in the xy -plane. The coupling

matrices were calculated with the array Z-parameters as described in [52]. This resulted in the normalized coupling matrices $\mathbf{M}^{(2)}$ and $\mathbf{M}^{(4)}$ given as

$$\mathbf{M}^{(2)} = \begin{bmatrix} 0.69 + j0.03 & 0.07 + j0.13 \\ 0.07 + j0.13 & 0.69 + j0.03 \end{bmatrix},$$

$$\mathbf{M}^{(4)} = \begin{bmatrix} 0.48 + j0.03 & 0.06 + j0.08 & -0.03 - j0.03 & 0.02 + j0.02 \\ 0.06 + j0.08 & 0.47 + j0.04 & 0.05 + j0.08 & -0.03 - j0.03 \\ -0.03 - j0.03 & 0.06 + j0.08 & 0.47 + j0.04 & 0.05 + j0.08 \\ 0.02 + j0.02 & -0.03 - j0.03 & 0.05 + j0.08 & 0.48 + j0.03 \end{bmatrix}, \quad (2.28)$$

for a two-element and four-element ULA, respectively. The NFGCFs were obtained by comparing the predicted and actual array gain at a point 5 mm away from the transmitter at boresight, giving the factors $\alpha^{(2)} = 1.43$ and $\alpha^{(4)} = 2.91$ for arrays of two and four elements, respectively.

Table 2.2.
Dipole antenna parameter specifications.

Parameter	Specifications	
	Ideal Dipole	Non-ideal Dipole
Total Length (mm)	5.353	5.065
Radius (mm)	0.01	0.01
Source Length (mm)	N/A	0.05
Source Impedance (Ω)	N/A	71.18

For SAR simulations, we consider a hemispherical head model with a 20 mm radius centered on the y -axis at a point 5 mm away from the origin, as seen in Fig. 2.3. The head tissue is assumed to be homogeneous with complex dielectric constant $\epsilon^* = 19 - j19.26$ approximately based on Gandhi's model in [21] at a frequency of 28

GHz, giving a tissue conductivity of $\sigma = 30$ S/m. The tissue density is assumed to be 1 g/cm³. SAR values in HFSS were obtained at a depth of 0.2 mm.

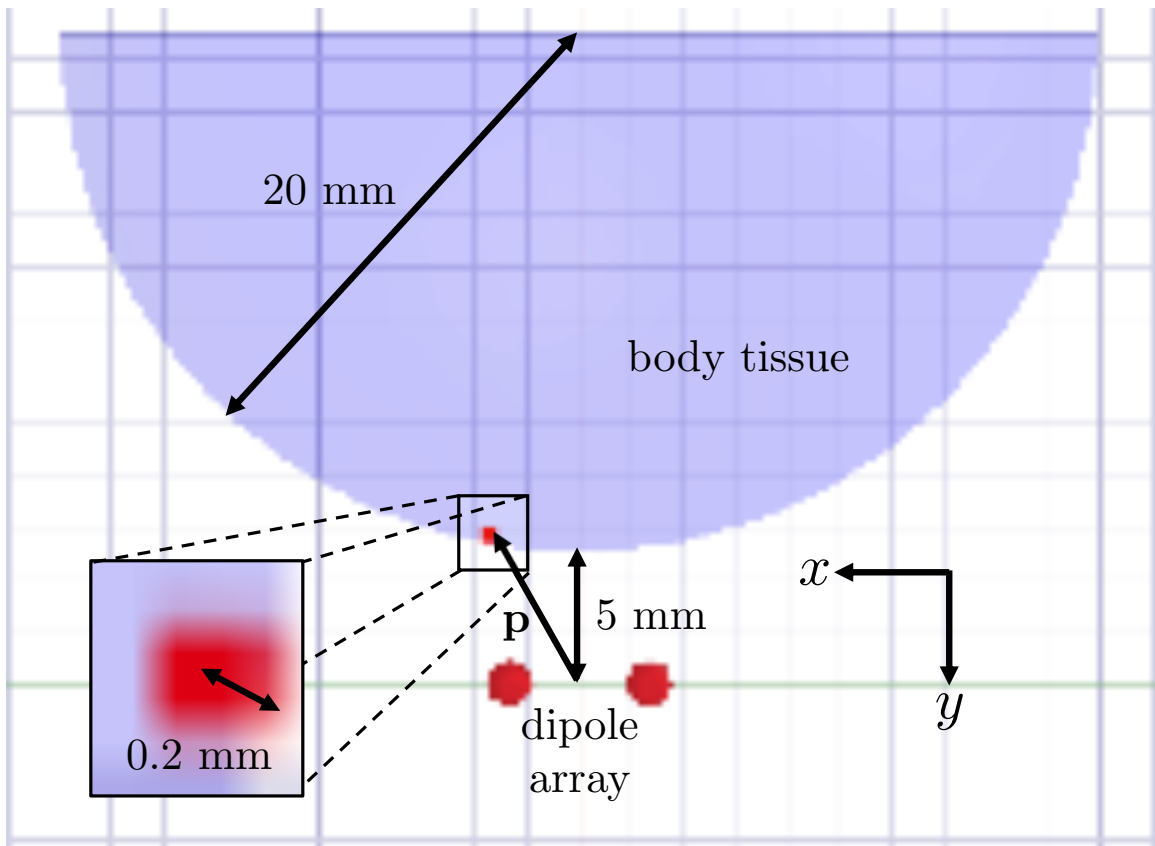


Fig. 2.3. HFSS setup for SAR simulations. The dipole array is placed 5 mm away from a hemispherical tissue model with radius 20 mm, complex dielectric constant $\epsilon^* = 19 - j19.26$, and tissue density 1 g/cm³. SAR values are obtained at a depth of 0.2 mm from the surface point \mathbf{p} .

Since the SAR simulation results were obtained below the tissue surface, we scale the proposed SAR model and SPW model by a constant β to properly account for absorption losses. To determine β , we simulated a plane wave traveling in the $-y$ direction and measured pointwise SAR on the y -axis at a depth of 0.2 mm below the tissue surface. This SAR reading was compared to the predicted surface SAR value obtained from (2.22) to compute β . For the head model with parameters as

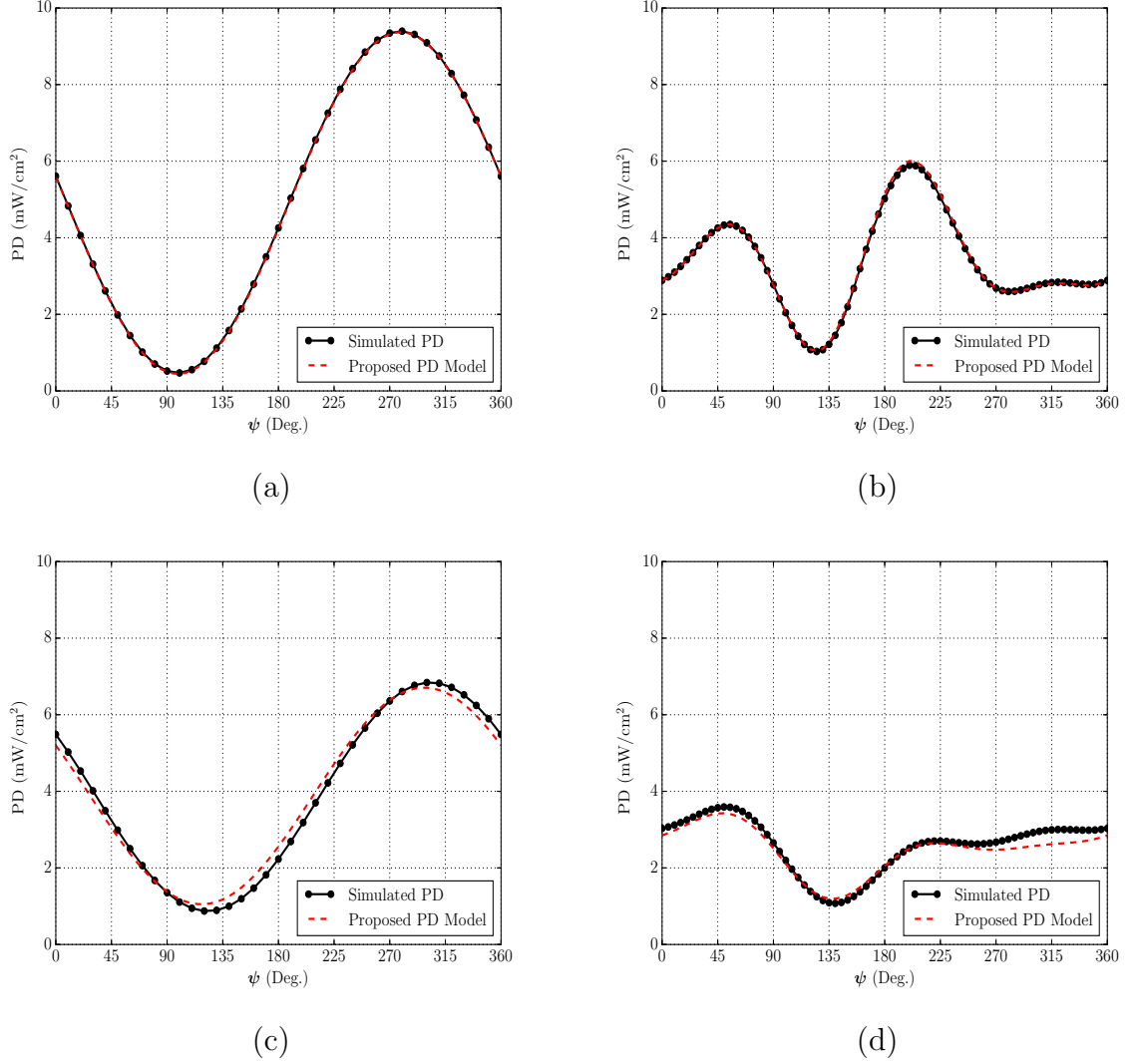


Fig. 2.4. Plane wave equivalent PD values from HFSS simulations and the quadratic model $\mathbf{x}^H \mathbf{R}_{\text{PD}}(\mathbf{p}) \mathbf{x}$, with PD matrices calculated as in (2.7), vs. the beam sweep angle ψ of the transmit signal \mathbf{x} in (2.29). The point \mathbf{p} is located 5 mm from the array center and at 30° from boresight. Results with half-wave dipole ULAs are shown in the ideal case with (a) $N = 2$ and (b) $N = 4$, and in the non-ideal case with $N = 2$ and $N = 4$ in (c) and (d), respectively. The dipole antenna parameters are given in Table 2.2, and the array coupling matrices are given in (2.28).

discussed above, this procedure resulted in a scaling coefficient $\beta = 0.7024$. The same scaling coefficient was used for all SAR scenarios.

2.3.2 Incident PD Model Validation

In the first example, we compare incident PD values obtained from simulations to the quadratic PD model. A beam sweep is performed by setting the transmit signal as

$$\mathbf{x} = \frac{1}{\sqrt{N}} \left[1 \ e^{j\psi} \ e^{j2\psi} \ \dots \ e^{j(N-1)\psi} \right]^T, \quad (2.29)$$

and varying ψ . Plane wave equivalent PD values were obtained from HFSS at a point \mathbf{p} located 5 mm from the center of the array at 30° from boresight. These results were compared to the PD model $\mathbf{x}^H \mathbf{R}_{\text{PD}} \mathbf{x}$ for various values of ψ . The PD matrices were calculated in terms of the simulation parameters and the point \mathbf{p} using (2.7). For example, the matrix for a two-element ULA with ideal dipoles was computed as

$$\mathbf{R}_{\text{PD}}^{(2)} = \begin{bmatrix} 2.87 & 0.68 + j4.41 \\ 0.68 - j4.41 & 6.95 \end{bmatrix}. \quad (2.30)$$

Fig. 2.4 (a) and (b) demonstrate a high agreement between the proposed PD model and the simulation results in the ideal case. The model yields a sinusoidal curve in the case $N = 2$, and the variation of PD behaves as a sum of sinusoids for $N = 4$. The PD model also demonstrates high accuracy in estimating the simulated exposure values in a non-ideal scenario as seen in Fig. 2.4 (c) and (d). As expected, the correction factors impose an amplitude scaling and phase translation on the sinusoid model obtained for $N = 2$.

2.3.3 Surface SAR Model Validation

In the second example, we consider the surface point $\mathbf{p} = [3.47 \ -5.30 \ 0]^T$ mm on the head model in Fig. 2.3. Fig. 2.5 shows the comparison between simulated measurements from HFSS and both the SPW SAR model and the proposed SAR

model $\mathbf{x}^H \mathbf{R}_{\text{SAR}}(\mathbf{p}) \mathbf{x}$ with $\mathbf{R}_{\text{SAR}}(\mathbf{p})$ found as in (2.10). For example, the scaled SAR matrix $\beta \mathbf{R}_{\text{SAR}}(\mathbf{p})$ for a two-element ULA with ideal dipoles was determined to be

$$\mathbf{R}_{\text{SAR}}^{(2)} = \begin{bmatrix} 5.20 & -0.20 + j13.49 \\ -0.20 - j13.49 & 35.04 \end{bmatrix}. \quad (2.31)$$

In the non-ideal case, we found an error between the amplitude of the proposed model and the simulated SAR even when taking the absorption coefficient into consideration. These discrepancies could be caused by a variety of unaccounted factors, such as coupling between the antennas and the head model, the curvature of the head model, and the depth at which SAR is simulated. To address this issue, the predicted SAR values were scaled by a constant K , which was chosen to minimize the error between the proposed model and the simulated values. We note that this scaling constant was only used in the case of the non-ideal dipoles.

The results demonstrate that the proposed model can predict the simulated SAR values with high accuracy. More importantly, the shape of the curves produced by the proposed model closely match that of the simulation results, especially compared to the SPW model curves. This suggests that the model can predict which transmit signals result in relatively high and low exposure values. Therefore, the model can still be applied to design transmission schemes which minimize exposure levels even if K cannot be determined accurately. In addition, any amplitude offset between the proposed model and actual SAR measurements can be lumped into the effective transmit power of the device and controlled through power control settings.

2.4 Exposure Model Analysis and Applications

Given a wireless device and a model for the exposed body, the proposed models for incident PD and surface SAR enable systems to estimate pointwise exposure over regions in space. Let \mathcal{P} be a set of testing points or a region over which exposure

is regulated, such as a superficial area on a head model or a region surrounding the transmitter array. Then an exposure constraint over \mathcal{P} can be expressed as

$$\text{EXP}(\mathbf{p}, \mathbf{x}) \leq Q, \forall \mathbf{p} \in \mathcal{P}, \quad (2.32)$$

where Q is the regulatory exposure threshold. However, if \mathcal{P} is defined as a contiguous area or volume, it is unfeasible to directly incorporate this constraint into signal design algorithms to mitigate electromagnetic absorption. In this section, we present methods for sampling \mathcal{P} in order to characterize exposure over the entire testing region within a certain error threshold with a finite number of points. We then leverage this sampled representation to obtain a method for calculating exposure matrices for predicting average exposure, rather than pointwise exposure.

2.4.1 Sampling Methods

Let \mathbf{p} and $\tilde{\mathbf{p}}$ be two points in the region \mathcal{P} . We first examine the relationship between the maximum difference in exposure levels at these points, given as

$$d_{\text{EXP}}(\mathbf{p}, \tilde{\mathbf{p}}) = \max_{\mathbf{x}: \|\mathbf{x}\|=1} |\text{EXP}(\mathbf{p}, \mathbf{x}) - \text{EXP}(\tilde{\mathbf{p}}, \mathbf{x})|, \quad (2.33)$$

and inter-point distance $\|\mathbf{p} - \tilde{\mathbf{p}}\|$.

Note that the highest levels of exposure occur at points which are closest to the array and which lie in the direction of the highest array gain. These characteristics can be captured by the minimum distance to the array over \mathcal{P} , denoted as r_{\min} , and the maximum directivity over \mathcal{P} among the antennas, denoted as G_{\max} . The minimum distance r_{\min} is defined as the smallest distance from a point in \mathcal{P} to any antenna element and is given as

$$r_{\min} = \min_{\mathbf{p} \in \mathcal{P}} r_{\min}(\mathbf{p}), \quad (2.34)$$

where $r_{\min}(\mathbf{p})$ is smallest distance to \mathbf{p} over the array elements,

$$r_{\min}(\mathbf{p}) = \min_{n=0,1,\dots,N-1} \|\mathbf{p}_n\|. \quad (2.35)$$

Likewise, the maximum directivity G_{\max} can be defined in terms of the individual gain pattern as

$$G_{\max} = \max_{n=0,1,\dots,N-1} \max_{\mathbf{p} \in \mathcal{P}} g_n(\mathbf{p}_n). \quad (2.36)$$

These parameters correspond to a worst-case scenario in terms of exposure, and are therefore useful in bounding the maximum exposure differential.

We now state the following lemma as a preliminary step in characterizing an upper bound on $d_{\text{EXP}}(\mathbf{p}, \tilde{\mathbf{p}})$.

Lemma 2.4.1 *Let \mathbf{p} and $\tilde{\mathbf{p}}$ be distinct points in a set \mathcal{P} not containing the origin. Assume that $g_n(\mathbf{p}_n)$ is constant over \mathcal{P} . Then we have that for any non-zero transmit signal \mathbf{x} ,*

$$\left| \frac{|\mathbf{a}^H(\mathbf{p})\mathbf{x}|^2}{\|\mathbf{p}\|^2} - \frac{|\mathbf{a}^H(\tilde{\mathbf{p}})\mathbf{x}|^2}{\|\tilde{\mathbf{p}}\|^2} \right| < \varepsilon \quad (2.37)$$

as long as $\|\mathbf{p} - \tilde{\mathbf{p}}\| < \Delta/\|\mathbf{x}\|^2$, where Δ is given as

$$\Delta = \frac{\varepsilon r_{\min}^2}{2N^2 G_{\max}} \left(\frac{4\pi}{\lambda} + \frac{1}{r_{\min}} \right)^{-1}. \quad (2.38)$$

The proof can be found in Appendix A.

Although Lemma 2.4.1 only bounds the difference in a quantity closely related to PD, the structure of the exposure models allow this result to be applied to both the PD and SAR models. As demonstrated in Section 2.2, both PD and surface SAR matrices can be characterized by an steering vector, and exposure at \mathbf{p} can be modeled as a rank-one quadratic as in (2.19). The effective steering vector $\hat{\mathbf{a}}_{\text{EXP}}(\mathbf{p})$ can be expressed as a spatially dependent linear transformation on $\mathbf{a}(\mathbf{p})$ of the form

$$\hat{\mathbf{a}}_{\text{EXP}}(\mathbf{p}) = k_{\text{EXP}} \mathbf{D}(\mathbf{p}) \mathbf{W} \mathbf{a}(\mathbf{p}), \quad (2.39)$$

where k_{EXP} is a constant of proportionality dependent on the exposure measure, $\mathbf{D}(\mathbf{p})$ is an $N \times N$ diagonal matrix defined as a function of \mathbf{p} , and \mathbf{W} is an $N \times N$ matrix. For example, the PD effective steering vector $\hat{\mathbf{a}}_{\text{PD}}(\mathbf{p})$ can be obtained by setting $k_{\text{PD}} = \sqrt{P/4\pi}$, $\mathbf{D} = \alpha(\|\mathbf{p}\|)\mathbf{I}$ and $\mathbf{W} = \mathbf{M}^H$. For simplicity we assume that the

region of interest is small enough so that $\mathbf{D}(\mathbf{p})$ can be approximated by a constant matrix \mathbf{D} over \mathcal{P} and $g_n(\mathbf{p}_n)$ is approximately constant.

The linear transformation in (2.39) and Lemma 2.4.1 can then be applied to show the following result.

Lemma 2.4.2 *Let \mathbf{p} and $\tilde{\mathbf{p}}$ be distinct points in a set \mathcal{P} not containing the origin. Assume $g_n(\mathbf{p}_n)$ is approximately constant over \mathcal{P} and that \mathbf{W} is full rank. Then*

$$d_{\text{EXP}}(\mathbf{p}, \tilde{\mathbf{p}}) < \varepsilon \quad (2.40)$$

as long as

$$\|\mathbf{p} - \tilde{\mathbf{p}}\| < \Delta_{\text{EXP}} \triangleq \frac{\Delta}{k_{\text{EXP}}^2 \|\mathbf{W}\mathbf{D}\|_2^2}, \quad (2.41)$$

where Δ is given as in Lemma 2.4.1.

Proof By substituting (2.19) into the definition of $d_{\text{EXP}}(\mathbf{p}, \tilde{\mathbf{p}})$, we have that

$$d_{\text{EXP}}(\mathbf{p}, \tilde{\mathbf{p}}) = \max_{\mathbf{x}: \|\mathbf{x}\|=1} \left| \frac{|\hat{\mathbf{a}}_{\text{EXP}}^H(\mathbf{p})\mathbf{x}|^2}{\|\mathbf{p}\|^2} - \frac{|\hat{\mathbf{a}}_{\text{EXP}}^H(\tilde{\mathbf{p}})\mathbf{x}|^2}{\|\tilde{\mathbf{p}}\|^2} \right|. \quad (2.42)$$

Since effective steering vectors in (2.42) are linear transformations of $\mathbf{a}(\mathbf{p})$, $d_{\text{EXP}}(\mathbf{p}, \tilde{\mathbf{p}})$ can be expressed as

$$d_{\text{EXP}}(\mathbf{p}, \tilde{\mathbf{p}}) = \max_{\mathbf{x}: \|\mathbf{x}\|=1} \left| \frac{|\mathbf{a}^H(\mathbf{p})\hat{\mathbf{x}}|^2}{\|\mathbf{p}\|^2} - \frac{|\mathbf{a}^H(\tilde{\mathbf{p}})\hat{\mathbf{x}}|^2}{\|\tilde{\mathbf{p}}\|^2} \right|, \quad (2.43)$$

where $\hat{\mathbf{x}}$ is the effective transmit signal given as

$$\hat{\mathbf{x}} = k_{\text{EXP}} \mathbf{W}^H \mathbf{D}^H \mathbf{x}. \quad (2.44)$$

Applying Lemma 2.4.1 with the effective transmit signal $\hat{\mathbf{x}}$, we have that if

$$\|\mathbf{p} - \tilde{\mathbf{p}}\| < \frac{\Delta}{\max_{\mathbf{x}: \|\mathbf{x}\|=1} \|\hat{\mathbf{x}}\|^2} = \frac{\Delta}{k_{\text{EXP}}^2 \|\mathbf{D}\mathbf{W}\|_2^2}, \quad (2.45)$$

then $d_{\text{EXP}}(\mathbf{p}, \tilde{\mathbf{p}}) < \varepsilon$ as desired. ■

The previous results not only imply that the maximum exposure differential $d_{\text{EXP}}(\mathbf{p}, \tilde{\mathbf{p}})$ can be guaranteed to lie below the error threshold ε if the two testing points are sufficiently close, but also give an explicit expression for the maximum allowable distance between the two points. The assumption that \mathbf{W} is full rank, which is equivalent to \mathbf{M} having full rank, corresponds with the notion that non-zero transmit signals cannot induce an electric field of zero over \mathcal{P} and is thus reasonable in the context of this study. These bounds are now applied to formulate uniform and non-uniform sampling methods which allow us to characterize pointwise exposure over \mathcal{P} in terms of a finite number of points at the cost of a predetermined margin of error.

Uniform Sampling: A direct application of Lemma 2.4.2 yields a method for uniformly sampling the region \mathcal{P} . Let ε be the desired maximum exposure variation between adjacent points. Then sampling points in \mathcal{P} at a maximum distance of Δ_{EXP} guarantees that the exposure differential between two adjacent points is at most ε . Note that this criteria only gives a guideline for the allowable distance between sample points, since the specific manner of sampling should be determined based on the body tissue geometry. However, we provide a numerical example in Section 2.4.3 to demonstrate how to sample a relatively simple region.

Non-uniform Sampling: A shortcoming of the uniform sampling method is that it does not leverage the decay of electromagnetic field strengths with distance from sources. Intuitively, exposure values should follow a downward trend as points move farther from the transmitter and thus the distance between sampled points should be allowed to increase without penalty. This dependence can be seen in the term Δ_{EXP} , which increases with r_{\min}^3 . Additionally, other model parameters which are dependent on location, such as the transmission coefficients and the NFGCF, also affect the sampling distance. The uniform sampling approach restricts Δ_{EXP} to a constant value based on the point closest to the array, but a non-uniform method can be developed by adaptively adjusting the sampling distance.

The main idea of the non-uniform sampling algorithm is to sample the closest points to the array first and move outwards while adaptively adjusting the sampling

distance. Given a spatial region \mathcal{P} , we first sample the closest point to the transmitter array, given as

$$\mathbf{p}_0 = \underset{\mathbf{p} \in \mathcal{P}}{\operatorname{argmin}} r_{\min}(\mathbf{p}). \quad (2.46)$$

Based on Lemmas 2.4.1 and 2.4.2, a positionally dependent sampling distance can be defined as

$$\begin{aligned} \Delta_{\text{EXP}}(\mathbf{p}) \triangleq & \frac{\varepsilon r_{\min}^2(\mathbf{p})}{2N^2 G_{\max} k_{\text{EXP}}^2 \|\mathbf{W}\mathbf{D}(\mathbf{p})\|_2^2} \\ & \times \left(\frac{4\pi}{\lambda} + \frac{1}{r_{\min}(\mathbf{p})} \right)^{-1}. \end{aligned} \quad (2.47)$$

According to the uniform sampling criteria, the next sample points should be located at a distance of $\Delta_{\text{EXP}}(\mathbf{p}_0)$ from \mathbf{p}_0 . Let \mathbf{p}_1 be one of those points, and let $\Delta_{\text{EXP}}(\mathbf{p}_1)$ be the sampling distance corresponding to \mathbf{p}_1 . Since exposure at points closer to the array than \mathbf{p}_1 is characterized by the sample at \mathbf{p}_0 , the remaining sample points will be located farther from the array than \mathbf{p}_1 . Therefore, the next sample point, \mathbf{p}_2 , is chosen to lie at a maximum distance of $\Delta_{\text{EXP}}(\mathbf{p}_1)$ from \mathbf{p}_1 , as doing so ensures that the conditions of Lemma 2.4.2 are still satisfied and the exposure differential between \mathbf{p}_1 and \mathbf{p}_2 is bounded as $d_{\text{EXP}}(\mathbf{p}_1, \mathbf{p}_2) < \varepsilon$. This procedure is repeated until the entire region is sampled.

2.4.2 Spatially Averaged Exposure Model

As previously mentioned, regulation agencies measure spatially averaged exposure rather than pointwise exposure in order to determine whether wireless devices comply with exposure thresholds. The sampling methods developed in the previous section allow us to characterize modeled exposure over a region \mathcal{P} with a finite number of points. We now show how this representation can be used to estimate spatially averaged exposure over \mathcal{P} , given as

$$\text{EXP}_{\text{avg}}(\mathcal{P}) = \frac{\int_{\mathcal{P}} \text{EXP}(\mathbf{p}, \mathbf{x}) d\mathbf{p}}{|\mathcal{P}|}, \quad (2.48)$$

where $|\mathcal{P}|$ is the area or volume of \mathcal{P} , with a quadratic model $\mathbf{x}^H \mathbf{R}_{\text{avg}}(\mathcal{P}) \mathbf{x}$. For simplicity, we shortly drop the dependence of the exposure function on the transmit signal \mathbf{x} .

Let \mathcal{P} be the region over which measurements are averaged and let

$$\mathcal{P}_s = \left\{ \mathbf{p}^{(0)}, \mathbf{p}^{(1)}, \dots, \mathbf{p}^{(M-1)} \right\} \quad (2.49)$$

be the M sample points obtained by applying either of the proposed sampling methods on \mathcal{P} . The region \mathcal{P} can be divided into subregions corresponding to each sample point as

$$\mathcal{P}^{(m)} = \left\{ \mathbf{p} \in \mathcal{P} : \mathbf{p}^{(m)} = \underset{\tilde{\mathbf{p}} \in \mathcal{P}_s}{\operatorname{argmin}} \|\mathbf{p} - \tilde{\mathbf{p}}\| \right\}. \quad (2.50)$$

The m -th subregion consists of the points in \mathcal{P} lying closest to the m -th sample point, and these subregions define a partition of \mathcal{P} . Therefore, average exposure over \mathcal{P} can be written as

$$\operatorname{EXP}_{\text{avg}}(\mathcal{P}) = \frac{\sum_{m=0}^{M-1} \int_{\mathcal{P}^{(m)}} \operatorname{EXP}(\mathbf{p}) d\mathbf{p}}{|\mathcal{P}|}. \quad (2.51)$$

Assuming there are no discontinuities in the electromagnetic field over \mathcal{P} , the integral Mean Value Theorem gives us that the average exposure over each subregion $\mathcal{P}^{(m)}$ is equal to the exposure value at some point $\tilde{\mathbf{p}}^{(m)}$ in the subregion. This relationship can be formally stated as

$$\operatorname{EXP}(\tilde{\mathbf{p}}^{(m)}) = \frac{\int_{\mathcal{P}^{(m)}} \operatorname{EXP}(\mathbf{p}) d\mathbf{p}}{|\mathcal{P}^{(m)}|}. \quad (2.52)$$

Note that the point $\tilde{\mathbf{p}}^{(m)}$ belongs to the m -th sample point's subregion. Moreover, the distance between \mathbf{p}_m and $\tilde{\mathbf{p}}_m$ must be less than the distance between \mathbf{p}_m and its neighboring sample points. Thus, Lemma 2.4.2 ensures that

$$d_{\operatorname{EXP}}(\mathbf{p}_m, \tilde{\mathbf{p}}_m) < \varepsilon. \quad (2.53)$$

Combining the expressions (2.51) and (2.52) with the bound in (2.53), we have that average exposure over the entire region can be approximated as

$$\operatorname{EXP}_{\text{avg}}(\mathcal{P}) \approx \frac{\sum_{m=0}^{M-1} |\mathcal{P}^{(m)}| \operatorname{EXP}(\mathbf{p}^{(m)})}{|\mathcal{P}|}. \quad (2.54)$$

If \mathcal{P} is sampled such that each subregion is of the same size, average exposure can be approximated as the arithmetic mean of the sample points as

$$\text{EXP}_{\text{avg}}(\mathcal{P}) \approx \text{EXP}_{\text{avg}}(\mathcal{P}_s) \triangleq \frac{1}{M} \sum_{m=0}^{M-1} \text{EXP}(\mathbf{p}^{(m)}). \quad (2.55)$$

In this case, the maximum error between the approximation in (2.55) and the true averaged exposure, given as

$$d_{\text{EXP}}(\mathcal{P}, \mathcal{P}_s) = \max_{\mathbf{x}: \|\mathbf{x}\|=1} \left| \text{EXP}_{\text{avg}}(\mathcal{P}) - \text{EXP}_{\text{avg}}(\mathcal{P}_s) \right|, \quad (2.56)$$

will also be bounded by ε . The approximation for average exposure given in (2.55) can also be written in terms of the signal-level model as

$$\text{EXP}_{\text{avg}}(\mathcal{P}_s, \mathbf{x}) = \frac{1}{M} \sum_{m=0}^{M-1} \mathbf{x}^H \mathbf{R}_{\text{EXP}}(\mathbf{p}^{(m)}) \mathbf{x} \quad (2.57)$$

$$= \mathbf{x}^H \left(\frac{1}{M} \sum_{m=0}^{M-1} \mathbf{R}_{\text{EXP}}(\mathbf{p}^{(m)}) \right) \mathbf{x} \quad (2.58)$$

$$\triangleq \mathbf{x}^H \mathbf{R}_{\text{EXP, avg}}(\mathcal{P}) \mathbf{x}, \quad (2.59)$$

where the matrix $\mathbf{R}_{\text{EXP, avg}}(\mathcal{P})$ now characterizes average exposure over \mathcal{P} . In general, the average exposure matrix can be written as a weighted average of the exposure matrices for each sample point as

$$\mathbf{R}_{\text{EXP, avg}}(\mathcal{P}) = \frac{1}{|\mathcal{P}|} \sum_{m=0}^{M-1} |\mathcal{P}^{(m)}| \mathbf{R}_{\text{EXP}}(\mathbf{p}^{(m)}). \quad (2.60)$$

In practice, average exposure matrices $\mathbf{R}_0, \mathbf{R}_1, \dots, \mathbf{R}_{L-1}$ corresponding to L different body regions and/or gestures can be calculated offline to model exposure over a variety of operating conditions. A worst-case constraint on the system can then be defined as

$$\max_{\ell=0,1,\dots,L-1} \mathbf{x}^H \mathbf{R}_\ell \mathbf{x} \leq Q. \quad (2.61)$$

This constraint is identical to those examined in [36,37,42–46], therefore the signaling schemes developed in these studies can be applied to jointly maximize the far-field rate performance while controlling near-field exposure.

2.4.3 Numerical Examples of Sampling Methods

We present a numerical example to demonstrate the application of the proposed sampling guidelines. We consider a scenario similar to that in Fig. 2.3, but with a spherical head model with a radius of 90 mm at a distance d away from a transmitter equipped with N ideal half-wave dipoles operating at a frequency of 28 GHz. We assume an incident power density constraint is placed on the surface of the head model in the xy -plane, where maximum exposure occurs.

The surface of the head model was sampled for $N = 2$ and $d = 10$ mm according to the uniform and non-uniform sampling guidelines as seen in Fig. 2.6. For illustrative purposes, the transmit power was set to $P = 10$ mW and the variation threshold ε was set to 25 mW/cm². The sampled area corresponds to an arc of length 94.25 mm centered at boresight from the center of the transmitter. Note that although the uniform sampling forces points to be located in close proximity, the non-uniform approach allows sparser sampling at points relatively far from the transmitter. It takes 51 points to uniformly sample the region, whereas the region can be sampled with only 17 points using the non-uniform method.

Table 2.3.
Number of sample points for different choices of N and d .

Parameters	# Sampling Points	
	Uniform	Non-uniform
$d = 10$ mm, $N = 2$	1251	343
$d = 10$ mm, $N = 4$	5003	1359
$d = 5$ mm, $N = 2$	5357	787
$d = 5$ mm, $N = 4$	21425	3133

The number of sample points required to sample the region from the previous example with a variation threshold of $\varepsilon = 1$ mW/cm² for various combinations of values

for N and d are shown in Tables 2.3. In all cases, non-uniform sampling requires a significantly smaller number of points than the uniform method but the sampling distance must be recalculated at each iteration, increasing the computational complexity of this approach. Although the amount of sampling required in all cases seems onerous, this is due to the restrictive bound we have placed on the maximum difference between *pointwise* exposure measurements. For practical applications, the sample points should be used to compute average exposure matrices as discussed in Section 2.4.2.

2.4.4 Average Exposure Model Validation

In order to validate the average exposure model, we consider two arcs, denoted as \mathcal{P}_1 and \mathcal{P}_2 , on the surface of a head model of radius $R = 90$ mm next to a two-element dipole array at distance of $d = 5$ mm from the head, as shown in Fig. 2.7. These regions were sampled uniformly and non-uniformly according to the proposed guidelines. As in Section 2.3, we assume that the transmission frequency is 28 GHz, the transmit power is 10 mW, and all arrays are ULAs with $\lambda/2$ spacing.

In Fig. 2.8, we perform a beam sweep with non-ideal dipoles as in Section 2.3 and compare the simulated average PD from HFSS with the average PD predicted by the model in (2.55). The regions were uniformly sampled with $\epsilon = 10$ mW/cm², resulting in 45 and 29 sample points for \mathcal{P}_1 and \mathcal{P}_2 , respectively. The proposed model approximates the simulated values well even though the value of ϵ is relatively large.

We also studied the convergence of the average exposure matrix in (2.60) as M increases for both uniform and non-uniform samplings of the regions \mathcal{P}_1 and \mathcal{P}_2 . In this case, we consider an ideal two-element half-wave dipole array and compute average PD matrices. For each region \mathcal{P} , the limit as $M \rightarrow \infty$ of the average PD matrices, denoted as $\mathbf{R}(\mathcal{P})$, is taken to be $\mathbf{R}_{\text{EXP,avg}}(\mathcal{P})$ from (2.60) with $\epsilon = 0.1$ mW/cm². In Fig. 2.9, we compare the mean-square-error (MSE) between the average PD matrix $\mathbf{R}_{\text{PD,avg}}(\mathcal{P})$ from (2.60) and $\mathbf{R}(\mathcal{P})$ versus the number of samples used to

compute $\mathbf{R}_{\text{PD, avg}}(\mathcal{P})$. Since the sampling procedures are defined in terms of ϵ rather than the number of samples, there is a range of values of ϵ for which a sampling of \mathcal{P} will result in a fixed M . Therefore, for any given M we take the MSE above to be the average MSE among all ϵ which result in M samples. The plot shows that non-uniform sampling leads to a lower MSE than uniform-sampling in both regions. This is because the non-uniform sampling procedure allocates more samples to the portions of a region which have a larger effect on the average PD matrix than to the portions which are less impactful.

2.5 Conclusion

In this chapter, we examined exposure models for two major measures of electromagnetic absorption at millimeter wave frequencies. We developed expressions to approximate the pointwise exposure matrices for both incident PD and surface SAR and showed that both exposure measures are characterized by an effective steering vector. The proposed models only require a relatively small number of parameters to be computed and can predict exposure over contiguous regions without additional measurements. Software simulations demonstrate that the exposure models can estimate pointwise exposure with high accuracy.

The models were then analyzed in order to provide insights into how to sample them to obtain an accurate representation of exposure over a spatial region. The proposed uniform and non-uniform sampling guidelines indicate what inter-point sampling distance is required to ensure that spatial exposure variations lie beneath a chosen threshold. A numerical example showing the application of the sampling algorithms demonstrates that non-uniform spatial sampling results in significantly fewer sample points. The sampling methods can further be applied to the problem of calculating quadratic models for spatially averaged exposure. Simulation results demonstrate that these models can effectively approximate average exposure. Average exposure matrices can also be directly incorporated into exposure-aware signal design

algorithms in the literature to achieve high data rates while remaining compliant with regulatory exposure standards.

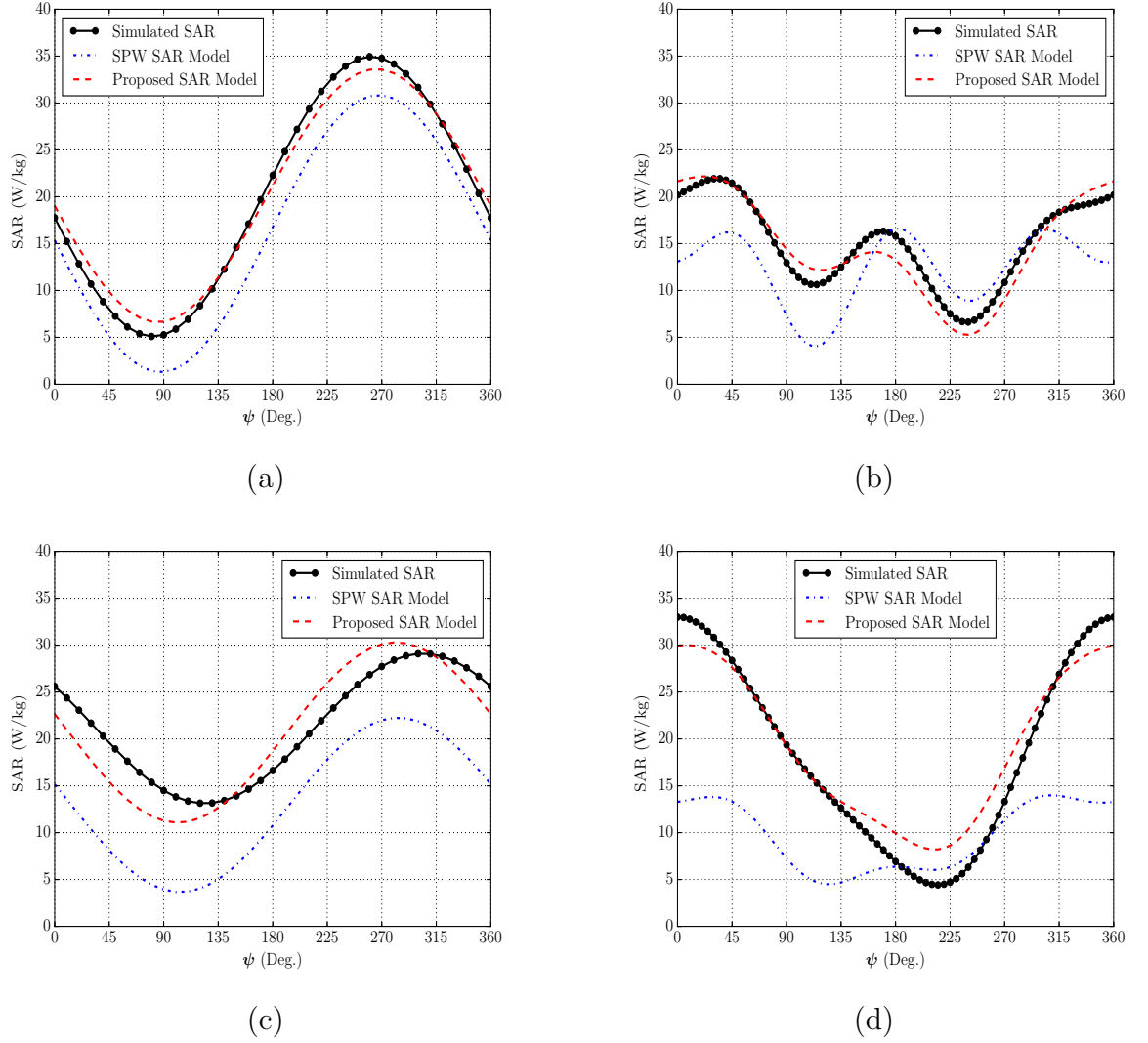
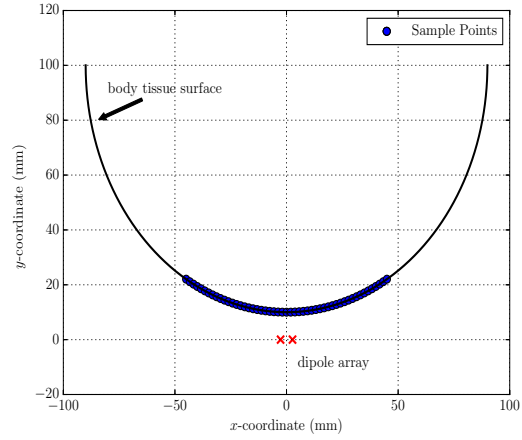
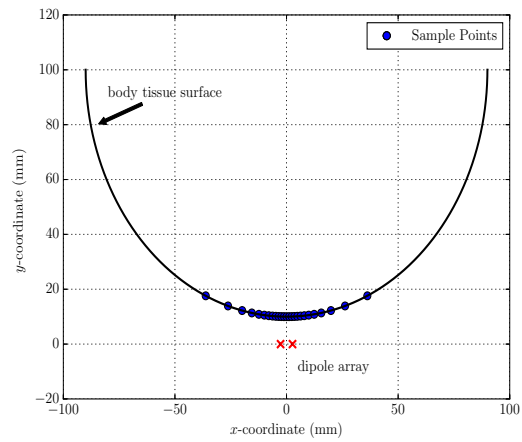


Fig. 2.5. SAR values from HFSS simulations, the SPW SAR model in (2.22), and the quadratic model $\mathbf{x}^H \mathbf{R}_{\text{SAR}}(\mathbf{p}) \mathbf{x}$, with SAR matrices calculated as in (2.10), vs. the beam sweep angle ψ of the transmit signal \mathbf{x} in (2.29). The body model and measurement point are shown in Fig. 2.3. Non-simulated values were scaled by a factor of 0.7024 to account for absorption losses. Results with half-wave dipole ULAs are shown in the ideal case with (a) $N = 2$ and (b) $N = 4$, and in the non-ideal case with $N = 2$ and $N = 4$ in (c) and (d), respectively. The dipole antenna parameters are given in Table 2.2, and the array coupling matrices are given in (2.28). In the non-ideal cases, the proposed model was scaled by a factor of $K = 1.203$ and $K = 1.423$ in (c) and (d), respectively.



(a)



(b)

Fig. 2.6. Plots of the sampling points obtained from the (a) uniform and (b) non-uniform sampling approaches over the surface of a spherical head model with radius 90 mm at a distance of 10 mm from a two-element ideal dipole ULA. Sampling was performed with an error parameter of $\epsilon = 25$ mW/cm².

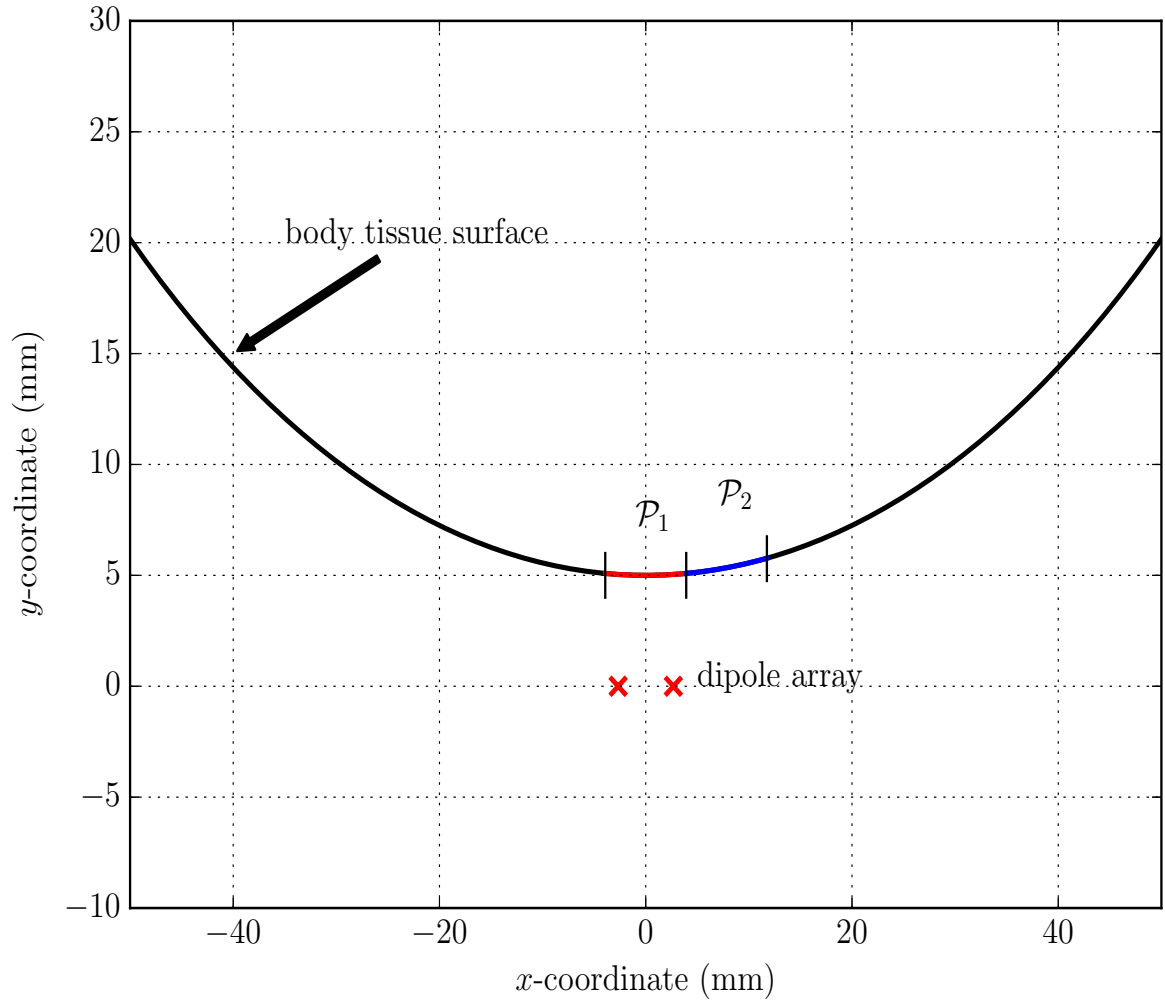


Fig. 2.7. Two regions considered in the validation of the average exposure model. Each region is an arc of measure 5° on the surface of a spherical head model with radius 90 mm at a distance of 5 mm from the center of the array.

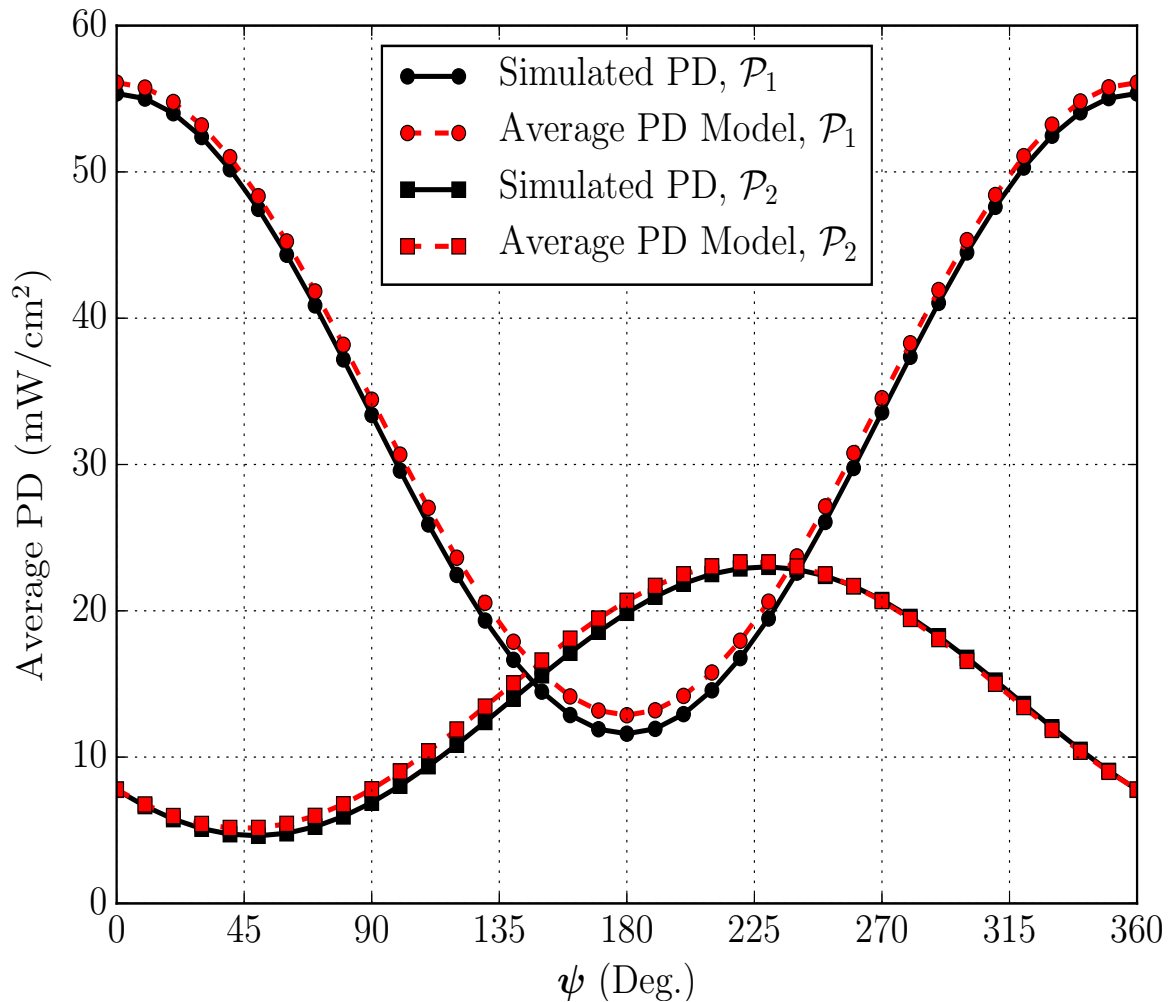


Fig. 2.8. Average PD values obtained from HFSS simulations using (2.48), and the proposed average exposure model in (2.55), vs. the beam sweep angle ψ of the transmit signal \mathbf{x} in (2.29) on the regions \mathcal{P}_1 and \mathcal{P}_2 . Values were obtained for a non-ideal two-element dipole array. For both regions, the proposed model was calculated using a uniform sampling with $\epsilon = 10$ mW/cm².

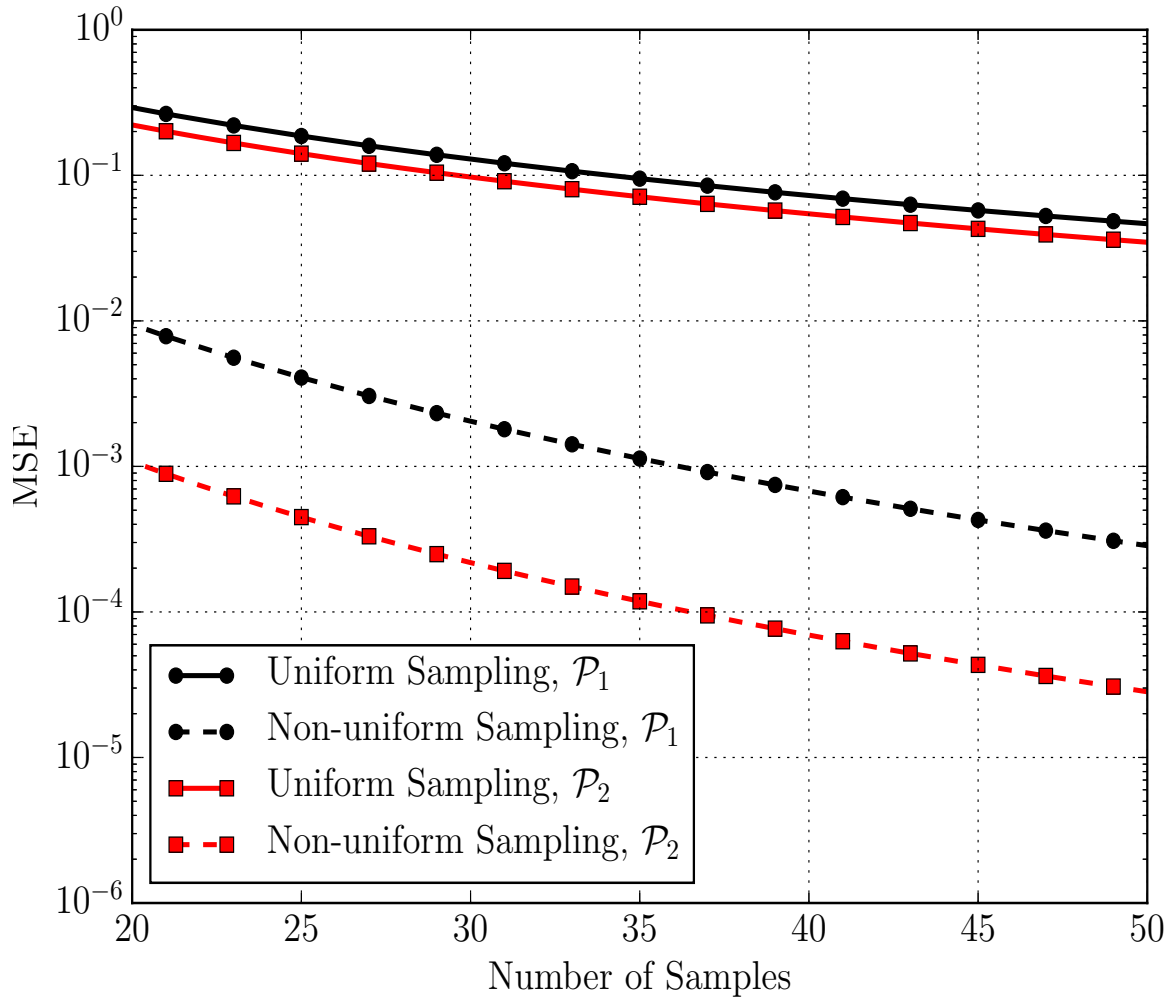


Fig. 2.9. Mean-square-error (MSE) between the average PD matrices $\mathbf{R}_{\text{PD, avg}}(\mathcal{P})$ from (2.60) and $\mathbf{R}(\mathcal{P})$ vs. the number of samples M . Computations were performed for an ideal two-element dipole array.

3. EFFICIENT SIGNAL DESIGN UNDER EXPOSURE CONSTRAINTS

In this chapter, we propose two applications for the exposure models considered in Chapter 2 by introducing constraints directly into the signal design problem. We first consider a scenario in which the number of exposure constraints is large, and propose an approach that reduces the number of exposure constraints by iteratively finding the points with maximum exposure. In the second scenario, we consider a dynamic exposure scenario in which the position of the device relative to the user changes. We propose a position-based adaptive power back-off scheme and develop an efficient implementation by leveraging the structure of DFT codebooks.

3.1 System Model

We consider an uplink narrowband transmission from a wireless device with N_T transmit antennas to a base-station with N_R receive antennas. The received signal $\mathbf{y} \in \mathbb{C}^{N_R}$ can be written as

$$\mathbf{y} = \mathbf{H}\mathbf{x} + \mathbf{n}, \quad (3.1)$$

where $\mathbf{x} \in \mathbb{C}^{N_T}$ is the transmit signal, $\mathbf{H} \in \mathbb{C}^{N_R \times N_T}$ is the channel matrix, and $\mathbf{n} \in \mathbb{C}^{N_R}$ is an additive white Gaussian noise (AWGN) vector with entries distributed as $\mathcal{C}(0, \sigma^2)$. The transmit signal \mathbf{x} is formed from M data streams by precoding a zero-mean, unit-variance symbol vector $\mathbf{s} \in \mathbb{C}^M$ with a precoder $\mathbf{F} \in \mathbb{C}^{N_T \times M}$ as $\mathbf{x} = \mathbf{F}\mathbf{s}$. We assume that the data streams are independent, thus $\mathbb{E}[\mathbf{s}\mathbf{s}^H] = \mathbf{I}$.

We assume the channel follows an extended Saleh-Valenzuela geometric model [56] with L propagation clusters. Here, \mathbf{H} is given as

$$\mathbf{H} = \frac{1}{\sqrt{L}} \sum_{\ell=1}^L \beta_{\ell} \mathbf{a}_R(\boldsymbol{\theta}_{R,\ell}) \mathbf{a}_T^H(\boldsymbol{\theta}_{T,\ell}), \quad (3.2)$$

where $\beta_\ell \sim \mathcal{CN}(0, 1)$ denotes the complex cluster gain, $\mathbf{a}_R(\boldsymbol{\theta}_{R,\ell}) \in \mathbb{C}^{N_R}$ denotes the receive array steering vector corresponding to the angle of arrival (AOA) $\boldsymbol{\theta}_{R,\ell}$, and $\mathbf{a}_T(\boldsymbol{\theta}_{T,\ell}) \in \mathbb{C}^{N_T}$ denotes the transmit array steering vector corresponding to the angle of departure (AOD) $\boldsymbol{\theta}_{T,\ell}$. The transmitter and receiver are assumed to employ uniform linear arrays (ULAs) of antennas with half-wavelength spacing. In this case, the array response vector for an array with N elements is given as

$$\mathbf{a}(\theta) = \left[1 \ e^{j\pi \sin \theta} \ \dots \ e^{j\pi(N-1) \sin \theta} \right]^T. \quad (3.3)$$

The precoder optimization problem under simultaneous transmit power and exposure constraints is given as

$$\begin{aligned} \max_{\mathbf{F} \in \mathcal{F}} \quad & \log \left| \mathbf{I} + \frac{1}{\sigma^2} \mathbf{H} \mathbf{F} \mathbf{F}^H \mathbf{H}^H \right| \\ \text{s.t.} \quad & \text{tr}(\mathbf{F}^H \mathbf{F}) \leq P_T \\ & \text{EXP}(\mathbf{F}, \mathcal{P}) \leq Q, \end{aligned} \quad (3.4)$$

where \mathcal{F} is the precoding feasible set, $\text{EXP}(\mathbf{F}, \mathcal{P})$ is an exposure constraint function defined over the set of testing points \mathcal{P} and Q is the exposure threshold. The models from the previous section yield the approximation $\mathbf{x}^H \mathbf{R}(p) \mathbf{x}$ for exposure at p . Exposure measurements are typically reported as averages over a specified time window. The averaging times are typically on the order of minutes, while the transmit signal can vary on the order of microseconds. Additionally, the maximum exposure measurement must lie below the PD or SAR limit for the device to be compliant. Therefore, we define the exposure constraint function $\text{EXP}(\mathbf{F}, \mathcal{P})$ as a maximum exposure constraint over all of the testing points

$$\text{EXP}(\mathbf{F}, \mathcal{P}) \triangleq \max_{p \in \mathcal{P}} \mathbb{E} \left[\mathbf{x}^H \mathbf{R}(p) \mathbf{x} \right] = \max_{p \in \mathcal{P}} \text{tr} \left(\mathbf{F}^H \mathbf{R}(p) \mathbf{F} \right). \quad (3.5)$$

PD and SAR thresholds are typically specified as averages over contiguous spatial regions rather than single points. PD measurements are averaged over areas of 1 or 20 cm², while SAR measurements are averaged over volumes corresponding to 1 or

10 g [18, 19]. The point exposure model can be extended to find an exposure matrix \mathbf{R}_V corresponding to an averaging volume (or surface) V through the relation

$$\mathbf{R}_V = \frac{1}{|V|} \int_V \mathbf{R}(p) dV. \quad (3.6)$$

The volume exposure matrix inherits its Hermitian and positive semi-definite structure from $\mathbf{R}(p)$, therefore the proposed approaches do not preclude cases where spatial averages are measured.

Even in the case $\mathcal{F} = \mathbb{C}^{N_T \times M}$, i.e., when only the precoder size is constrained, the problem in (3.4) is non-convex. Work in [42] shows that this problem has a strong dual in the case that \mathcal{P} is finite and that an optimal precoder can be obtained through a modified waterfilling algorithm. However, \mathcal{P} may be large or infinite, and millimeter wave systems are often unable to perform fully-digital precoding, therefore it might be impractical or impossible to apply this optimal solution.

3.2 Discretization Method for Optimal Signaling

3.2.1 Problem Formulation

We first consider a scenario in which the feasible precoding set is $\mathbb{C}^{N_T \times M}$ and the number of testing points in \mathcal{P} is large. In this case, the optimal solution to (3.4) derived in [42] might be overwhelming to compute. To address this issue, we propose a discretization approach to significantly reduce the size of the constraint space of (3.4). We assume perfect transmitter and receiver channel knowledge. We also assume that the transmitter can calculate the characteristic exposure matrix $\mathbf{R}(p)$ at any testing point $p \in \mathcal{P}$ as in Chapter 2.

3.2.2 Discretization

The precoder design problem in (3.4) can also be seen as a semi-infinite programming (SIP) problem by expressing it as

$$\begin{aligned} \max_{\mathbf{F} \in \mathcal{F}} \quad & \log \left| \mathbf{I} + \frac{1}{\sigma^2} \mathbf{H} \mathbf{F} \mathbf{F}^H \mathbf{H}^H \right| \\ \text{s.t.} \quad & \text{tr}(\mathbf{F}^H \mathbf{F}) \leq P_T \\ & \text{tr}(\mathbf{F}^H \mathbf{R}(p) \mathbf{F}) \leq Q \forall p \in \mathcal{P}. \end{aligned} \quad (3.7)$$

SIPs refer to optimizations in which the number of constraints is infinite. These problems arise naturally in many fields and are generally difficult to solve in closed-form unless the problem satisfies certain conditions [57].

One common and intuitive method for solving SIPs known as discretization approximates the infinite constraint space \mathcal{P} as a finite set. The resulting optimization problem with a finite number of constraints can then be solved through other methods depending on the structure of the problem. Let $\text{PF}[\mathcal{P}']$ denote the optimization problem

$$\begin{aligned} \text{PF}[\mathcal{P}'] : C[\mathcal{P}'] = \max_{\mathbf{F} \in \mathcal{F}} \quad & \log \left| \mathbf{I} + \frac{1}{\sigma^2} \mathbf{H} \mathbf{F} \mathbf{F}^H \mathbf{H}^H \right| \\ \text{s.t.} \quad & \text{tr}(\mathbf{F}^H \mathbf{F}) \leq P_T \\ & \text{EXP}(\mathbf{F}, \mathcal{P}') \leq Q, \end{aligned} \quad (3.8)$$

and let $\mathbf{F}[\mathcal{P}']$ be a solution to $\text{PF}[\mathcal{P}']$. The main idea is to obtain a finite set $\mathcal{P}_d \subseteq \mathcal{P}$, referred to as a grid, such that $C[\mathcal{P}_d] \approx C[\mathcal{P}]$. The desired grid, if it exists, may still contain a large number of points and yield a problem which cannot be efficiently solved. An alternative approach is to define or compute a nested grid sequence, i.e., $\{\mathcal{P}_k\}$ with $\mathcal{P}_k \subseteq \mathcal{P}_{k+1}$ for all k , and iteratively solve the problem $\text{PF}[\mathcal{P}_k]$ until the solution converges to optimality.

We make the following assumptions to simplify our analysis:

(A3) : The set of testing points \mathcal{P} is compact.

(A4) : The function $\text{tr}(\mathbf{F}^H \mathbf{R}(p) \mathbf{F})$, where $\mathbf{R}(p)$ corresponds to one of the considered exposure metrics, is continuous over \mathcal{P} for any precoder \mathbf{F} .

The first of these assumptions is reasonable since exposure decreases as a function of distance from the transmitter and therefore \mathcal{P} can be defined as some closed set with points bounded as within a sphere of norm D_{\max} . Additionally, electromagnetic fields are continuous in most cases, implying that (A4) holds.

We propose the use of an efficient discretization algorithm in [58] along with the modified waterfilling algorithm from [42] to solve $\text{PF}[\mathcal{P}]$. The main idea is to iteratively identify the points in \mathcal{P} that correspond to active constraints. Let the initial grid \mathcal{P}_0 consist of a single point p_0 and solve $\text{PF}[\mathcal{P}_0]$ to obtain the precoder $\mathbf{F}[\mathcal{P}_0]$. The following grid $\mathcal{P}_1 = \{p_0, p_1^*\}$ is obtained by finding a point p_1^* that has the largest exposure value given the current precoder as

$$p_1^* = \underset{p \in \mathcal{P}}{\text{argmax}} \text{tr}(\mathbf{F}_0^H \mathbf{R}(p) \mathbf{F}_0). \quad (3.9)$$

A new precoder $\mathbf{F}[\mathcal{P}_1]$ is obtained by solving $\text{PF}[\mathcal{P}_1]$ and the process is repeated.

A summary of the proposed algorithm is provided in Algorithm 1. Note that the assumptions (A3) and (A4) ensure the existence of a maximal exposure point in each iteration. In the context of our discussion, the algorithm probes the constraint space with near-optimal precoders to find the exposure hotspots. If at any point in the algorithm we have that $\mathcal{P}_{k+1} = \mathcal{P}_k$, then the algorithm can be stopped since this implies that $\mathbf{F}[\mathcal{P}_k]$ is a feasible precoder, and $\mathcal{P}_k \subseteq \mathcal{P}$ gives that $C[\mathcal{P}_k] \geq C[\mathcal{P}]$. However, there is no guarantee that this condition occurs, so an alternative stopping criterion should be defined, for example, when $|C[\mathcal{P}_{k-1}] - C[\mathcal{P}_k]|/C[\mathcal{P}_k]$ is smaller than a predetermined threshold. This convergence criterion may result in a solution that exceeds the exposure constraint, but this issue can be remedied by setting the exposure constraint to be slightly lower than desired or by performing a small power back-off.

Algorithm 1 Discretization Algorithm

Input: $p_0, \mathbf{R}(p), P_T, Q$

- 1: Set $\mathcal{P}_0 := \{p_0\}$ and $k := 0$
- 2: **while** Stopping criteria not met **do**
- 3: Find a solution $\mathbf{F}_k = \mathbf{F}[\mathcal{P}_k]$ for PF(\mathcal{P}_k) using the modified waterfilling algorithm
- 4: Set $\mathcal{P}_{k+1} = \mathcal{P}_k \cup \{p_{k+1}^*\}$, where p_{k+1}^* is a solution to

$$\max_{p \in \mathcal{P}} \text{tr} \left(\mathbf{F}_k^H \mathbf{R}(p) \mathbf{F}_k \right)$$

- 5: $k \rightarrow k + 1$
 - 6: **end while**
-

The convergence of general discretization approaches depends heavily on the type of problem considered. The following lemma shows that Algorithm 1 converges to an optimal solution of $\text{PF}[\mathcal{P}]$.

Lemma 3.2.1 *Under assumptions (A3) and (A4), a solution to the problem $\text{PF}[\mathcal{P}]$ exists and $\lim_{k \rightarrow \infty} C[\mathcal{P}_k] = C[\mathcal{P}]$.*

Proof Let $\mathcal{F}(\mathcal{P}')$ denote the set of feasible points

$$\mathcal{F}(\mathcal{P}') = \left\{ \mathbf{F} \in \mathcal{F} : \text{tr}(\mathbf{F}^H \mathbf{F}) \leq P_T, \text{tr}(\mathbf{F}^H \mathbf{R}(p) \mathbf{F}) \leq Q, p \in \mathcal{P}' \right\}, \quad (3.10)$$

and $L(\mathbf{F}, \mathcal{P}')$ denote the feasible level set

$$L(\mathbf{F}, \mathcal{P}') = \{ \mathbf{F}' \in \mathcal{F} : C(\mathbf{F}') \leq C(\mathbf{F}) \} \cap \mathcal{F}(\mathcal{P}'), \quad (3.11)$$

where $C(\mathbf{F})$ is the objective function of $\text{PF}[\mathcal{P}]$. We show that $\mathcal{F}(\mathcal{P})$ is nonempty, and $L(\mathbf{F}, \{p_0\})$ is bounded for some \mathbf{F} . These conditions, combined with assumptions, (A3) and (A4) allow us to apply Theorem 2.1 in [58] to complete the proof.

The set of feasible points is clearly nonempty since we have $\mathbf{0} \in \mathcal{F}(\mathcal{P})$. Now let $p_0 \in \mathcal{P}$ and $\mathbf{F} \in \mathcal{F}$ be arbitrary and let $\mathcal{F} = \mathbb{C}^{M \times N_T}$ be equipped with the Frobenius norm as its metric. Any precoder $\mathbf{F}' \in L(\mathbf{F}, \{p_0\})$ must satisfy the transmit power constraint, so we have that

$$0 \leq \|\mathbf{F}'\|_F \leq \sqrt{P_T}. \quad (3.12)$$

Therefore, $L(\mathbf{F}, \{p_0\})$ is bounded, as desired. ■

An analysis of the rate of convergence of Algorithm 1 was not performed, but our simulation results show that the algorithm converges in less than five iterations for a variety of initial points.

3.2.3 Numerical Results

We now present simulation results for the proposed precoding schemes in a 28 GHz uplink scenario. The transmitter and receiver are equipped with ideal half-wave

dipole ULAs with $\lambda/2$ spacing. We assume the receive array has $N_R = 16$ elements in all simulations. We perform Monte Carlo simulations with the i.i.d. realizations of the channel model in (3.2) with $L = 6$ clusters, and AOAs and AODs uniformly distributed in $[0, 2\pi)$. The transmitter is assumed to be at a distance of 5 mm from a spherical head model with radius 9 cm corresponding to statistical body size measurements obtained from [59].

An incident PD constraint is placed on the head at points lying in the azimuth plane with line-of-sight to the center of the transmitter array. Rather than placing constraints over a continuous region, we consider a more practical case in which there are 21 evenly distributed testing points. For the given head model, this corresponds to points on the head at boresight angles less than 71.33° that are spaced 1.5 mm apart. PD matrices are calculated with the proposed ideal baseband model in (2.16). The performance of the proposed scheme is compared with the worst-case power back-off method, in which the power of the optimal precoder without exposure constraints is reduced by a factor of γ_{worst} , where

$$\gamma_{\text{worst}} = \min \left\{ 1, \frac{Q}{Q_{\text{worst}}} \right\}, \quad (3.13)$$

and Q_{worst} is the worst-case exposure reading

$$Q_{\text{worst}} = \max_{\substack{\mathbf{F} \in \mathcal{F} \\ \text{tr}(\mathbf{F}^H \mathbf{F}) \leq P_T}} \text{EXP}(\mathbf{F}, \mathcal{P}). \quad (3.14)$$

In the first experiment, the exposure constraint is set to $Q = 5 \text{ mW/cm}^2$, and we fix the noise variance as $\sigma^2 = 1$. In Fig. 3.1, we vary the transmit power and show the capacity performance of the power back-off and the discretization approach. Results for a higher number of data streams are omitted since both the traditional and modified waterfilling algorithms pour all power into a single channel eigenmode at low transmit SNRs. The proposed method shows a rate improvement over the power back-off approach when both the transmit power constraint and exposure constraint are active. This gain becomes more significant as the transmit power increases since the back-off scheme restricts beams to a fixed power level to ensure induced exposures

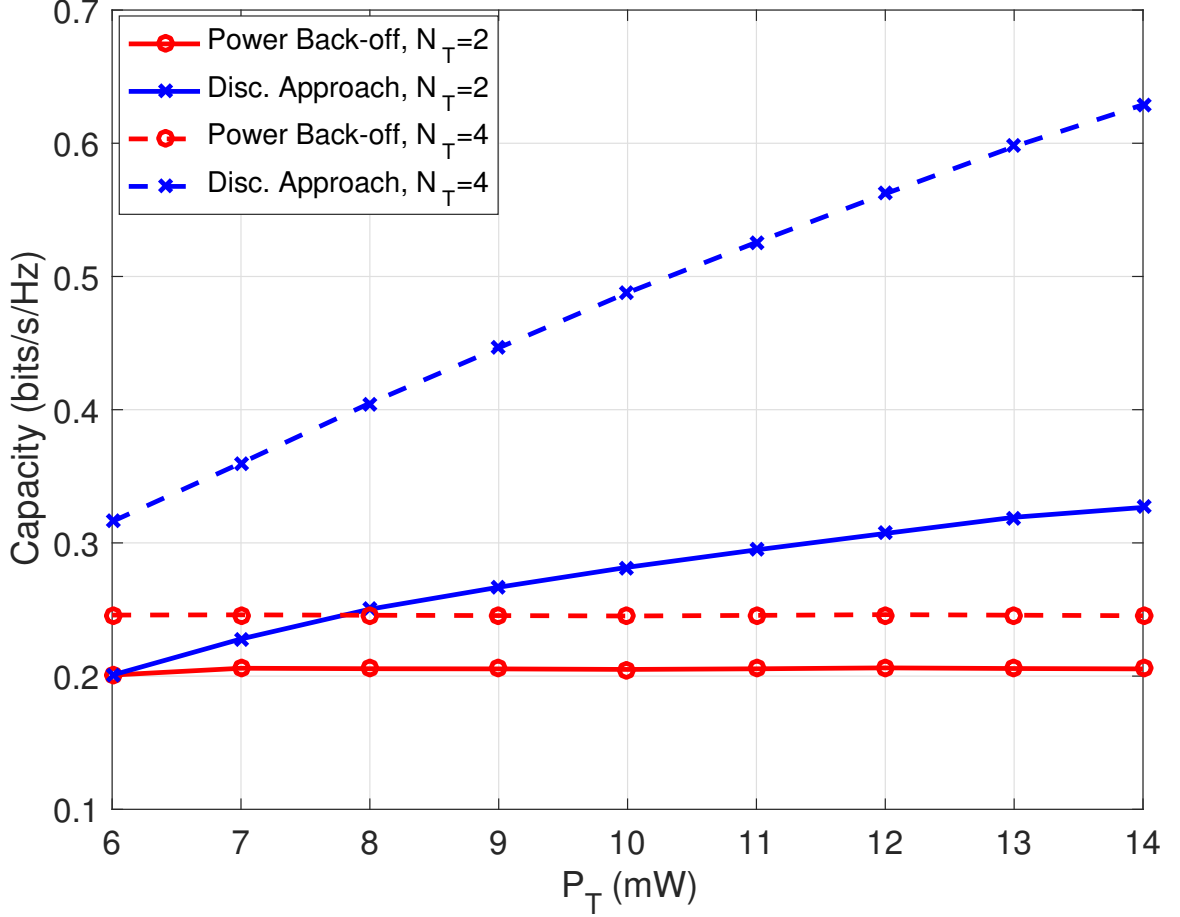


Fig. 3.1. Capacity vs. the transmit power constraint P_T for the proposed discretization approach and worst-case power back-off. The exposure constraint and noise variance are fixed to $Q = 5 \text{ mW/cm}^2$ and $\sigma^2 = 1$, respectively.

lie below the exposure limit. However, the capacity achieved by the proposed methods also reaches an asymptotic value since the exposure constraint becomes the only active constraint at high values of P_T .

In Fig. 3.2, the transmit power is set to $P_T = 10 \text{ mW}$ and the PD constraint is varied. The noise variance is fixed to give a 0 dB transmit SNR. We consider the feasible precoding set $\mathbb{C}^{N_T \times M}$. The results demonstrate that the proposed methods outperform the power back-off method, especially for lower exposure thresholds. Again, all

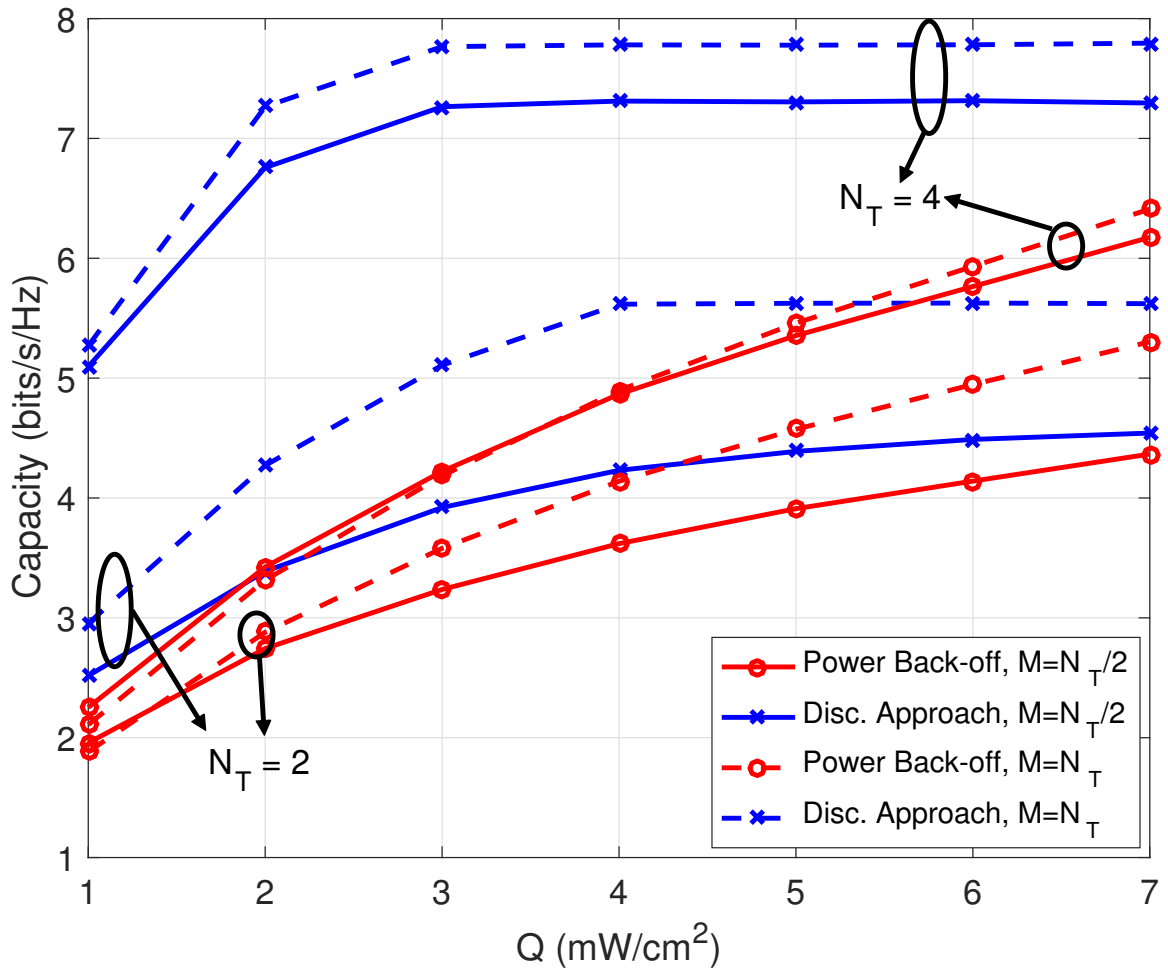


Fig. 3.2. Capacity vs. the exposure constraint Q with transmit power $P_T = 10$ mW. The transmit SNR is fixed to 0 dB.

methods exhibit an asymptotic behavior since the probability of an active exposure constraint decreases as Q increases. Note that in the case $N_T = 4$, the power back-off method with $M = 2$ performs worse than with $M = 4$ at low PD thresholds, as shown in Fig. 3.2. This is because waterfilling is performed prior to the power back-off and the lowered water level may be highly suboptimal for large power reductions. A more detailed discussion of this phenomenon can be found in [42].

3.3 Position-Based Adaptive Power Back-Off

3.3.1 Problem Formulation

We assume the transmitter employs codebook-based beamforming with $M = 1$ data streams. The beamforming direction is constrained to a predetermined transmission codebook \mathcal{C} , but the system is able to adaptively reduce the transmit power as needed. Uplink power control is important for managing interference between users in cellular systems and is currently employed in 5G NR [60–62]. Here, however, we propose its use as a means for complying with exposure limitations. A maximum transmit power constraint is also placed on the system as $\|\mathbf{f}\|^2 \leq P_T$, where P_T is the power constraint. The feasible beamforming set is, therefore, given as

$$\mathcal{F} = \{ \sqrt{\gamma} \mathbf{f} : \mathbf{f} \in \mathcal{C}, \gamma \in [0, 1] \}, \quad (3.15)$$

where γ is the adaptive power back-off constant and \mathcal{C} is the beamforming direction codebook composed of vectors with power P_T . The max-SNR beamformer optimization problem under an exposure constraint is given as

$$\begin{aligned} \max_{\mathbf{f} \in \mathcal{F}} \quad & \|\mathbf{H}\mathbf{f}\|^2 \\ \text{s.t.} \quad & \text{EXP}(\mathbf{f}, \mathcal{P}) \leq Q, \end{aligned} \quad (3.16)$$

where $\text{EXP}(\mathbf{f})$ is a function which gives the time-averaged exposure induced by the device when transmitting with the beamformer \mathbf{f} , and Q is the regulatory threshold. We assume the receiver is able to estimate the receive SNR of each beam in \mathcal{C} , for example, by transmitting pilot symbols, and that this information is fed back to the transmitter.

3.3.2 Dynamic Exposure Model

We consider a millimeter wave exposure scenario in which the user's head is located near the transmitter array, as seen in Fig. 3.3. The array is located in the xy -plane and is centered at the origin. The head is modeled as a sphere of radius R_{head} centered

on the y -axis. The distance between the center of the array and the head is denoted as d , and ϕ denotes the tilt angle between the y -axis and the array. An exposure constraint is placed on the system as per regulatory standards for millimeter wave systems [20]. During testing, multiple exposure cases are considered in order to identify the location of worst-case exposure. We assume that average PD values are to be monitored over the region \mathcal{P} on the surface of the head and that the system must satisfy the constraint

$$\text{PD}_{\mathcal{P}}(\mathbf{f}, \boldsymbol{\tau}) \leq Q, \quad (3.17)$$

where $\boldsymbol{\tau} = [d, \phi]^T$ is a vector which characterizes the position of the device relative to the head and $\text{PD}_{\mathcal{P}}(\mathbf{f}, \boldsymbol{\tau})$ is the average PD over \mathcal{P} induced by an array with beamformer \mathbf{f} and location parameter $\boldsymbol{\tau}$. We assume that \mathcal{P} is a region in the xy -plane since maximum exposure will occur in this plane.

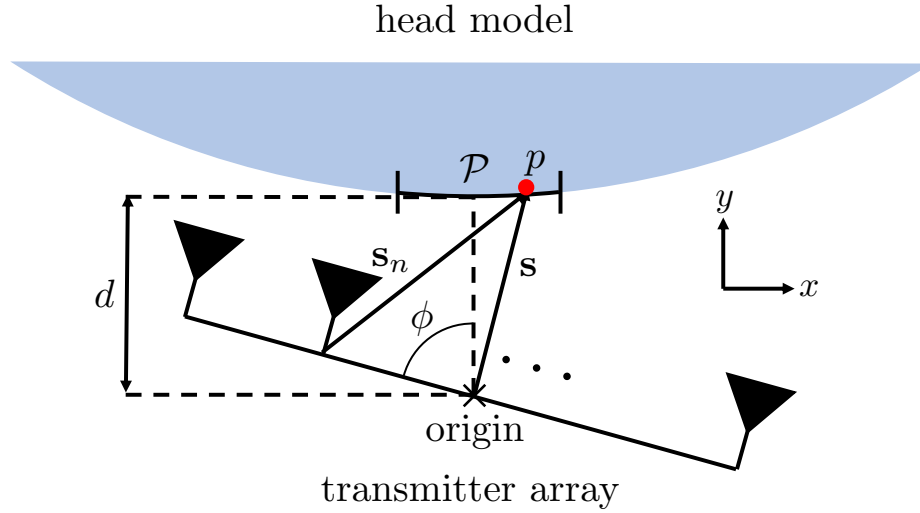


Fig. 3.3. Diagram of the considered exposure scenario. A ULA in the xy -plane is located near a spherical head model. The distance between the array and the head is d , and the array is tilted at an angle ϕ . Average PD levels are monitored over the region \mathcal{P} in the xy -plane. For a point p in the region, \mathbf{s} denotes the position vector from the center of the array to p , and \mathbf{s}_n denotes the position vector from the n -th array element to p .

Rather than directly modeling average exposure, we use the pointwise exposure model for PD discussed in [63]. Let p be a point in the region \mathcal{P} , and let \mathbf{s} and \mathbf{s}_n denote the position vector from the center of the array to p and from the n -th antenna to p , respectively. Work in [63] demonstrates that PD at p can be well-approximated as

$$\text{PD}_p(\mathbf{f}, \boldsymbol{\tau}) = \left| \mathbf{f}^H \mathbf{r}_p(\boldsymbol{\tau}) \right|^2, \quad (3.18)$$

where $\mathbf{r}_p(\boldsymbol{\tau})$ is a length N_T vector which characterizes PD at p . More importantly, [63] also gives an expression to calculate $\mathbf{r}_p(\boldsymbol{\tau})$ for any p , d , and ϕ . Let $\mathbf{a}_{\text{nf}}(\mathbf{s})$ denote the near-field array response vector of the transmitter at p , which is given as

$$\mathbf{a}_{\text{nf}}(\mathbf{s}) \triangleq \left[\gamma_1 e^{-j\varphi_1} \quad \gamma_2 e^{-j\varphi_2} \quad \dots \quad \gamma_{N_T} e^{-j\varphi_{N_T}} \right]^T, \quad (3.19)$$

where

$$\varphi_n = \frac{2\pi (\|\mathbf{s}_n\| - \|\mathbf{s}\|)}{\lambda}, \quad (3.20)$$

$$\gamma_n = \frac{\|\mathbf{s}\|}{\|\mathbf{s}_n\|}, \quad (3.21)$$

and λ is the transmission wavelength. Then, the PD vector for an array of isotropic antennas is given as

$$\mathbf{r}_p(\boldsymbol{\tau}) = \sqrt{\frac{1}{4\pi\|\mathbf{s}\|^2}} \mathbf{a}_{\text{nf}}(\mathbf{s}). \quad (3.22)$$

Note that, given the array geometry, \mathbf{s} and \mathbf{s}_n can be calculated from p and $\boldsymbol{\tau}$. In addition, expressions for \mathbf{r}_p for scenarios with non-ideal antenna gain patterns are discussed in [63].

Results in [63] also demonstrate that by appropriately sampling \mathcal{P} , average exposure can be estimated as

$$\text{PD}_{\mathcal{P}}(\mathbf{f}, \boldsymbol{\tau}) \approx \frac{1}{K} \sum_{k=1}^K \text{PD}_{p_k}(\mathbf{f}, \boldsymbol{\tau}), \quad (3.23)$$

where K is the number of sample points and p_k is the k -th sample point. Therefore, we express the exposure constraint on the system as

$$\text{PD}(\mathbf{f}, \boldsymbol{\tau}) = \frac{1}{K} \sum_{k=1}^K \left| \mathbf{f}^H \mathbf{r}_k(\boldsymbol{\tau}) \right|^2 \leq Q, \quad (3.24)$$

where we let $\mathbf{r}_k = \mathbf{r}_{p_k}$ denote the PD vector for the k -th sample point, for simplicity.

It is important to note that $\mathbf{r}_k(\boldsymbol{\tau})$ is dependent on d and ϕ through \mathbf{s} and \mathbf{s}_n . As the device moves, the exposure induced by the device will naturally change. We assume the device is able to measure d and ϕ using a proximity sensor and calculate $\mathbf{r}_k(\boldsymbol{\tau})$ using (3.22). Therefore, the device can estimate the induced exposure $\text{PD}(\mathbf{f}, \boldsymbol{\tau})$ for any \mathbf{f} , d and ϕ .

3.3.3 Power Back-Off Schemes

Current wireless systems deal with exposure constraints by decreasing the transmit power. In such a scheme, a power reduction factor $\gamma(\mathbf{f}, \boldsymbol{\tau}) \in [0, 1]$ is computed as a function of \mathbf{f} and $\boldsymbol{\tau}$ so that $\sqrt{\gamma(\mathbf{f}, \boldsymbol{\tau})}\mathbf{f}$ obeys the exposure constraint. The system then beamforms with $\sqrt{\gamma(\mathbf{f}_{\text{opt}}, \boldsymbol{\tau})}\mathbf{f}_{\text{opt}}$, where

$$\mathbf{f}_{\text{opt}} = \underset{\mathbf{f} \in \mathcal{C}}{\text{argmax}} \|\mathbf{H}\mathbf{f}\|^2. \quad (3.25)$$

While this is not an optimal solution to (3.16), power back-off provides a practical method for finding feasible solutions to the exposure-constrained beamforming problem. We now discuss two strategies for computing $\gamma(\mathbf{f}, \boldsymbol{\tau})$.

Regulation agencies compare worst-case exposure measurements to thresholds to determine compliance. Therefore, γ is typically computed as

$$\gamma_{\text{worst}} = \min \left\{ 1, \frac{Q}{Q_{\text{worst}}} \right\}, \quad (3.26)$$

where Q_{worst} is the worst-case exposure reading among all transmit signals, gestures, and relative device positions. In the considered setting, this quantity can be calculated as

$$Q_{\text{worst}} = \max_{\mathbf{f} \in \mathcal{F}, \boldsymbol{\tau} \in \mathcal{T}} \text{PD}(\mathbf{f}, \boldsymbol{\tau}), \quad (3.27)$$

where \mathcal{T} denotes the set of feasible distances and tilt angles.

Worst-case power reduction is highly restrictive since it unnecessarily attenuates all signals regardless of their expected emissions. However, this problem can be

alleviated by computing the power back-off factor as a function of the current induced exposure. For each beamformer \mathbf{f} in the codebook, we can calculate

$$\gamma_{\text{adp}}(\mathbf{f}, \boldsymbol{\tau}) = \min \left\{ 1, \frac{Q}{\text{PD}_{\mathcal{P}}(\mathbf{f}, \boldsymbol{\tau})} \right\}. \quad (3.28)$$

Clearly, $\gamma_{\text{adp}}(\mathbf{f}, d)$ is the largest γ for which the beamformer $\sqrt{\gamma}\mathbf{f}$ satisfies both the exposure and power constraint.

Previous studies have addressed adaptive power back-off only as a function of the transmit signal [35, 42]. One issue with the proposed scheme, however, is that updating the adaptive power back-off factors each time $\boldsymbol{\tau}$ changes may be impractical and computationally intensive for general codebooks. To address this, we show how the complexity of computing $\gamma_{\text{adp}}(\mathbf{f}, \boldsymbol{\tau})$ can be significantly reduced by employing a DFT codebook.

3.3.4 DFT Codebook Implementation

Let $N_T O$ be the size of the DFT codebook for some positive integer O and let \mathbf{W} denote the $N_T O \times N_T O$ DFT matrix with entries

$$\mathbf{W}_{i,k} = e^{-j2\pi \frac{(i-1)(k-1)}{N_T O}} \quad (3.29)$$

for $i = 1, 2, \dots, N_T O$ and $k = 1, 2, \dots, N_T O$. The DFT-based beamforming vectors are obtained from the first N_T rows of \mathbf{W} as

$$\mathbf{f}^{(i)} = \sqrt{\frac{P_T}{N_T}} \left[1 \ e^{-j2\pi \frac{i}{N_T O}} \ \dots \ e^{-j2\pi \frac{(N_T-1)i}{N_T O}} \right]^T, \quad (3.30)$$

where $i = 1, 2, \dots, N_T O$. Our goal is to efficiently calculate γ_{adp} for each $\mathbf{f}^{(i)}$. For convenience, we drop the dependence of exposure on d .

Let $\hat{\mathbf{r}}_k = [\mathbf{r}_k^T \ \mathbf{0}^T]^T$ be the length $N_T O$ vector obtained by zero-padding the length N_T vector \mathbf{r}_k . The $N_T O$ -point inverse DFT (IDFT) of $\hat{\mathbf{r}}_k$ is then given as

$$\mathbf{z}_k = \frac{1}{N_T O} \mathbf{W}^H \hat{\mathbf{r}}_k. \quad (3.31)$$

Moreover, we have that

$$\text{PD}_k(\mathbf{f}^{(i)}) = P_T N_T O^2 |z_{ik}|^2, \quad (3.32)$$

where z_{ik} is the i -th element of \mathbf{z}_k . The average exposure constraint for $\mathbf{f}^{(i)}$ can be expressed as

$$\text{PD}_{\mathcal{P}}(\mathbf{f}^{(i)}) = \frac{1}{K} \sum_{k=1}^K P_T N_T O^2 |z_{ik}|^2. \quad (3.33)$$

Therefore, we have

$$\gamma_{\text{adp}}^{(i)} = \gamma_{\text{adp}}(\mathbf{f}^{(i)}) = \min \left\{ 1, \frac{QK}{\sum_{k=1}^K P_T N_T O^2 |z_{ik}|^2} \right\}, \quad (3.34)$$

and the exposure-aware codebook is $\tilde{\mathcal{F}} = \left\{ \sqrt{\gamma_{\text{adp}}^{(i)}} \mathbf{f}^{(i)} \right\}_{i=1}^{N_T O}$.

In practice, DFTs and IDFTs can be performed very efficiently via efficient FFT implementations, which makes the proposed DFT-based transmission an attractive alternative over other exposure-aware schemes. The effective channel gain can also be computed as an IDFT to reduce the difficulty of the beamformer search. In addition, DFT codebooks are realizable in millimeter wave systems constrained to analog beamforming architectures.

3.3.5 Numerical Results

We now present simulation results for the proposed scheme in a 28 GHz uplink scenario. We assume the receiver and transmitter are equipped with ULAs with $N_R = 16$ and $N_T = 2$ ideal isotropic antennas, respectively. The user's head is modeled as a sphere with radius $R_{\text{head}} = 9$ cm, corresponding to statistical body size measurements obtained from [59]. An incident PD constraint is placed on the head at points lying in the azimuth plane, since this is the plane of maximum exposure. The region \mathcal{P} is set to be an arc of measure 5° centered at boresight from the array. This region was uniformly sampled with $K = 51$ points to obtain the exposure constraint in (4.5).

In Fig. 3.4, we plot the maximum possible PD at points at the center and edges of \mathcal{P} for a transmit power of $P_T = 10$ mW. The tilt angle ϕ was fixed as $\phi = 90^\circ$, and

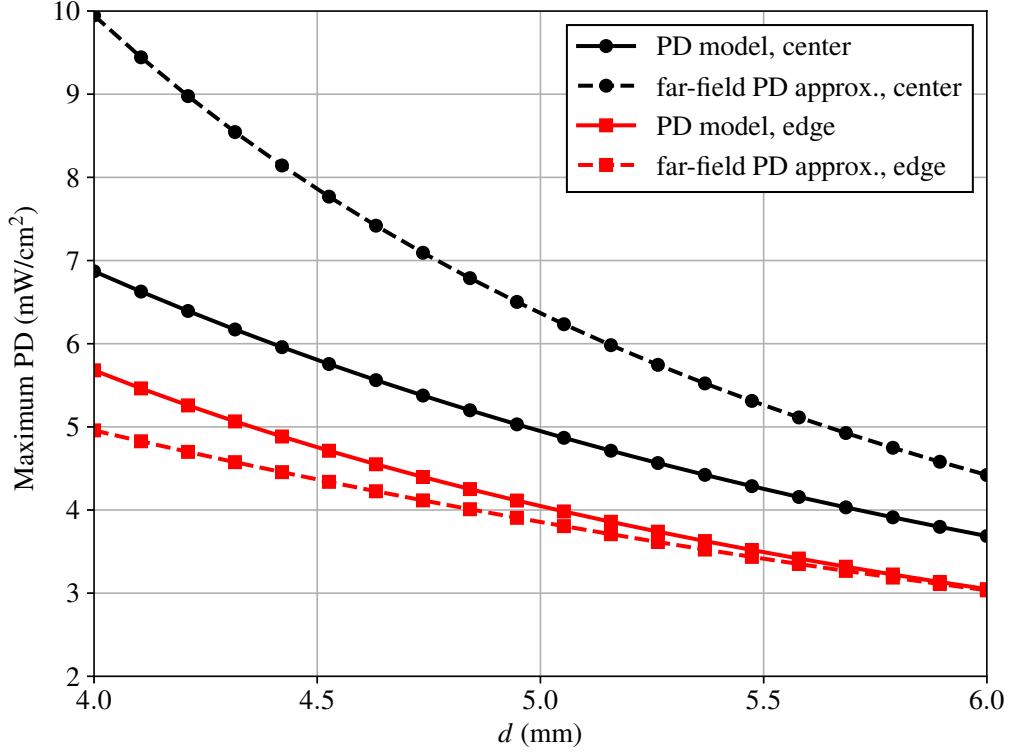


Fig. 3.4. Maximum possible PD vs. the distance d at points in the center and edge of the region \mathcal{P} for a transmitter with transmit power $P_T = 10$ mW and $\phi = 90^\circ$.

the distance d was varied in the range from 4 to 6 mm. The solid lines are obtained from the PD model by taking $P_T \|\mathbf{r}\|^2$, where \mathbf{r} is the PD vector for the considered point. The dashed lines show an ideal far-field approximation in which the maximum PD at a point p is given as

$$\text{PD}_{\text{ff}} = \frac{N_T P_T}{4\pi D_p^2}, \quad (3.35)$$

where D_p is the distance from the center of the array to p . Note that the far-field approximation yields notably different values at points close to the array. This indicates that the PD model is necessary to appropriately reduce the transmit power as needed.

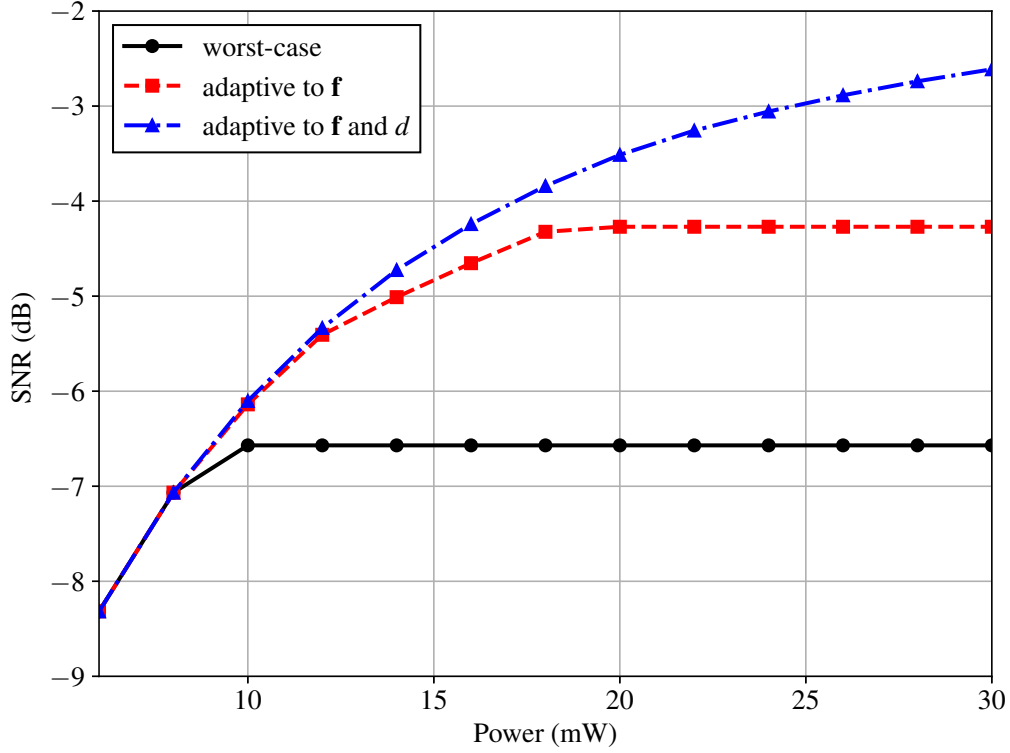


Fig. 3.5. Average receive SNR vs. the transmit power P_T for the different power back-off schemes applied to a DFT codebook. The exposure constraint is $Q = 4 \text{ mW/cm}^2$ and the noise variance $\sigma^2 = 1$. The distance d is uniformly distributed in $[4, 6]$ mm and the tilt angle is as $\phi = 90^\circ$

We compare the receive SNR achieved by applying the power back-off schemes to a DFT codebook with factor $O = 2$. We perform Monte Carlo simulations with i.i.d. realizations of the channel model in (3.2) with $L = 6$ clusters, cluster gains distributed as $\mathcal{CN}(0, 1)$, and AOAs and AODs uniformly distributed in $[0, 2\pi)$. The distance d from the transmitter to the user is modeled as a uniformly distributed random variable in the interval $[4, 6]$ mm. The PD constraint is fixed as $Q = 4 \text{ mW/cm}^2$ according to the proposed FCC guidelines [64].

Performance results for a fixed tilt angle of $\phi = 90^\circ$ are shown in Fig. 3.6. Worst-case back-off reduces power so that all beams in the DFT codebook satisfy the PD constraint at the worst-case distance of 4 mm. Adaptive back-off for \mathbf{f} means that γ is computed only as a function of the beamformer and the worst-case distance. Adaptive back-off for \mathbf{f} and d signifies that the \mathbf{r}_k are calculated for each d in order to update the exposure constraint, and power reduction depends on d and \mathbf{f} . At $P_T = 30$ mW, adapting the power back-off as a function of both \mathbf{f} and d leads to a gain of 1.5 dB over the scheme which only adapts to \mathbf{f} .

Fig. 3.5 demonstrates the performance of the power back-off schemes when ϕ is additionally modeled as a uniformly distributed random variable in the range $[60^\circ, 120^\circ]$. Note that the overall performance of the system decreases due to an increase in exposure values at certain tilt angles. The position-based power back-off adapts to \mathbf{f} , d , and ϕ , and this scheme shows a significant performance benefit over the other back-off methods.

3.4 Conclusion

In this chapter, we demonstrated how exposure models allow us to formulate a signal design problem with a transmit power constraint and an exposure constraint. We developed two exposure-aware transmission strategies as applications of the signal-level exposure model developed in Chapter 2. We first presented a discretization approach for optimal precoding when the number of exposure constraints is large. The proposed algorithm leverages the pointwise exposure models to iteratively add constraints to the precoder optimization as needed. We then examined the advantages of adjusting the transmit power levels of exposure-constrained depending on both the transmit signal and the position of the device relative to the user. We also propose the use of a DFT codebook in order to simplify the recalculation of the power back-off factors when the device moves. Numerical results demonstrate that the proposed schemes outperforms traditional power back-off methods.

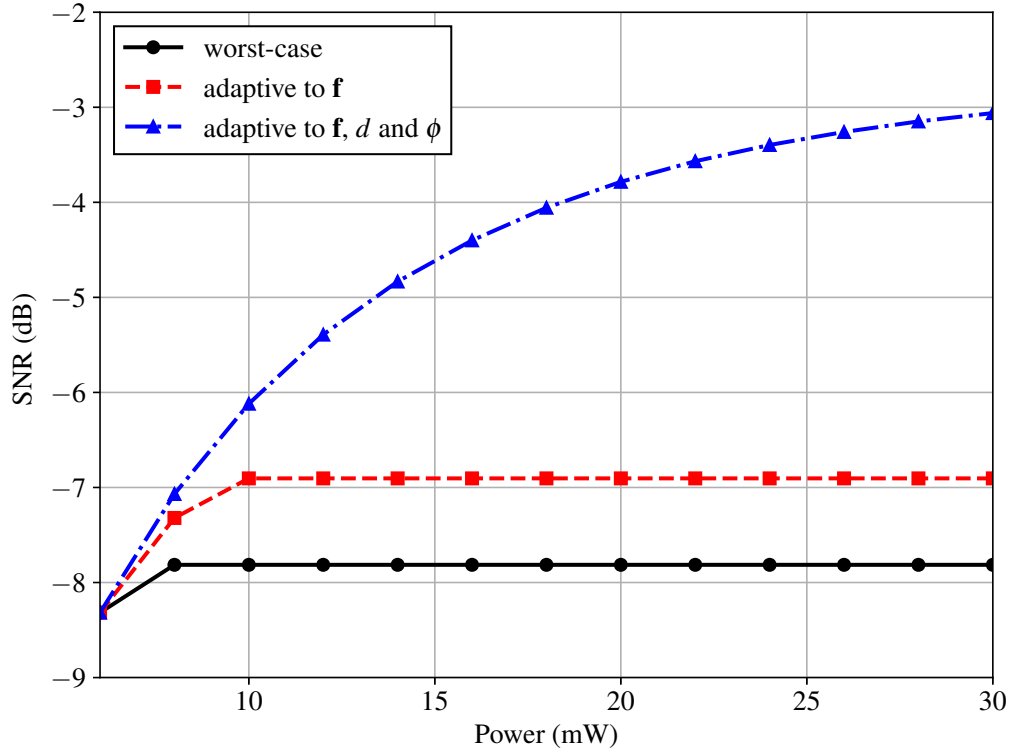


Fig. 3.6. Average receive SNR vs. the transmit power P_T for the different power back-off schemes applied to a DFT codebook. The exposure constraint is $Q = 4 \text{ mW/cm}^2$ and the noise variance $\sigma^2 = 1$. The distance d and the angle ϕ are uniformly distributed in the ranges $[4, 6]$ mm and $[60^\circ, 120^\circ]$, respectively.

4. BEAMFORMING PERTURBATION APPROACH FOR MITIGATING USER EXPOSURE

4.1 System Model

We consider an uplink MIMO system in which a transmitter with N_T antennas communicates with a receiver with N_R antennas. We assume a narrowband transmission where the transmitter beamforms a data symbol $s \in \mathbb{C}$, and the receiver obtains the signal $\mathbf{y} \in \mathbb{C}^{N_R}$, given by

$$\mathbf{y} = \mathbf{H}\mathbf{f}s + \mathbf{n}. \quad (4.1)$$

Here, $\mathbf{H} \in \mathbb{C}^{N_R \times N_T}$ is the channel between the UE and the BS, $\mathbf{f} \in \mathbb{C}^{N_T}$ is the beamforming vector, and $\mathbf{n} \in \mathbb{C}^{N_R}$ is the AWGN noise vector with entries distributed as $\mathcal{CN}(0, \sigma^2)$. We assume that the transmit symbol is zero-mean and unit-variance, i.e., $\mathbb{E}[s] = 0$ and $\mathbb{E}[s^H s] = 1$. The receiver combines \mathbf{y} with a unit-norm vector $\mathbf{z} \in \mathbb{C}^{N_R}$ to obtain an estimate of the data symbol as

$$\hat{s} = \mathbf{z}^H \mathbf{y} = \mathbf{z}^H \mathbf{H}\mathbf{f}s + \mathbf{z}^H \mathbf{n}. \quad (4.2)$$

The achievable rate at the receiver is given as

$$R = \log \left(1 + \frac{1}{\sigma^2} |\mathbf{z}^H \mathbf{H}\mathbf{f}|^2 \right). \quad (4.3)$$

Given \mathbf{H} , R can be maximized by choosing \mathbf{z} and \mathbf{f} to maximize the beamforming gain $|\mathbf{z}^H \mathbf{H}\mathbf{f}|^2$. We assume \mathbf{H} is perfectly known at the receiver and that the transmitter has no knowledge of the channel. With no further constraints on \mathbf{z} , the receiver will combine optimally by employing maximum ratio combining (MRC), which sets $\mathbf{z} = \mathbf{H}\mathbf{f}/\|\mathbf{H}\mathbf{f}\|$, resulting in a beamforming gain of $\|\mathbf{H}\mathbf{f}\|^2$. We assume that the receiver is responsible for selecting a suitable beamformer to maximize $\|\mathbf{H}\mathbf{f}\|^2$ and

that feedback is employed to convey \mathbf{f} to the transmitter. The selection of \mathbf{f} , however, is complicated by power and exposure constraints placed on the user device.

The transmitter is assumed to lie in the vicinity of the user and is, therefore, subject to an exposure constraint in addition to the traditional power constraint. A power constraint can be imposed on the system as $\|\mathbf{f}\|^2 \leq P$, where P is the transmit power limit. Optimal signaling under a single power constraint has been widely studied in the literature.

In a multi-antenna system, the radiated electric field is a result of the superposition of the fields from the individual antenna elements. Therefore, exposure values can vary significantly with the transmit signal. This relationship can be captured with the quadratic model first proposed in [35–37]. In these works, time-averaged exposure over a volume V is modeled as

$$\text{EXP} = \mathbf{f}^H \mathbf{R}_V \mathbf{f}, \quad (4.4)$$

where \mathbf{R}_V is the characteristic *exposure matrix* corresponding to V . Experimental results in [35–37, 39, 41] demonstrate that this model can accurately predict exposure measures such as SAR, power-loss density, and incident PD, in a variety of operating conditions. These studies also address the issue of computing an appropriate exposure matrix \mathbf{R}_V .

Exposure compliance testing typically considers multiple gestures and operating conditions to determine the possible worst-case exposure volumes associated with each case. We let K be the total number of considered averaging volumes, and let V_k be k -th volume chosen as a candidate for worst-case exposure. With the quadratic model in (4.4), an exposure constraint on the system can be expressed as

$$\mathbf{f}^H \mathbf{R}_k \mathbf{f} \leq Q_k, \quad k = 1, 2, \dots, K \quad (4.5)$$

where \mathbf{R}_k is the exposure matrix which characterizes exposure at V_k , and Q_k is the regulatory exposure constraint for the k -th case. As previously mentioned, worst-case exposure must lie below the established threshold for the device to pass exposure

testing, so any feasible beamformer must satisfy each of the K exposure constraints and the power constraint.

Given a channel realization \mathbf{H} , the maximum effective channel gain under power and exposure constraints is given as

$$\begin{aligned} \mathbf{f}_{\text{opt}} = \underset{\mathbf{f}}{\operatorname{argmax}} \quad & \|\mathbf{H}\mathbf{f}\|^2 \\ \text{s.t.} \quad & \mathbf{f}^H \mathbf{f} \leq P, \\ & \mathbf{f}^H \mathbf{R}_k \mathbf{f} \leq Q_k, \quad k = 1, 2, \dots, K. \end{aligned} \quad (4.6)$$

Since all of the constraints are quadratic, the problem can also be written as

$$\begin{aligned} \mathbf{f}_{\text{opt}} = \underset{\mathbf{f}}{\operatorname{argmax}} \quad & \|\mathbf{H}\mathbf{f}\|^2 \\ \text{s.t.} \quad & \mathbf{f}^H \mathbf{R}_k \mathbf{f} \leq Q_k, \quad k = 0, 1, \dots, K, \end{aligned} \quad (4.7)$$

where the power constraint is accounted for by letting $\mathbf{R}_0 = \mathbf{I}$ and $Q_0 = P$. The solution to (4.7) has been studied under various levels of channel state information (CSI) in [42, 43], which demonstrates the exposure constraints behave similarly to spatial correlation at the transmitter. Optimal signaling is not realizable in our scenario since the transmitter lacks channel information and the receiver has no knowledge of the exposure matrices \mathbf{R}_k .

We assume the receiver chooses the beamforming vector by solving

$$\mathbf{f}_P = \underset{\tilde{\mathbf{x}} \in \mathcal{F}}{\operatorname{argmax}} \|\mathbf{H}\tilde{\mathbf{x}}\|^2, \quad (4.8)$$

where \mathcal{F} is the feasible beamforming set. In the case of optimal beamforming, \mathcal{F} is the set of all vectors \mathbf{f} in \mathbb{C}^{N_T} with $\mathbf{f}^H \mathbf{f} = P$. For a codebook-based deployment, we have that $\mathcal{F} = \{\mathbf{f}_1, \mathbf{f}_2, \dots, \mathbf{f}_{|\mathcal{F}|}\}$, where $|\mathcal{F}|$ denotes the number of vector in the codebook. The transmitter receives \mathbf{f}_P through feedback, but the beamformer may not comply with the exposure constraints. Therefore, the transmitter must choose an alternate beamformer which satisfies all constraints.

A suboptimal but practical approach for ensuring exposure compliance is to reduce the transmit power of the beamformer. In a power back-off scheme, the device

calculates a back-off factor $\alpha \in [0, 1]$ such that $\alpha \mathbf{f}_P$ satisfies the exposure constraints, i.e.,

$$\alpha^2 \mathbf{f}_P^H \mathbf{R}_k \mathbf{f}_P \leq Q_k, \quad k = 1, \dots, K. \quad (4.9)$$

In practice, power back-off is generally performed with regards to the worst-case exposure by setting

$$\alpha_{\text{worst}} = \sqrt{\min \left(1, \min_{k=1,2,\dots,K} \frac{Q_k}{\text{EXP}_{k,\text{worst}}} \right)}, \quad (4.10)$$

where $\text{EXP}_{k,\text{worst}}$ is the worst-case exposure for the k -th constraint and is given as

$$\text{EXP}_{k,\text{worst}} = \max_{\mathbf{f}} \mathbf{f}^H \mathbf{R}_k \mathbf{f}. \quad (4.11)$$

Reducing the transmit power on a worst-case basis is simple and forces the system to comply with all of the exposure constraints. In addition, $\text{EXP}_{k,\text{worst}}$ can be measured offline through exposure testing procedures and does not require the use of signal-level exposure models.

Systems can also leverage exposure models to perform power back-off adaptively as a function of the current induced exposure. An adaptive back-off factor can be calculated as

$$\alpha_{\text{adp}} = \sqrt{\min \left(1, \min_{k=1,2,\dots,K} \frac{Q_k}{\mathbf{f}_P^H \mathbf{R}_k \mathbf{f}_P} \right)}. \quad (4.12)$$

By adjusting the power back-off factor to the exposure induced by \mathbf{f}_P , the system achieves better performance than with a worst-case approach. As seen in previous analyses of exposure-constrained channels, however, there is a large gap in performance between the optimal scheme and the power back-off methods. In the following sections, we address the problem of finding an alternative method for obtaining a feasible solution to (4.7) based only on \mathbf{f}_P , \mathbf{R}_k and Q_k .

4.2 Perturbation-Based Beamforming

Our goal is to find a beamforming vector \mathbf{g} which achieves performance close to that of \mathbf{f}_P but satisfies the exposure constraints. To this end, we define a perturbation function $\Phi_h : \mathbb{C}^{N_T} \rightarrow \mathbb{C}^{N_T}$ which maps a vector \mathbf{f} to the solution of the problem

$$\begin{aligned} \Phi_h(\mathbf{f}) = \operatorname{argmin}_{\mathbf{g} \in \mathbb{C}^{N_T}} h(\mathbf{f}, \mathbf{g}) \\ \text{s.t. } \mathbf{g}^H \mathbf{R}_k \mathbf{g} \leq Q_k, \quad k = 0, 1, 2, \dots, K, \end{aligned} \quad (4.13)$$

where $h(\mathbf{f}, \mathbf{g})$ is a metric between the vectors \mathbf{f} and \mathbf{g} . The average distortion induced by the perturbation operation can be characterized through the expected beamforming gain loss incurred by beamforming with $\Phi_h(\mathbf{f}_P)$ instead of \mathbf{f}_P , given as [65]

$$D(\Phi_h) = \mathbb{E}_{\mathbf{H}} \left[\left| \|\mathbf{H}\mathbf{f}_P\|^2 - \|\mathbf{H}\Phi_h(\mathbf{f}_P)\|^2 \right| \right]. \quad (4.14)$$

The perturbation function should therefore be chosen minimize the distortion function. Note that for fixed \mathbf{R}_k and Q_k , the performance of Φ_h is completely specified by h . We now provide upper bounds for the distortion function which yield appropriate choices for h .

4.2.1 Minimum Distance

We first consider a perturbation scheme in which the beamforming vector \mathbf{g} is chosen to be the nearest vector to \mathbf{f}_P in terms of Euclidean distance which satisfies the power and exposure constraints. Note that the expected beamforming gain loss can be bounded as

$$\begin{aligned} D(\Phi_h) &= \mathbb{E} \left[\left| \left(\|\mathbf{H}\mathbf{f}_P\| - \|\mathbf{H}\Phi_h(\mathbf{f}_P)\| \right) \left(\|\mathbf{H}\mathbf{f}_P\| + \|\mathbf{H}\Phi_h(\mathbf{f}_P)\| \right) \right| \right] \\ &\leq 2\sqrt{P}\mathbb{E} \left[\|\mathbf{H}\|_2^2 \|\mathbf{f}_P - \Phi_h(\mathbf{f}_P)\| \right]. \end{aligned} \quad (4.15)$$

Therefore, minimizing the Euclidean distance between \mathbf{f}_P and \mathbf{g} will also minimize the distortion induced by the perturbation.

In this case, the metric is set as

$$h_D(\mathbf{f}, \mathbf{g}) = \|\mathbf{f} - \mathbf{g}\|^2, \quad (4.16)$$

yielding the optimization problem

$$\begin{aligned} \mathbf{g}_D = \Phi_D(\mathbf{f}_P) = \underset{\mathbf{g}}{\operatorname{argmin}} \|\mathbf{f}_P - \mathbf{g}\|^2 \\ \text{s.t. } \mathbf{g}^H \mathbf{R}_k \mathbf{g} \leq Q, \quad k = 0, 1, \dots, K. \end{aligned} \quad (4.17)$$

Note that since we are minimizing the Euclidean distance, it is not necessary to use the phase-invariant distance, given as

$$d(\mathbf{f}, \mathbf{g}) = \min_{\psi \in [0, 2\pi)} \left\| \mathbf{f} - e^{j\psi} \mathbf{g} \right\|. \quad (4.18)$$

If we let $\tilde{\mathbf{g}}_D$ be a solution to the problem

$$\begin{aligned} \tilde{\mathbf{g}}_D = \underset{\mathbf{g}}{\operatorname{argmin}} \min_{\psi \in [0, 2\pi)} \left\| \mathbf{f}_P - e^{j\psi} \mathbf{g} \right\|^2 \\ \text{s.t. } \mathbf{g}^H \mathbf{R}_k \mathbf{g} \leq Q, \quad k = 0, 1, \dots, K, \end{aligned} \quad (4.19)$$

then $e^{j\psi^*} \tilde{\mathbf{g}}_D$, where

$$\psi^* = \underset{\psi \in [0, 2\pi)}{\operatorname{argmin}} \left\| \mathbf{f}_P - \tilde{\mathbf{g}}_D^* \right\|, \quad (4.20)$$

is clearly a solution to (4.17). Moreover, multiplication of the beamforming vector \mathbf{g} by $e^{j\theta}$, where $\theta \in [0, 2\pi)$, does not change the beamforming gain, nor the power of the beam, nor the induced exposure by the beam.

The problem (4.17) is a convex quadratically constrained quadratic program (QCQP). The Lagrangian of this problem can be formulated as

$$L_D(\mathbf{g}, \boldsymbol{\mu}) = \|\mathbf{f}_P - \mathbf{g}\|^2 + \sum_{k=0}^K \mu_k \left(\mathbf{g}^H \mathbf{R}_k \mathbf{g} - Q_k \right), \quad (4.21)$$

where μ_k is the dual variable corresponding to the k -th quadratic constraint and $\boldsymbol{\mu} = [\mu_0 \mu_1 \dots \mu_K]^T$. The following proposition gives the optimal solution for the problem.

Lemma 4.2.1 *Let $Q_k > 0$ for $k = 0, 1, \dots, K$ and define*

$$\mathbf{W}_\mu = \sum_{k=0}^K \mu_k \mathbf{R}_k. \quad (4.22)$$

Let

$$\mathbf{g} = (\mathbf{W}_\mu + \mathbf{I})^{-1} \mathbf{f}_P. \quad (4.23)$$

If there exist dual variables $\{\mu_k\}_{k=0,1,\dots,K}$ that satisfy the conditions

$$\begin{cases} \mathbf{g}^H \mathbf{R}_k \mathbf{g} \leq Q_k, \\ \mu_k > 0, \\ \mu_K (\mathbf{g}^H \mathbf{R}_K \mathbf{g} - Q_K) = 0, \end{cases} \quad (4.24)$$

for $k = 0, 1, \dots, K$, then \mathbf{g}_μ is the optimal solution to (4.17).

Proof: Since the optimization problem in (4.17) is convex and satisfies Slater's condition, the Karush-Kuhn-Tucker (KKT) conditions are necessary and sufficient for the optimality of \mathbf{g} . These conditions are given as

$$\mathbf{g} - \mathbf{f}_P + \mathbf{W}_\mu \mathbf{g} = \mathbf{0}, \quad (4.25)$$

$$\mathbf{g}^H \mathbf{R}_k \mathbf{g} \leq Q_k, \quad (4.26)$$

$$\mu_k \geq 0, \quad (4.27)$$

$$\mu_k (\mathbf{g}^H \mathbf{R}_k \mathbf{g} - Q_k) = 0, \quad (4.28)$$

where $k = 0, 1, \dots, K$. Note that (4.25) can be rearranged to give

$$\mathbf{g} = (\mathbf{W}_\mu + \mathbf{I})^{-1} \mathbf{f}_P. \quad (4.29)$$

Therefore if $\boldsymbol{\mu}$ satisfies the remaining KKT conditions, then \mathbf{g} is optimal. ■

The Lagrange dual problem of (4.17) is given as

$$\boldsymbol{\mu}_D = \operatorname{argmax}_{\boldsymbol{\mu} \geq \mathbf{0}} \min_{\mathbf{g}} L_D(\mathbf{g}, \boldsymbol{\mu}). \quad (4.30)$$

The dual problem is always a convex problem, therefore, we can find always $\boldsymbol{\mu}_D$ which solves the dual. The convexity of (4.17) implies that the problem satisfies

strong duality. Thus, $\boldsymbol{\mu}_D$ satisfies the conditions in the Lemma 1, and $\mathbf{g}_D = \mathbf{g}_{\boldsymbol{\mu}_D}$ is the optimal solution to (4.17). We refer to this scheme as the minimum distance (MinD) perturbation method.

The perturbed beamforming vector \mathbf{g}_D can be decomposed as

$$\mathbf{g}_D = \alpha_D \mathbf{f}_P + \mathbf{e}_D, \quad (4.31)$$

where $\alpha_D \in \mathbb{C}$ is scalar applied to the main beam \mathbf{f}_P and $\mathbf{e}_D^H \mathbf{f}_P = 0$. Note that since $\mathbf{f}_P^H \mathbf{f}_P = P$, we must have that $|\alpha_D| \in [0, 1]$ for any \mathbf{g}_D which satisfies the power constraint. Therefore, $|\alpha_D|$ can be seen as a back-off factor applied to the main beam. Expressions for α_D and \mathbf{e}_D in (4.31) can be obtained. Let $\mathbf{W}_D = \mathbf{W}_{\boldsymbol{\mu}_D}$. Then we have that

$$\alpha_D = \frac{\mathbf{f}_P^H (\mathbf{W}_D + \mathbf{I})^{-1} \mathbf{f}_P}{\mathbf{f}_P^H \mathbf{f}_P}, \quad (4.32)$$

and

$$\mathbf{e}_D = ((\mathbf{W}_D + \mathbf{I})^{-1} - \alpha_D \mathbf{I}) \mathbf{f}_P. \quad (4.33)$$

4.2.2 Maximum Correlation

Consider the case in which \mathbf{f}_P is the optimal beamforming vector without exposure constraints. In other words, $\mathbf{f}_P = \sqrt{P} \mathbf{v}_1$ where \mathbf{v}_1 is the dominant eigenvector of $\mathbf{H}^H \mathbf{H}$. In this case, the distortion measure $D(\Phi_h)$ for an arbitrary fading channel can be bounded as [66]

$$D(\Phi_h) \leq \sqrt{P^2 - \mathbb{E} \left[\left| \mathbf{f}_P^H \Phi_h(\mathbf{f}_P) \right|^2 \right]} \left(\mathbb{E} [\lambda_1] + \sqrt{2 \text{Var} [\lambda_1]} \right), \quad (4.34)$$

where λ_1 is the dominant eigenvalue of $\mathbf{H}^H \mathbf{H}$. Note that the effect of the perturbation on the bound is completely captured by the term $\sqrt{1 - \mathbb{E} \left[\left| \mathbf{f}_P^H \Phi_h(\mathbf{f}_P) \right|^2 \right]}$. Therefore, we can minimize the distortion measure by maximizing the correlation $\left| \mathbf{f}_P^H \Phi_h(\mathbf{f}_P) \right|^2$.

Accordingly, we define the objective function

$$h_C(\mathbf{f}, \mathbf{g}) = - \left| \mathbf{g}^H \mathbf{f} \right|^2, \quad (4.35)$$

yielding the optimization problem

$$\begin{aligned} \mathbf{g}_C = \operatorname{argmax}_{\mathbf{g}} & \left| \mathbf{f}_P^H \mathbf{g} \right|^2 \\ \text{s.t.} & \mathbf{g}^H \mathbf{R}_k \mathbf{g} \leq Q, \quad k = 0, 1, \dots, K. \end{aligned} \quad (4.36)$$

While maximizing the correlation between two vectors \mathbf{f} and \mathbf{g} is equivalent to minimizing the phase-invariant distance $d(\mathbf{f}, \mathbf{g})$ when the norms of \mathbf{f} and \mathbf{g} are fixed, this is not true in general. From (4.18), we have that

$$\begin{aligned} d(\mathbf{f}, \mathbf{g}) &= \min_{\psi \in [0, 2\pi)} \left(\mathbf{f}^H \mathbf{f} - 2 \operatorname{Re} \left(e^{j\psi} \mathbf{f}^H \mathbf{g} \right) + \mathbf{g}^H \mathbf{g} \right) \\ &= \mathbf{f}^H \mathbf{f} - 2 \left| \mathbf{f}^H \mathbf{g} \right| + \mathbf{g}^H \mathbf{g}. \end{aligned} \quad (4.37)$$

Since the norm of \mathbf{g} is not fixed, minimizing $d(\mathbf{f}, \mathbf{g})$ does not correspond with maximizing $\left| \mathbf{f}^H \mathbf{g} \right|^2$.

While (4.36) is not convex, its solution can be obtained through strong duality. Note that (4.36) can also be expressed as

$$\begin{aligned} \mathbf{g}_C = \operatorname{argmax}_{\mathbf{g}} & \log \left(1 + \left| \mathbf{f}_P^H \mathbf{g} \right|^2 \right) \\ \text{s.t.} & \mathbf{g}^H \mathbf{R}_k \mathbf{g} \leq Q, \quad k = 0, 1, \dots, K, \end{aligned} \quad (4.38)$$

which is a maximum capacity analysis problem for rank-one precoding under multiple quadratic constraints given the channel \mathbf{f}_P^H . This problem is a special case of the precoder optimization under multiple quadratic constraints given in [42]. The Lagrangian of (4.38) is given as

$$L_C(\mathbf{g}, \boldsymbol{\mu}) = \log \left(1 + \left| \mathbf{f}_P^H \mathbf{g} \right|^2 \right) - \sum_{k=0}^K \mu_k \left(\mathbf{g}^H \mathbf{R}_k \mathbf{g} - Q_k \right), \quad (4.39)$$

and the dual problem is given by

$$\boldsymbol{\mu}_C = \operatorname{argmin}_{\boldsymbol{\mu} \geq \mathbf{0}} \max_{\mathbf{g}} L_C(\mathbf{g}, \boldsymbol{\mu}). \quad (4.40)$$

The following lemma gives the optimal solution to (4.38).

Lemma 4.2.2 *Let $Q_k > 0$ for $k = 0, 1, \dots, K$ and define*

$$\mathbf{W}_\mu = \sum_{k=0}^K \mu_k \mathbf{R}_k. \quad (4.41)$$

Let $\boldsymbol{\mu}_C$ be the optimal dual variables obtained by solving the dual of (4.38) and $\mathbf{W}_C = \mathbf{W}_{\boldsymbol{\mu}_C}$. Then, the solution to (4.38) is given by

$$\mathbf{g}_C = \frac{\sqrt{\|\mathbf{u}\|^2 - 1}}{\|\mathbf{u}\|^2} \mathbf{W}_C^{-1} \mathbf{f}_P, \quad (4.42)$$

where $\mathbf{u} = \mathbf{W}_C^{-1/2} \mathbf{f}_P$.

Proof: The proof can be found in Theorem 3.6 of [42]. ■

We refer to this scheme as the maximum correlation (MaxC) perturbation method. As before, we have that \mathbf{g}_C can be written as $\mathbf{g}_C = \alpha_C \mathbf{f}_P + \mathbf{e}_C$, where

$$\alpha_C = \frac{\sqrt{\mathbf{f}_P^H \mathbf{W}_C^{-1} \mathbf{f}_P - 1}}{\mathbf{f}_P^H \mathbf{f}_P}, \quad (4.43)$$

and

$$\mathbf{e}_C = \left(\frac{\sqrt{\|\mathbf{u}\|^2 - 1}}{\|\mathbf{u}\|^2} \mathbf{W}_C^{-1} - \alpha_C \mathbf{I} \right) \mathbf{f}_P. \quad (4.44)$$

4.2.3 Performance Analysis

In this section, we provide a brief performance analysis of the proposed perturbation schemes. The following lemmas demonstrate that the back-off factors that arise from the perturbation schemes are guaranteed to be greater than that of the adaptive power back-off solution, where the system beamforms with

$$\mathbf{f}_{\text{adp}} = \alpha_{\text{adp}} \mathbf{f}_P \quad (4.45)$$

with α_{adp} is defined as in (4.12).

Lemma 4.2.3 *Let $Q_k > 0$ for $k = 0, 1, \dots, K$ and let $\mathbf{g}_D = \alpha_D \mathbf{f}_P + \mathbf{e}_D$ be the solution to (4.17). Then, $|\alpha_D| \geq \alpha_{\text{adp}}$.*

Proof: We have that the squared Euclidean distance between \mathbf{f}_P and \mathbf{g} can be written as

$$\|\mathbf{f}_P - \mathbf{g}\|^2 = \|(1 - \alpha)\mathbf{f}_P - \mathbf{e}\|^2 = |1 - \alpha|^2 \|\mathbf{f}_P\|^2 + \|\mathbf{e}\|^2. \quad (4.46)$$

Therefore, the MinD scheme equivalently finds α and \mathbf{e} with $\mathbf{f}_P^H \mathbf{e} = 0$ which minimize the term $|1 - \alpha|^2 \|\mathbf{f}_P\|^2 + \|\mathbf{e}\|^2$ subject to the power and exposure constraints. The adaptive back-off solution, which is achieved when $\alpha = \alpha_{\text{adp}}$ and $\mathbf{e} = \mathbf{0}$, satisfies both the power and exposure constraints by definition and is a feasible solution to the optimization in (4.17). Therefore, if we have that $\mathbf{g}_D = \alpha_D \mathbf{f}_P + \mathbf{e}_D$ is the solution to (4.17), we have the following bound:

$$\begin{aligned} |1 - \alpha_D|^2 \|\mathbf{f}_P\|^2 &\leq |1 - \alpha_D|^2 \|\mathbf{f}_P\|^2 + \|\mathbf{e}_D\|^2 \\ &\leq |1 - \alpha_{\text{adp}}|^2 \|\mathbf{f}_P\|^2. \end{aligned} \quad (4.47)$$

Note that α_{adp} is real, so the inequality above yields

$$1 - |\alpha_D| \leq |1 - \alpha_D| \leq 1 - \alpha_{\text{adp}}, \quad (4.48)$$

which implies $|\alpha_D| \geq \alpha_{\text{adp}}$. ■

Lemma 4.2.4 *Let $Q_k > 0$ for $k = 0, 1, \dots, K$ and let $\mathbf{g}_C = \alpha_C \mathbf{f}_P + \mathbf{e}_C$ be the solution to (4.36). Then, $|\alpha_C| \geq \alpha_{\text{adp}}$.*

Proof: For $\mathbf{g} = \alpha \mathbf{f}_P + \mathbf{e}$ with $\mathbf{f}_P^H \mathbf{e} = 0$, we have

$$|\alpha| = \frac{|\mathbf{f}_P^H \mathbf{g}|}{\|\mathbf{f}_P\|^2}. \quad (4.49)$$

Therefore, maximizing the correlation between \mathbf{f}_P and \mathbf{g} is equivalent to maximizing α . Since \mathbf{f}_{adp} is a feasible solution to (4.36), we have that $|\alpha_C| \geq \alpha_{\text{adp}}$ as desired. ■

Note that in both perturbation schemes, the system is able to transmit with more power in the main beam compared to the adaptive back-off solution by transmitting a portion of energy in an orthogonal direction \mathbf{e} . Because of this, we refer to \mathbf{e} as an *exposure-cancelling* component, since its purpose is to decrease the exposure induced by the main beam.

In general, the beamforming gain of \mathbf{g} can be written as

$$\|\mathbf{H}\mathbf{g}\|^2 = |\alpha|^2 \|\mathbf{H}\mathbf{f}_P\|^2 + 2\text{Re} \left\{ \mathbf{f}_P^H \mathbf{H}^H \mathbf{H} \mathbf{e} \right\} + \|\mathbf{H}\mathbf{e}\|^2. \quad (4.50)$$

In many cases, however, the norm of the vector \mathbf{e} is much smaller than that of \mathbf{f}_P , and the beamforming gain can be approximated as

$$\|\mathbf{H}\mathbf{g}\|^2 \approx |\alpha|^2 \|\mathbf{H}\mathbf{f}_P\|^2. \quad (4.51)$$

Since the perturbation schemes are able to transmit with more power on the main beam, they generally perform better than the adaptive back-off method. Note that in the case $\mathbf{f}_P = \sqrt{P}\mathbf{v}_1$, where \mathbf{v}_1 is the dominant right singular vector of \mathbf{H} , we have that

$$\|\mathbf{H}\mathbf{g}\|^2 = |\alpha|^2 \|\mathbf{H}\mathbf{f}_P\|^2 + \|\mathbf{H}\mathbf{e}\|^2. \quad (4.52)$$

Therefore, both perturbation schemes are guaranteed to achieve a higher receive signal power than the adaptive back-off technique when applied to the optimal beamformer without exposure constraints.

4.3 Numerical Results

In this section, we compare the performance of the proposed perturbation schemes with the adaptive power back-off method and the optimal solution to (4.7). We first consider a MIMO system with $N_T = 2$ and $N_R = 8$. We performed Monte Carlo simulations with i.i.d. Rayleigh fading, where the entries of \mathbf{H} are distributed according to $\mathcal{CN}(0, 1)$. In the first simulation we placed a SAR constraint on the system and used a SAR matrix obtained from [35] given by

$$\mathbf{R} = \begin{bmatrix} r_1 & r_2 e^{j\varphi} \\ r_2 e^{-j\varphi} & r_1 \end{bmatrix}, \quad (4.53)$$

where $r_1 = 4.6050$, $r_2 = 2.6250$, and $\varphi = 0.78\pi$. We fixed the SAR constraint to $Q = 1.6$ W/kg and varied the transmit power P . The noise variance is fixed as $\sigma^2 = 1$ in all simulations.

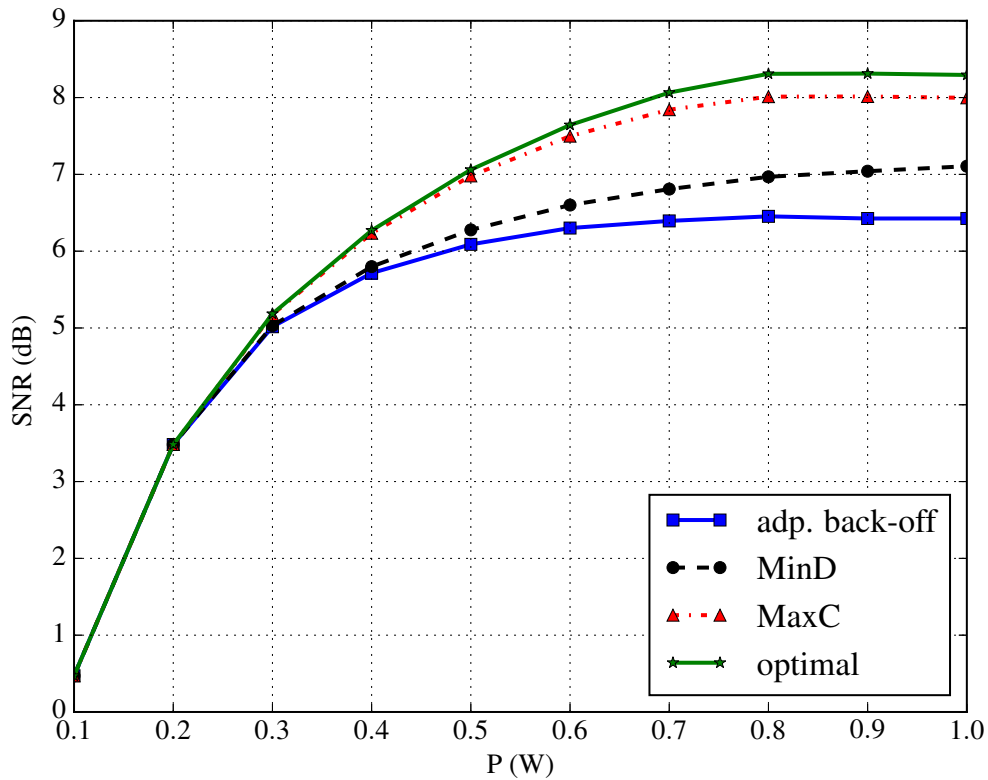


Fig. 4.1. Average receive SNR vs. transmit power P for a SAR-constrained 2x8 MIMO system. The proposed perturbation methods and the power back-off methods are applied to the optimal exposure-unaware beamformer.

In Fig. 4.1, the perturbation schemes and the traditional back-off methods are applied to the optimal exposure-unaware beamformer $\mathbf{f}_P = \sqrt{P}\mathbf{v}_1$, where \mathbf{v}_1 is the dominant eigenvector of $\mathbf{H}^H\mathbf{H}$. Both the MinD and the MaxC method achieve better SNR than the adaptive power back-off method. At $P = 1$ W, the MinD and MaxC methods achieve gains of about 0.6 dB and 1.6 dB, respectively, over the adaptive back-off method. In addition, the MaxC scheme performs nearly optimally throughout the considered range of transmit power. While the MinD approach performs notably worse than the MaxC approach, its implementation only requires the solution of a

relatively simple convex problem instead of the strong dual method required for the MaxC scheme.

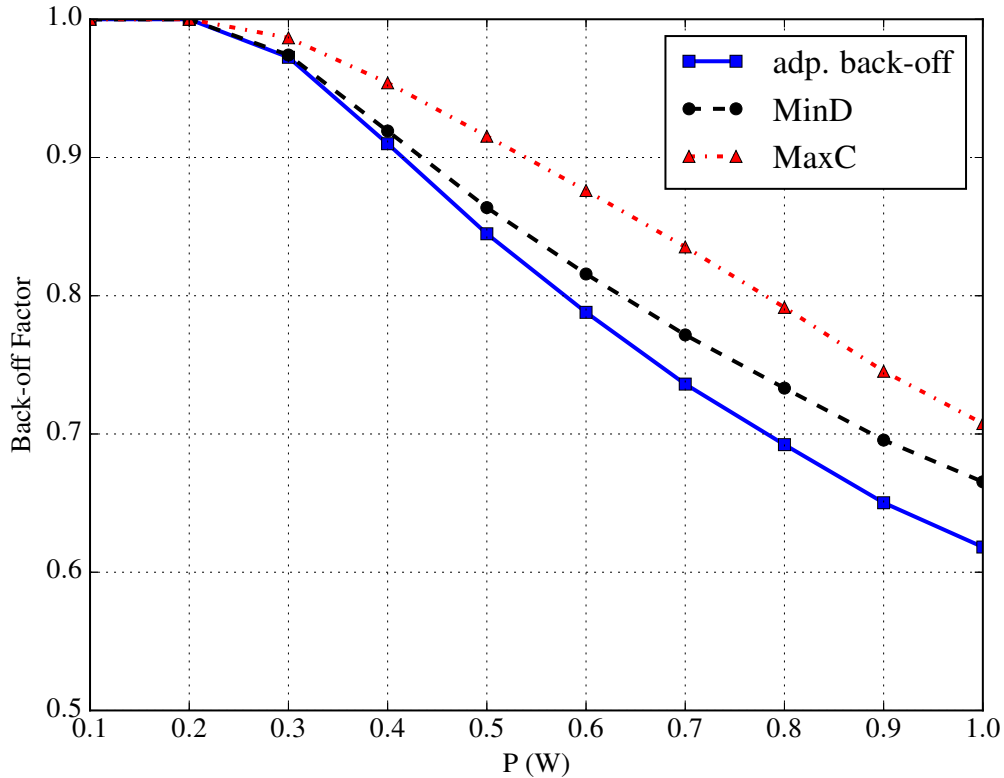


Fig. 4.2. Main beam back-off factor vs. transmit power P for a SAR-constrained 2x8 MIMO system.

Fig. 4.2 shows the main beam back-off factors for the adaptive power back-off scheme given in (4.12) and the magnitude of the back-off factor for the proposed schemes given in (4.32) and (4.43) for the case of optimal exposure-unaware beamforming. The perturbation schemes allows the system to transmit with a higher power than the adaptive power scheme, resulting in the performance gains seen in Fig. 4.1. This demonstrates the power back-off factor is the dominant factor in determining the performance of the perturbation schemes, as seen in Fig. 4.1.

In Fig. 4.4 we consider the same scenario as above, but we add a second SAR constraint to the system. The second SAR matrix is obtained from [42] and is given as

$$\mathbf{R} = \begin{bmatrix} 3.94 & -2.65 - 2.53j \\ -2.65 + 2.53j & 4.57 \end{bmatrix}. \quad (4.54)$$

We set both SAR limits as 1.6 W/kg and vary the transmit power. Note that the additional SAR constraint decreases the overall performance of the system. In this case the, the perturbation approaches achieve higher gains over the adaptive power back-off than in the single SAR constraint case. At $P = 1$ W, the MinD approach leads to a 1 dB gain over the adaptive back-off scheme, while the MaxC approach achieves a gain of 2 db over the back-off scheme.

For the next experiment, we consider a millimeter wave scenario at 28 GHz. We again perform Monte Carlo simulations with the i.i.d. realizations of the channel model in (3.2) with $L = 6$ clusters, cluster gains distributed as $\mathcal{CN}(0, 1)$, and AOAs and AODs uniformly distributed in $[-\pi/2, \pi/2)$. We assume the transmitter and receiver are equipped with half-wave dipole ULAs consisting of $N_T = 4$ and $N_R = 16$ antennas, respectively. We place an exposure constraint on the system as in Section 3.3.5, where an incident PD constraint with $Q = 4$ mW/cm² is placed on the surface of a spherical head model with radius 9 cm along an arc of measure 5° in the azimuth plane centered at boresight from the array. The distance between the head and the array is 4 mm, and the array is assumed to be perpendicular to the head normal.

Due to sparse nature of millimeter-wave channels, signaling schemes based on directional beam steering are often implemented. In this case, the beamforming vector \mathbf{f}_P is set to the transmit steering vector corresponding to the beamforming angle θ_{opt} as

$$\mathbf{f}_P = \sqrt{\frac{P}{N_T}} \mathbf{a}_T(\theta_{\text{opt}}), \quad (4.55)$$

where $\mathbf{a}_T(\theta)$ is defined as in (3.3) and θ_{opt} is given as

$$\theta_{\text{opt}} = \underset{\theta \in \mathcal{T}}{\operatorname{argmax}} \|\mathbf{H}\mathbf{a}_T(\theta)\|^2, \quad (4.56)$$

and \mathcal{T} is a codebook of beamforming angles. We assume that \mathcal{T} consists of 4 uniformly spaced angles in the range $[-\pi/2, \pi/2)$. We apply the perturbation approaches and the adaptive back-off method to the \mathbf{f}_P obtained from above.

In Fig. 4.3, we demonstrate the performance of the proposed schemes compared to the adaptive back-off scheme. The performance of the optimal scheme is shown as an upper bound for the codebook-based schemes. Note that the optimal beamformer is not restricted to the codebook. The proposed perturbation schemes demonstrate a substantial performance improvement over the adaptive back-off approach.

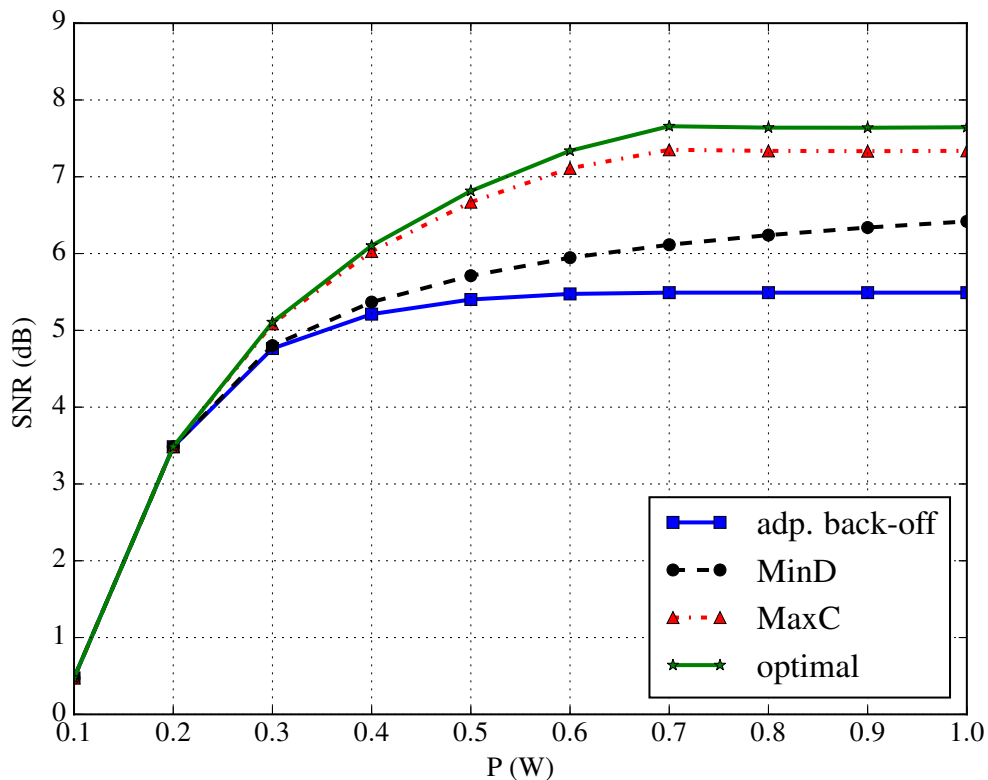


Fig. 4.3. Average receive SNR vs. transmit power P for a 2x8 MIMO system with two SAR constraints. The proposed perturbation methods and the power back-off methods are applied to the optimal exposure-unaware beamformer.

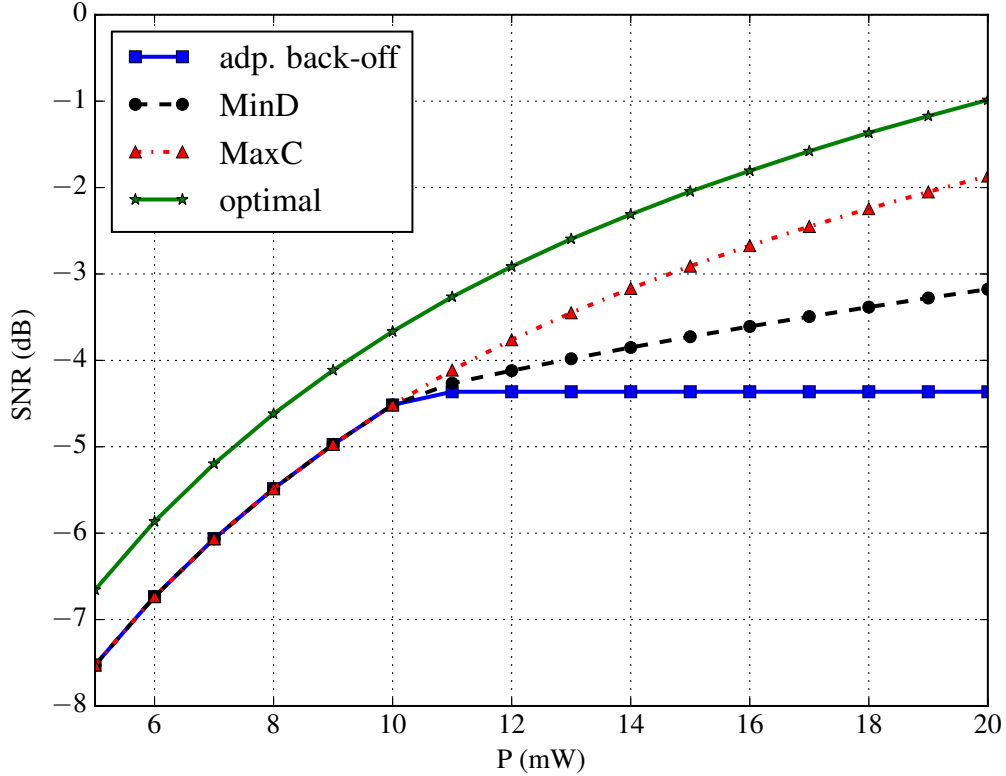


Fig. 4.4. Average receive SNR vs. transmit power P for a 4x16 MIMO millimeter wave system with an incident PD constraint. The proposed perturbation methods and the power back-off methods are applied to a DFT codebook.

In Fig. 4.5, we display the normalized array gain (with respect to the transmit power) achieved by the considered exposure-aware beamforming methods in the millimeter wave scenario. The original beam denotes the given \mathbf{f}_P from the codebook search over a sample channel realization with \mathcal{T} consisting of 16 uniformly spaced angles in the range $[-\pi/2, \pi/2)$. The optimal beamforming solution achieves the optimal tradeoff between beamforming gain and exposure compliance, and therefore demonstrates the optimal allocation of power in each direction. Note that in this case, the optimal solution significantly reduces the power of the main lobe and increases

the sidelobe levels. By contrast, the perturbation approaches show array gains which are similar to the original array gain. As expected, the MaxC array gain achieves the highest main lobe level of all of the exposure-aware schemes.

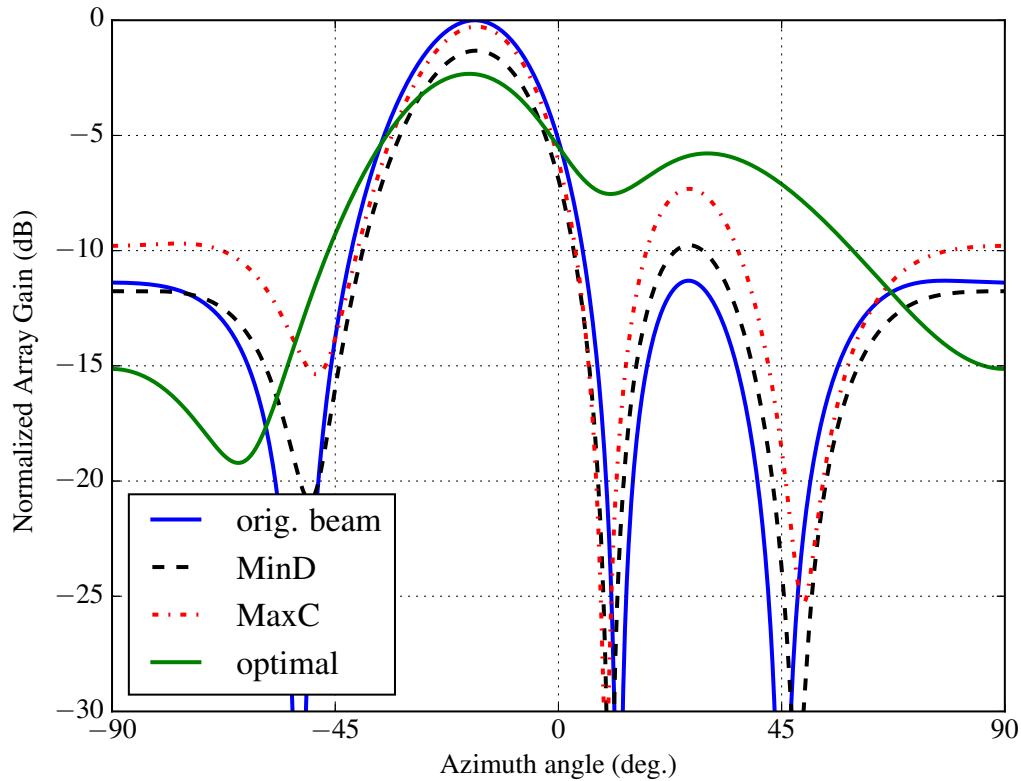


Fig. 4.5. Normalized array gain achieved by the exposure-aware beamforming methods.

4.4 Conclusion

In this chapter, we developed a low-complexity perturbation approach to reduce the exposure of a given beamforming vector in order to comply with exposure limits. The proposed method can be interpreted as reducing the power of the original beamformer and directing energy in an orthogonal direction to decrease exposure. By

employing the proposed method, the system is able to direct more power in the original beamforming direction than when employing traditional power back-off methods. Simulation results demonstrate that the proposed method is able to outperform the simpler back-off methods and only incurs a relatively small loss compared to the optimal exposure-aware beamforming approach.

5. SUMMARY

Previous research related to exposure-aware signaling has focused on sub-6 GHz systems. However, exposure management at millimeter wave is of paramount importance. The nature of millimeter wave exposure makes it potentially more dangerous to humans than sub-6 GHz exposure. In addition, millimeter wave systems need high array gains to combat the high path losses at these frequencies, which makes worst-case power back-off approaches especially harmful for millimeter wave systems.

In this dissertation, we studied the problem of exposure mitigation in the context of millimeter wave systems. The two main aspects of this problem are modeling exposure in terms of the transmit signal and designing efficient transmission schemes to maximize the performance of the system subject to exposure constraints. The former problem is important because sub-6 GHz exposure measures are not applicable at millimeter wave frequencies. The exposure-aware signal design problem for millimeter wave systems also differs from that of sub-6 GHz systems because millimeter wave systems are often constrained by hardware and power consumption limitations. Thus, there is a need to develop low-complexity algorithms which can be implemented in millimeter wave systems.

In Chapter 2, we focused on the modeling portion of the considered problem. We focused on modeling incident PD and surface SAR, as both are pertinent exposure measures in the millimeter wave band. Both of these measures are relatively simple to model in terms of array parameters, which allowed us to develop expressions to calculate pointwise exposure at any point surrounding the device. In addition, we studied the problem of how to sample regions so that the pointwise exposure models can be used to characterize average exposure. We performed various simulations with half-wave dipoles and demonstrated that the proposed models can accurately estimate millimeter wave exposure.

In Chapter 3, we presented two applications of the developed exposure models. We first developed an iterative algorithm for optimal precoding which samples the constraint space in order to identify the active constraints. We also leveraged the proposed exposure models to formulate a scheme which adjusts the transmit power not only as a function of the transmit signal but also as a function of the distance between the user and the device. Due to the increased complexity that arises from recalculating the power back-off factors each time the device moves, we proposed the use of a DFT codebook to expedite the process. Simulation results showed that both of these efficient algorithms offer significant performance benefits.

In Chapter 4, we proposed a perturbation approach as an alternative to power back-off approaches. We considered the problem of slightly perturbing a given beamformer in order to obtain a beamforming vector which attains similar beamforming gain but satisfies the exposure and power constraints. We considered two metrics for the perturbation approach which aim to reduce the performance loss associated with the perturbation. Our analytical and numerical results demonstrated that the proposed approaches outperform power back-off approaches by allowing the system to transmit with more power in the intended beamforming direction.

It is important to note that both the exposure models and the signaling strategies were developed generally and may have possible applications beyond the millimeter wave frequency band. System transmission frequencies are set to increase beyond the millimeter wave band, and the proposed exposure models may find use at higher frequencies depending on regulatory guidelines. In addition, the efficient exposure-aware signaling methods considered in this thesis offer low-complexity alternatives to exposure management. Such methods may find use in applications which require low computational complexity or low power consumption.

REFERENCES

REFERENCES

- [1] W. Roh, J.-Y. Seol, J. Park, B. Lee, J. Lee, Y. Kim, J. Cho, K. Cheun, and F. Aryanfar, "Millimeter-wave beamforming as an enabling technology for 5G cellular communications: Theoretical feasibility and prototype results," vol. 52, no. 2, pp. 106–113, Feb. 2014.
- [2] A. Ghosh, T. A. Thomas, M. C. Cudak, R. Ratasuk, P. Moorut, F. W. Vook, T. S. Rappaport, G. R. MacCartney, S. Sun, and S. Nie, "Millimeter-wave enhanced local area systems: A high-data-rate approach for future wireless networks," *IEEE Journ. Sel. Areas in Commun.*, vol. 32, no. 6, pp. 1152–1163, June 2014.
- [3] T. S. Rappaport, S. Sun, R. Mayzus, H. Zhao, Y. Azar, K. Wang, G. N. Wong, J. K. Schulz, M. Samimi, and F. Gutierrez Jr, "Millimeter wave mobile communications for 5G cellular: It will work!" *IEEE Access*, vol. 1, no. 1, pp. 335–349, May 2013.
- [4] 3GPP TR 38.901 V14.1.1 (2017-07), "Technical Specification Group Radio Access Network; Study on Channel Model for Frequencies from 0.5 to 100 GHz (Rel. 14)," July 2017.
- [5] S. Hur, T. Kim, D. J. Love, J. V. Krogmeier, T. A. Thomas, and A. Ghosh, "Millimeter wave beamforming for wireless backhaul and access in small cell networks," vol. 61, no. 10, pp. 4391–4403, Oct. 2013.
- [6] C. Dehos, J. L. González, A. De Domenico, D. Ktenas, and L. Dussopt, "Millimeter-wave access and backhauling: the solution to the exponential data traffic increase in 5G mobile communications systems?" vol. 52, no. 9, pp. 88–95, Sept. 2014.
- [7] J. Choi, V. Va, N. Gonzalez-Prelcic, R. Daniels, C. R. Bhat, and R. W. Heath, "Millimeter-wave vehicular communication to support massive automotive sensing," vol. 54, no. 12, pp. 160–167, Dec. 2016.
- [8] J. Hasch, E. Topak, R. Schnabel, T. Zwick, R. Weigel, and C. Waldschmidt, "Millimeter-wave technology for automotive radar sensors in the 77 GHz frequency band," vol. 60, no. 3, pp. 845–860, Mar. 2012.
- [9] O. El Ayach, S. Rajagopal, S. Abu-Surra, Z. Pi, and R. W. Heath, "Spatially sparse precoding in millimeter wave MIMO systems," vol. 13, no. 3, pp. 1499–1513, Mar. 2014.
- [10] J. Brady, N. Behdad, and A. M. Sayeed, "Beamspace MIMO for millimeter-wave communications: System architecture, modeling, analysis, and measurements," vol. 61, no. 7, pp. 3814–3827, July 2013.

- [11] A. Alkhateeb, O. El Ayach, G. Leus, and R. W. Heath, "Channel estimation and hybrid precoding for millimeter wave cellular systems," *IEEE Journ. Sel. Topics in Sig. Proc.*, vol. 8, no. 5, pp. 831–846, Oct. 2014.
- [12] V. Raghavan, J. Cezanne, S. Subramanian, A. Sampath, and O. Koymen, "Beamforming tradeoffs for initial UE discovery in millimeter-wave MIMO systems," *IEEE Journ. Sel. Topics in Sig. Proc.*, vol. 10, no. 3, pp. 543–559, Apr. 2016.
- [13] J. Song, J. Choi, S. G. Larew, D. J. Love, T. A. Thomas, and A. A. Ghosh, "Adaptive millimeter wave beam alignment for dual-polarized MIMO systems," vol. 14, no. 11, pp. 6283–6296, Nov. 2015.
- [14] S. Noh, M. D. Zoltowski, and D. J. Love, "Multi-resolution codebook and adaptive beamforming sequence design for millimeter wave beam alignment," vol. 16, no. 9, pp. 5689–5701, June 2017.
- [15] J. Song, J. Choi, and D. J. Love, "Common codebook millimeter wave beam design: Designing beams for both sounding and communication with uniform planar arrays," vol. 65, no. 4, pp. 1859–1872, Apr. 2017.
- [16] M. R. Castellanos, V. Raghavan, J. H. Ryu, O. H. Koymen, J. Li, D. J. Love, and B. Peleato, "Channel-reconstruction-based hybrid precoding for millimeter-wave multi-user MIMO systems," *IEEE Journ. Sel. Topics in Sig. Proc.*, vol. 12, no. 2, pp. 383–398, May 2018.
- [17] World Health Organization, International Agency for Research on Cancer, "IARC classifies radiofrequency electromagnetic fields as possibly carcinogenic to humans," May, 11. [Online]. Available: http://www.iarc.fr/en/media-centre/pr/2011/pdfs/pr208_E.pdf.
- [18] "Evaluating compliance with FCC guidelines for human exposure to radiofrequency electromagnetic fields," Federal Communications Commission, Tech. Rep. OET Bull. 65, Suppl. C, ed. 01-01, June 2001.
- [19] ICNIRP, "Guidelines for limiting exposure to time-varying electric, magnetic, and electromagnetic fields (up to 300 GHz)," *Health Phys.*, vol. 74, no. 4, pp. 494–521, Apr. 1998.
- [20] *IEEE Standard for Safety Levels with Respect to Human Exposure to Radio Frequency Electromagnetic Fields, 3 kHz to 300 GHz*. IEEE Standard C95.1-2005, 2005.
- [21] O. P. Gandhi and A. Riazi, "Absorption of millimeter waves by human beings and its biological implications," vol. 34, no. 2, pp. 228–235, Feb. 1986.
- [22] S. Gabriel, R. Lau, and C. Gabriel, "The dielectric properties of biological tissues: II. Measurements in the frequency range 10 Hz to 20 GHz," *Phys. Med. Biol.*, vol. 41, no. 11, p. 2251, Nov. 1996.
- [23] C. Alabaster, "Permittivity of human skin in millimetre wave band," *Electron. Lett.*, vol. 39, no. 21, pp. 1521–1522, Oct. 2003.
- [24] H. Hwang, J. Yim, J.-W. Cho, C. Cheon, and Y. Kwon, "110 GHz broadband measurement of permittivity on human epidermis using 1 mm coaxial probe," in *Proc. IEEE MTT-S Int. Microwave Symp. Dig.*, vol. 1, June 2003, pp. 399–402.

- [25] S. Alekseev and M. Ziskin, "Human skin permittivity determined by millimeter wave reflection measurements," *Bioelectromagnetics*, vol. 28, no. 5, pp. 331–339, July 2007.
- [26] M. Zhadobov, N. Chahat, R. Sauleau, C. Le Quement, and Y. Le Drean, "Millimeter-wave interactions with the human body: state of knowledge and recent advances," *Int. J. Microw. Wirel. Technol.*, vol. 3, no. 02, pp. 237–247, Apr. 2011.
- [27] N. Chahat, M. Zhadobov, L. Le Coq, S. I. Alekseev, and R. Sauleau, "Characterization of the interactions between a 60-GHz antenna and the human body in an off-body scenario," vol. 60, no. 12, pp. 5958–5965, Dec. 2012.
- [28] T. Wu, T. S. Rappaport, and C. M. Collins, "Safe for generations to come: Considerations of safety for millimeter waves in wireless communications," vol. 16, no. 2, pp. 65–84, Mar. 2015.
- [29] D. Colombi, B. Thors, and C. Törnevik, "Implications of EMF exposure limits on output power levels for 5G devices above 6 GHz," vol. 14, pp. 1247–1249, 2015.
- [30] K. Zhao, Z. Ying, and S. He, "EMF exposure study concerning mmwave phased array in mobile devices for 5G communication," vol. 15, pp. 1132–1135, 2016.
- [31] B. Thors, D. Colombi, Z. Ying, T. Bolin, and C. Törnevik, "Exposure to RF EMF from array antennas in 5G mobile communication equipment," *IEEE Access*, vol. 4, pp. 7469–7478, Aug. 2016.
- [32] I. Nasim and S. Kim, "Mitigation of human exposure to RF fields in downlink of millimeter-wave cellular systems," Jan. 2018.
- [33] M. Mangoud, R. Abd-Alhameed, N. McEwan, P. Excell, and E. Abdulmula, "SAR reduction for handset with two-element phased array antenna computed using hybrid MoM/FDTD technique," *Electron. Lett.*, vol. 35, no. 20, pp. 1693–1694, Sept. 1999.
- [34] K.-C. Chim, K. C. Chan, and R. D. Murch, "Investigating the impact of smart antennas on SAR," vol. 52, no. 5, pp. 1370–1374, May 2004.
- [35] B. M. Hochwald and D. J. Love, "Minimizing exposure to electromagnetic radiation in portable devices," in *UCSD Information Theory Appl. Workshop (ITA)*, San Diego, CA, USA, Feb. 2012, pp. 255–261.
- [36] B. M. Hochwald, D. J. Love, S. Yan, and J. Jin, "SAR codes," in *UCSD Information Theory Appl. Workshop (ITA)*, San Diego, CA, USA, Feb. 2013, pp. 1–9.
- [37] B. M. Hochwald, D. J. Love, S. Yan, P. Fay, and J.-M. Jin, "Incorporating specific absorption rate constraints into wireless signal design," vol. 52, no. 9, pp. 126–133, Sept. 2014.
- [38] A. Ebadi-Shahrivar, J. Ren, B. M. Hochwald, P. Fay, J.-M. Jin, and D. J. Love, "Mixed quadratic model for peak spatial-average SAR of coherent multiple antenna devices," in *Proc. IEEE Int. Symp. Antennas and Propagation USNC/URSI Nat. Radio Science Meeting*, San Diego, CA, USA, July 2017, pp. 1419–1420.

- [39] J. Li, S. Yan, Y. Liu, B. M. Hochwald, and J.-M. Jin, “A high-order model for fast estimation of electromagnetic absorption induced by multiple transmitters in portable devices,” vol. 65, no. 12, pp. 6768–6778, Dec. 2017.
- [40] A. Ebadi-Shahrivar, P. Fay, B. M. Hochwald, and D. J. Love, “Multi-antenna SAR estimation in linear time,” in *Proc. IEEE AP-S Int. Symp. Antennas and Propagation USNC/URSI Nat. Radio Science Meeting*, Boston, MA, USA, July 2018, pp. 583–584.
- [41] A. Ebadi-Shahrivar, P. Fay, D. J. Love, and B. M. Hochwald, “Determining electromagnetic exposure compliance of multi-antenna devices in linear time,” vol. 67, no. 12, pp. 7585–7596, Dec. 2019.
- [42] D. Ying, D. J. Love, and B. M. Hochwald, “Closed-loop precoding and capacity analysis for multiple antenna wireless systems with user radiation exposure constraints,” vol. 14, no. 10, pp. 5859–5870, Oct. 2015.
- [43] —, “Sum-rate analysis for multi-user MIMO systems with user exposure constraints,” vol. 16, no. 11, pp. 7376–7388, Sept. 2017.
- [44] —, “Beamforming optimization with a constraint on user electromagnetic radiation exposure,” in *Proc. Conf. Information Sciences and Systems (CISS)*, Baltimore, MD, USA, Mar. 2013.
- [45] —, “Transmit covariance optimization with a constraint on user electromagnetic radiation exposure,” in *Proc. IEEE Global Communications Conf. (GLOBECOM)*, Atlanta, GA, USA, Dec. 2013, pp. 4104–4109.
- [46] M. R. Castellanos, D. J. Love, and B. M. Hochwald, “Hybrid precoding for millimeter wave systems with a constraint on user electromagnetic radiation exposure,” in *Proc. IEEE Asilomar Conf. Signals, Systems, and Computers*, Pacific Grove, CA, USA, Nov. 2016, pp. 296–300.
- [47] M. Harper, C. M. Forrester, and C. Lorenz, “Ultrasonic proximity sensing for SAR mitigation,” US Patent App. 16 390 893, Nov. 7, 2019.
- [48] J. C. Lin, “Specific absorption rates induced in head tissues by microwave radiation from cell phones,” vol. 2, no. 1, pp. 22–25, Oct. 2001.
- [49] D. H. Johnson and D. E. Dudgeon, *Array Signal Processing: Concepts and Techniques*. Eaglewood Cliffs, NJ, USA: PTR Prentice Hall, 1993.
- [50] C. A. Balanis, *Antenna Theory: Analysis and Design*, 4th ed. Hoboken, NJ, USA: John Wiley & Sons, Inc., 2016.
- [51] *IEEE Recommended Practice for Measurements and Computations of Radio Frequency Electromagnetic Fields With Respect to Human Exposure to Such Fields, 100 kHz-300 GHz*. IEEE Standard C95.3-2002, 2002.
- [52] I. Gupta and A. Ksienski, “Effect of mutual coupling on the performance of adaptive arrays,” vol. 31, no. 5, pp. 785–791, Sept. 1983.
- [53] B. Friedlander and A. J. Weiss, “Direction finding in the presence of mutual coupling,” vol. 39, no. 3, pp. 273–284, Mar. 1991.

- [54] T. Su and H. Ling, “On modeling mutual coupling in antenna arrays using the coupling matrix,” *Microw. Opt. Tech. Lett.*, vol. 28, no. 4, pp. 231–237, Feb. 2001.
- [55] M. Born and E. Wolf, *Principles of Optics*, 7th ed. Cambridge, UK: Cambridge Univ. Press, 1999.
- [56] A. A. Saleh and R. Valenzuela, “A statistical model for indoor multipath propagation,” vol. 5, no. 2, pp. 128–137, Feb. 1987.
- [57] R. Hettich and K. O. Kortanek, “Semi-infinite programming: theory, methods, and applications,” *SIAM review*, vol. 35, no. 3, pp. 380–429, Sept. 1993.
- [58] R. Reemtsen, “Discretization methods for the solution of semi-infinite programming problems,” *Journal of Optimization Theory and Applications*, vol. 71, no. 1, pp. 85–103, Oct. 1991.
- [59] “Man-systems integration standards,” *NASA-STD-3000, Revision B*, 1995.
- [60] R. D. Yates, “A framework for uplink power control in cellular radio systems,” vol. 13, no. 7, pp. 1341–1347, 1995.
- [61] H.-S. Jo, C. Mun, J. Moon, and J.-G. Yook, “Interference mitigation using uplink power control for two-tier femtocell networks,” vol. 8, no. 10, pp. 4906–4910, 2009.
- [62] 3GPP TS 36.211, “Evolved universal terrestrial radio access (E-UTRA); Physical channels and modulation,” (Release 15).
- [63] M. R. Castellanos, Y. Liu, D. J. Love, B. Peleato, J.-M. Jin, and B. M. Hochwald, “Signal-level models of pointwise electromagnetic exposure for millimeter wave communication,” accepted in *IEEE Trans. Antennas Propag.*, June 2019.
- [64] J. C. Lin, “FCC announces its existing RF exposure limits apply to 5G,” vol. 21, no. 4, pp. 15–17, 2020.
- [65] D. J. Love, R. W. Heath, and T. Strohmer, “Grassmannian beamforming for multiple-input multiple-output wireless systems,” *IEEE transactions on information theory*, vol. 49, no. 10, pp. 2735–2747, 2003.
- [66] V. Raghavan, R. W. Heath, and A. M. Sayeed, “Systematic codebook designs for quantized beamforming in correlated MIMO channels,” vol. 25, no. 7, pp. 1298–1310, 2007.

APPENDIX

A. APPENDIX

A.1 Proof of Lemma 2.4.1

Let $r = \|\mathbf{p}\|$ and $\tilde{r} = \|\tilde{\mathbf{p}}\|$, and denote $\mathbf{a}(\mathbf{p})$ and $\mathbf{a}(\tilde{\mathbf{p}})$ as \mathbf{a} and $\tilde{\mathbf{a}}$, respectively. The n -th element of \mathbf{a} is expressed as

$$\mathbf{a}_n = g^{1/2}(\mathbf{p}) \frac{r}{r_n} \exp(-j\varphi_n), \quad (\text{A.1})$$

where φ_n is given as in (2.5), and similarly for $\tilde{\mathbf{a}}_n$. Since the points \mathbf{p} and $\tilde{\mathbf{p}}$ are nonzero, the desired bound can be expressed as

$$A = \frac{\left| |\tilde{r}\mathbf{a}^H\mathbf{x}| - |r\tilde{\mathbf{a}}^H\mathbf{x}| \right|}{r\tilde{r}} \frac{\left| |\tilde{r}\mathbf{a}^H\mathbf{x}| + |r\tilde{\mathbf{a}}^H\mathbf{x}| \right|}{r\tilde{r}} < \varepsilon. \quad (\text{A.2})$$

We first derive an upper bound on A in terms of the inter-point distance $\|\mathbf{p} - \tilde{\mathbf{p}}\|$. An application of the reverse triangle inequality and the Cauchy-Schwarz inequality gives an upper bound on A as

$$A \leq BC\|\mathbf{x}\|^2 \triangleq \left[\frac{\|\tilde{r}\mathbf{a} - r\tilde{\mathbf{a}}\| \|\tilde{r}\mathbf{a}\| + \|r\tilde{\mathbf{a}}\|}{r\tilde{r}} \right] \|\mathbf{x}\|^2. \quad (\text{A.3})$$

For clarity, we bound B and C separately.

Through repeated applications of the triangle inequality and the Cauchy-Schwarz inequality, it can be shown that the term B can be bounded as

$$\begin{aligned}
B &\leq G_{\max}^{1/2} \sum_{n=0}^{N-1} \left| \frac{\exp(j\varphi_n)}{r_n} - \frac{\exp(j\tilde{\varphi}_n)}{\tilde{r}_n} \right| \\
&\leq G_{\max}^{1/2} \sum_{n=0}^{N-1} \frac{1}{r_n} |\exp(j\varphi_n) - \exp(j\tilde{\varphi}_n)| + \left| \frac{1}{r_n} - \frac{1}{\tilde{r}_n} \right| \\
&= G_{\max}^{1/2} \sum_{n=0}^{N-1} \frac{2}{r_n} \left| \sin\left(\frac{\varphi_n - \tilde{\varphi}_n}{2}\right) \right| + \left| \frac{\tilde{r}_n - r_n}{r_n \tilde{r}_n} \right| \\
&\stackrel{(a)}{\leq} G_{\max}^{1/2} \sum_{n=0}^{N-1} \left(\frac{2\pi}{\lambda r_n} |r_n - r + \tilde{r} - \tilde{r}_n| + \left| \frac{\tilde{r}_n - r_n}{r_n \tilde{r}_n} \right| \right) \\
&\leq G_{\max}^{1/2} \sum_{n=0}^{N-1} \left(\frac{2\pi}{\lambda r_n} (|r_n - \tilde{r}_n| + |r - \tilde{r}|) + \left| \frac{\tilde{r}_n - r_n}{r_n \tilde{r}_n} \right| \right) \\
&\stackrel{(b)}{\leq} G_{\max}^{1/2} \left(\frac{4\pi N}{r_{\min} \lambda} \|\mathbf{p} - \tilde{\mathbf{p}}\| + \frac{N}{r_{\min}^2} \|\mathbf{p} - \tilde{\mathbf{p}}\| \right), \tag{A.4}
\end{aligned}$$

The bound $\sin(y) < y$ for $y > 0$ is used in (a), and (b) results from the definition of r_{\min} . Similarly, the term C can be bounded as

$$\begin{aligned}
C &\leq G_{\max}^{1/2} \sum_{n=0}^{N-1} \left| \frac{\exp(j\varphi_n)}{r_n} \right| + \left| \frac{\exp(j\tilde{\varphi}_n)}{\tilde{r}_n} \right| \\
&\leq \frac{2NG_{\max}^{1/2}}{r_{\min}}. \tag{A.5}
\end{aligned}$$

Combining the bounds for B and C , we have that

$$A < \frac{2N^2 G_{\max} \|\mathbf{x}\|^2}{r_{\min}^2} \left(\frac{4\pi}{\lambda} + \frac{1}{r_{\min}} \right) \|\mathbf{p} - \tilde{\mathbf{p}}\|. \tag{A.6}$$

Therefore, $A < \varepsilon$ if

$$\|\mathbf{p} - \tilde{\mathbf{p}}\| < \frac{\varepsilon r_{\min}^2}{2N^2 G_{\max} \|\mathbf{x}\|^2} \left(\frac{4\pi}{\lambda} + \frac{1}{r_{\min}} \right)^{-1}. \tag{A.7}$$

Let $r = \|\mathbf{p}\|$ and $\tilde{r} = \|\tilde{\mathbf{p}}\|$, and denote $\mathbf{a}(\mathbf{p})$ and $\mathbf{a}(\tilde{\mathbf{p}})$ as \mathbf{a} and $\tilde{\mathbf{a}}$, respectively. The n -th element of \mathbf{a} is expressed as

$$\mathbf{a}_n = g_n^{1/2}(\mathbf{p}_n) \frac{r}{r_n} \exp(-j\varphi_n), \tag{A.8}$$

where φ_n is given as in (2.5), and similarly for $\tilde{\mathbf{a}}_n$. Since the points \mathbf{p} and $\tilde{\mathbf{p}}$ are nonzero, the desired bound can be expressed as

$$A = \frac{\left| |\tilde{r}\mathbf{a}^H\mathbf{x}| - |r\tilde{\mathbf{a}}^H\mathbf{x}| \right|}{r\tilde{r}} \frac{|\tilde{r}\mathbf{a}^H\mathbf{x}| + |r\tilde{\mathbf{a}}^H\mathbf{x}|}{r\tilde{r}} < \varepsilon. \quad (\text{A.9})$$

We first derive an upper bound on A in terms of the inter-point distance $\|\mathbf{p} - \tilde{\mathbf{p}}\|$. An application of the reverse triangle inequality and the Cauchy-Schwarz inequality gives an upper bound on A as

$$A \leq BC\|\mathbf{x}\|^2 \triangleq \left[\frac{\|\tilde{r}\mathbf{a} - r\tilde{\mathbf{a}}\|}{r\tilde{r}} \right] \left[\frac{\|\tilde{r}\mathbf{a}\| + \|r\tilde{\mathbf{a}}\|}{r\tilde{r}} \right] \|\mathbf{x}\|^2. \quad (\text{A.10})$$

For clarity, we bound B and C separately.

Through repeated applications of the triangle inequality and the Cauchy-Schwarz inequality, it can be shown that the term B can be bounded as

$$\begin{aligned} B &\leq G_{\max}^{1/2} \sum_{n=0}^{N-1} \left| \frac{\exp(j\varphi_n)}{r_n} - \frac{\exp(j\tilde{\varphi}_n)}{\tilde{r}_n} \right| \\ &\leq G_{\max}^{1/2} \sum_{n=0}^{N-1} \left(\frac{1}{r_n} |\exp(j\varphi_n) - \exp(j\tilde{\varphi}_n)| + \left| \frac{1}{r_n} - \frac{1}{\tilde{r}_n} \right| \right) \\ &= G_{\max}^{1/2} \sum_{n=0}^{N-1} \left(\frac{2}{r_n} \left| \sin \left(\frac{\varphi_n - \tilde{\varphi}_n}{2} \right) \right| + \left| \frac{\tilde{r}_n - r_n}{r_n \tilde{r}_n} \right| \right) \\ &\stackrel{(a)}{\leq} G_{\max}^{1/2} \sum_{n=0}^{N-1} \left(\frac{2\pi}{\lambda r_n} |r_n - r + \tilde{r} - \tilde{r}_n| + \left| \frac{\tilde{r}_n - r_n}{r_n \tilde{r}_n} \right| \right) \\ &\leq G_{\max}^{1/2} \sum_{n=0}^{N-1} \left(\frac{2\pi}{\lambda r_n} (|r_n - \tilde{r}_n| + |r - \tilde{r}|) + \left| \frac{\tilde{r}_n - r_n}{r_n \tilde{r}_n} \right| \right) \\ &\stackrel{(b)}{\leq} G_{\max}^{1/2} \left(\frac{4\pi N}{r_{\min} \lambda} \|\mathbf{p} - \tilde{\mathbf{p}}\| + \frac{N}{r_{\min}^2} \|\mathbf{p} - \tilde{\mathbf{p}}\| \right), \end{aligned} \quad (\text{A.11})$$

The bound $\sin(y) < y$ for $y > 0$ is used in (a), and (b) results from the definition of r_{\min} . Similarly, the term C can be bounded as

$$\begin{aligned} C &\leq G_{\max}^{1/2} \sum_{n=0}^{N-1} \left(\left| \frac{\exp(j\varphi_n)}{r_n} \right| + \left| \frac{\exp(j\tilde{\varphi}_n)}{\tilde{r}_n} \right| \right) \\ &\leq \frac{2NG_{\max}^{1/2}}{r_{\min}}. \end{aligned} \quad (\text{A.12})$$

Combining the bounds for B and C , we have that

$$A < \frac{2N^2 G_{\max} \|\mathbf{x}\|^2}{r_{\min}^2} \left(\frac{4\pi}{\lambda} + \frac{1}{r_{\min}} \right) \|\mathbf{p} - \tilde{\mathbf{p}}\|. \quad (\text{A.13})$$

Therefore, $A < \varepsilon$ if $\|\mathbf{p} - \tilde{\mathbf{p}}\| < \Delta / \|\mathbf{x}\|^2$.

VITA

VITA

M. Rodrigo Castellanos received the B.S. degree (with highest distinction) in electrical engineering in 2015 from Purdue University, West Lafayette, IN, USA where he is currently working toward the Ph.D. degree. During the summers of 2017 and 2019, he was a research intern at Qualcomm Flarion Technologies, Bridgewater, NJ, USA and at Nokia Networks, Naperville, IL, USA, respectively. His current research interests are in massive MIMO, millimeter wave communication, and multi-antenna systems with user exposure constraints. He was recognized as an Exemplary Reviewer of the IEEE WIRELESS COMMUNICATIONS LETTERS in 2018.